Mesoscale Ocean Eddy-Wind Interaction

A thesis submitted to the School of Environmental Sciences at the University of East Anglia in partial fulfilment of the requirements for the degree of Doctor of Philosophy

Thomas Matthew Wilder

100212402

September 2022

Abstract

A surface wind stress that includes the ocean surface current (known as relative wind stress) can result in a damping of eddy energy. A weakened eddy field has significant implications for the regional and global ocean circulation. Eddy energy budget-based parameterisations currently employ an arbitrary dissipation rate, leaving some uncertainty in future climate projections. Furthermore, the role of relative wind stress on eddy dynamics is not yet fully understood.

Using shallow water theory and analytical equations, a method is developed to predict the decay of barotropic and baroclinic eddy energy due to relative wind stress. The prediction is then compared against high-resolution numerical simulations. Predicting barotropic eddy energy works well when the Rossby number is less than 0.1. Predicting baroclinic eddy energy compares well with its respective numerical simulation, although performs poorly when the numerical eddy destabilises. Eddy energy dissipation rates are then inferred via the analytical framework.

The response of an anticyclonic baroclinic eddy to relative wind stress is subsequently examined in a dedicated case study. The damping of mean kinetic energy by relative wind stress is counteracted by an additional conversion of mean potential to mean kinetic energy via linear Ekman pumping. A scaling argument between additional conversion and damping confirms these results. Linear Ekman pumping also transfers horizontal density gradients into vertical, modifying surface potential vorticity gradients. As a result, the eddy destabilises and generates instabilities earlier.

Sensitivity experiments reveal that a cyclonic eddy responds similarly to the anticyclonic case, though an earlier destabilisation takes place. An anticyclonic eddy with a more stable stratification exhibits reduced additional conversion of mean potential to mean kinetic energy due to relative wind stress.

Access Condition and Agreement

Each deposit in UEA Digital Repository is protected by copyright and other intellectual property rights, and duplication or sale of all or part of any of the Data Collections is not permitted, except that material may be duplicated by you for your research use or for educational purposes in electronic or print form. You must obtain permission from the copyright holder, usually the author, for any other use. Exceptions only apply where a deposit may be explicitly provided under a stated licence, such as a Creative Commons licence or Open Government licence.

Electronic or print copies may not be offered, whether for sale or otherwise to anyone, unless explicitly stated under a Creative Commons or Open Government license. Unauthorised reproduction, editing or reformatting for resale purposes is explicitly prohibited (except where approved by the copyright holder themselves) and UEA reserves the right to take immediate ‘take down’ action on behalf of the copyright and/or rights holder if this Access condition of the UEA Digital Repository is breached. Any material in this database has been supplied on the understanding that it is copyright material and that no quotation from the material may be published without proper acknowledgement.

Contents

List of Figures

List of Tables

Acknowledgements

I would like to dedicate this thesis to my father, William Dean Wilder. I think he would be proud.

I am extremely grateful to all who have helped me through this PhD journey, an experience I will absolutely never forget. I would like to thank first and foremost my supervisory team, Xiaoming, Dave, and Manoj, who have given me their patience, support, and enthusiasm. Xiaoming, you have guided me to think in terms of Big Picture science. Dave, you have taught me that general circulation models are not scary beasts, but fun toys. Manoj, your words of encouragement and advice have been like gold. My appreciation for mathematics in the natural world has only grown deeper with each of your tuition. I would not be here today if it were not for you three. I am also thankful to my office mate Zhibin, who helped me get to grips with MITgcm.

Special thanks also go to my friends who have given me laughter and a shoulder for support over the past four years. My family's enthusiasm for my PhD has always been enjoyable, and I thank my grandad especially for putting time and energy into extra curricular reading. A big thank you goes to Katy for helping me believe in myself and always seeing the positives, even when I might not see them.

I'd like to acknowledge IT Linux and the HPC department for assisting me when things stopped working or things were not too obvious. Heading out on a research cruise was one of the most memorable experiences to date, and so I would like to extend thanks to Karen for encouraging me to apply during my probationary review meeting. And obviously, none of this research would have been made possible without funding from NERC, who do a stellar job in supporting science in the UK.

1

Introduction

1.1 Introducing mesoscale eddies

1.1.1 Definition

Ocean eddies are coherent vortices that exhibit highly variable spatial and temporal scales that differ from the background mean flow (Chelton et al., 2007). Mesoscale eddies have horizontal length scales - $[O(10 - 100 \text{ km})]$ - on the order of the *first baroclinic Rossby radius of deformation*, which describes the length scale where rotational effects become important. Eddies can primarily be categorised as either anticyclonic or cyclonic, displaying positive or negative sea surface height anomalies and depressed or raised thermocline displacements, respectively (see Fig. 1.1.1).

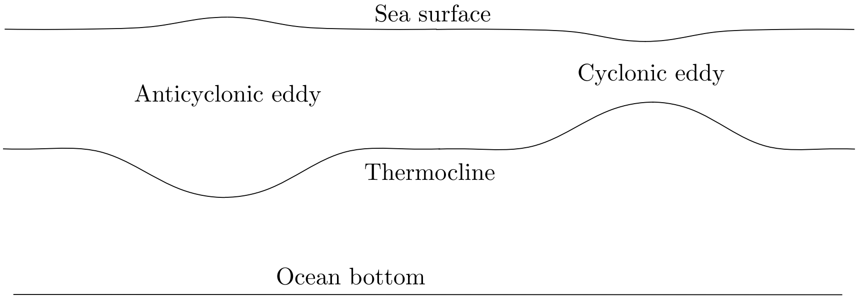

Figure 1.1.1: Schematic depicting anticyclonic (left) and cyclonic (right) eddy in a simple two-layer ocean. Anticyclonic eddy has a raised sea surface and a depressed thermocline. The opposite is the case for the cyclonic eddy.

The abundance of mesoscale eddies in the world's ocean is revealed through sea surface height in satellite altimetry data (Fig. 1.1.2), where the most populated regions are the western boundary currents and the Southern Ocean (Chelton et al., 2011), though they do also occur mid-ocean (Arbic and Flierl, 2004). These boundary currents typically meander and loop back on themselves creating a coherent eddy-like structure, paving a way for eddies to pinch off from the main jet. Depending on which side the jet meanders, eddies can contain either cold nutrient rich waters or warm nutrient deficient waters (see Fig. 3 in McGillicuddy (2016)). Eddies can also trap oceanic properties within their core, aiding the mixing and redistribution of tracers in the ocean (Chelton et al., 2011). Satellite altimetry data has shown that eddies display remarkable horizontal structures, encompassing much of the ocean surface (Chelton et al., 2011; Chen et al., 2019). Their vertical structure has also been diagnosed using in-situ Argo float data, showing deep reaching structures with large ocean tracer anomalies (Yang et al., 2013).

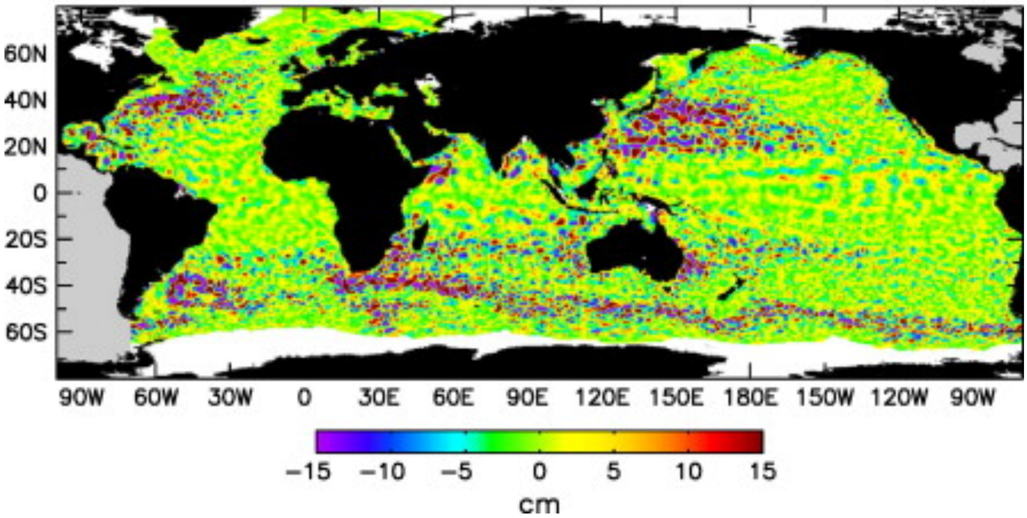

Figure 1.1.2: Sea surface anomaly height map showing prevalence of eddies across the world's ocean. Source: Chelton et al. (2011).

Mesoscale eddies can be further defined through their vertical structure as being either barotropic or baroclinic. A barotropic eddy will exhibit parallel surfaces of density and pressure throughout the water column. Barotropic eddies are generated by horizontal or vertical shear instabilities in the mean flow (Kloosterziel and Van Heijst, 1991). A baroclinic eddy will display sloping density surfaces that cross pressure surfaces, producing gradients in density.

Baroclinic eddies are produced via large-scale atmospheric processes, such as wind, that tilt density surfaces, leading to a release of potential energy (Gill et al., 1974).

1.1.2 Wider importance

The ubiquitousness of mesoscale eddies in the world's ocean coupled with their unique structure and dynamics, make them important features of the climate system. Since eddies typically populate regions with fast flowing currents, their impact on these particular regions has been examined extensively. In a model of the Northwest Atlantic, Zhai and Greatbatch (2006) examined a rich eddy field and found eddies contributed to a net ocean surface heat loss of 100 W m^{-2}. Consistent with results from Zhai and Greatbatch, Griffies et al. (2015) showed that eddies act as a regulator for ocean heat uptake, whereby they transport heat upwards in response to the large-scale wind driven downwelling. Past the separation point of the Gulf Stream at the US east coast, eddy momentum fluxes have been shown to explain the increased oceanic transport there (Greatbatch et al., 2010). By neglecting eddy activity in the Kuroshio Extension, Ma et al. (2015) revealed this to enhance heavy rainfall events over the US west coast, highlighting the downstream effects of mesoscale eddies. Eddies also contribute to the global Meridional Overturning Circulation through their excitement of equatorward propagating boundary waves upon their entering western boundary regions (Zhai et al., 2004; Zhai and Yang, 2022). Zhai and Yang found eddy-induced transport anomalies that ranged between 1 to 5 Sv over timescales of 10 to 100 days, meaning eddies could play an important role in forecasting accurate seasonal and climate variability.

The Southern Ocean connects all ocean basins through an overturning circulation; is one of the largest sinks of anthropogenic carbon; transports waters to and from the ice shelves; and is home to the largest ocean current, the Antarctic Circumpolar Current (ACC) (Rintoul, 2018). Therefore the Southern

Ocean is influential on a wide swathe of climate processes that has effects on global scales. The Ekman transport associated with strong eastward zonal winds that drive the ACC tilt the meridional density gradient, or isopycnals, which enables the generation of mesoscale eddies via baroclinic instability (Holland and Lin, 1975). Eddies in the Southern Ocean are also produced via the Agulhas and Malvinas (Falkland) boundary current regions. The presence of mesoscale eddies in the Southern Ocean mean they can impart wide reaching impacts regionally and globally. Increasing wind speeds over the ACC can generate additional horizontal northward Ekman transport with a steepening of isopycnals. With this in mind, resolved eddies in general circulation models have been found to constrain the zonal ACC transport through the flattening of isopycnals, which is termed *eddy saturation* (Straub, 1993; Hallberg and Gnanadesikan, 2001; Munday et al., 2013). Eddies can also limit the Residual Meridional Overturning Circulation by inducing an opposing southward eddy transport to the northward Ekman transport, which is termed *eddy compensation* (Hallberg and Gnanadesikan, 2006; Meredith et al., 2012). However, Hewitt et al. (2016) noted an increase in ACC volume transport in higher resolution models, suggesting eddy fluxes may play a role in this increase. Eddies have also been shown to transport heat southwards from the Agulhas region (Meijers et al., 2007), as well as Circumpolar Deep Water across the Antarctic shelf break (Stewart and Thompson, 2015). Additionally, Munday et al. (2014) show a reduction in partial pressure of atmospheric carbon dioxide (pCO_2) sensitivity to changes in wind stress when including mesoscale eddies in the Southern Ocean. Linked with eddy saturation and eddy compensation, Munday et al. conclude that climate change induced wind stress changes over this region may have a lesser impact on pCO_2 than lower resolution models predict. Moreover, it has recently been shown that eddy rich regions in the ACC can lead to significant exchanges of ocean properties from the surface to the ocean interior (Dove et al., 2022).

The impact of eddies on the air-sea exchange of tracers and the above atmosphere has been examined in detail. Variability of CO_2 exchange by eddies is distinct between the seasons, whereby Song et al. (2016) revealed the warming (cooling) of anticyclones in summer (winter) enables more (less) uptake (outgassing). Studying a single warm core eddy in the South Atlantic, Pezzi et al. (2021) also showed that this type of eddy was able to act as a local source of CO_2 in a region otherwise known to be a net sink. In addition, Pezzi et al. were able to show increases in this source of CO_2 were linked with increases in sea surface temperature and wind speed. Villas-Bôas et al. (2015) looked at the exchange of heat at the ocean surface in the South Atlantic Ocean, finding eddies were able to account for 20% of the turbulent surface heat flux variance. Through the interaction of mesoscale eddies and the overlying atmosphere, the spatial variability of eddies was found to modify near-surface wind, cloud cover, and precipitation (Frenger et al., 2013).

In general, eddy dynamics can impose a unique influence on the biogeochemical cycle of the ocean. Cyclonic eddies display domed thermoclines (see Fig. 1.1.1) and as a result upwell nutrient-rich waters into the surface layers. Falkowski et al. (1991) showed this cyclonic upwelling enhanced primary production in the North Pacific by around 20%. McGillicuddy et al. (1998) later suggested the dynamics of mesoscale eddies are needed to balance the nutrient budget in the Sargasso Sea. Phytoplankton blooms also take place within the cores of mesoscale eddies, and can be sustained through eddy-wind interaction (McGillicuddy et al., 2007). Vertical motions generated by eddy-wind interaction are argued by Gaube et al. (2013) to also help sustain positive phytoplankton anomalies. Chenillat et al. (2015) further distinguished the role of eddies in the biogeochemical cycle within the California Current System, an eddy-rich upwelling boundary current system. Chennilat et al showed that eddies redistributed and reinvigorated regions of high primary productivity through their upwelling and trapping of biological tracers. Arostegui et al. (2022) colocated mesoscale eddy locations with pelagic predator catch, and found anticyclonic eddies displayed catch counts of around 80% higher than cyclonic eddies. They attributed this result to the extended depth of the anticyclonic warm cores, enabling thermally limited predators to spend more time at depth, subsequently increasing the pelagic population available to catch. In addition, many other studies have linked mesoscale eddies with the wider variability and behaviour of marine ecosystems (Alemany et al., 2010; Bailleul et al., 2010). These studies highlight the importance of vertical motions within mesoscale eddies on the ocean's bigoeochemical cycle.

These studies reveal mesoscale eddies have regional and global impacts within the climate system. Therefore, understanding eddy dynamics is of utmost importance for accurate ocean tracer and energy budgets, as well as inferring their climate impacts and making appropriate climate projections. In the next section we outline some relevant past literature on the dynamics of ocean eddies that aims to provide some motivation and context for this thesis.

1.2 A review of relevant past literature

1.2.1 Eddy energy

Eddy energy is important to diagnose and accurately represent as eddies make important contributions to the dynamics of the large-scale ocean circulation (Mcwilliams, 2008). Through detailed remote sensing data of sea surface heights, the mesoscale surface variability is now well captured (see Fig. 1.1.2). Sea surface height data has been shown to be extremely useful in determining eddy length scales (Stammer, 1997) and mapping the oceanic geostrophic kinetic energy (Wunsch and Stammer, 1998). The most energetic regions are major current systems like the Gulf Stream and Antarctic Circumpolar Current (see Fig. 1.2.1) as a result of the large-scale atmospheric winds forcing a baroclinically unstable regime (Holland, 1978). These energetic regions are clearly correlated with the positive and negative sea surface height data. Estimates of mesoscale eddy kinetic energy have since found eddies account for up to 80% of the total ocean kinetic energy (Ferrari and Wunsch, 2009).

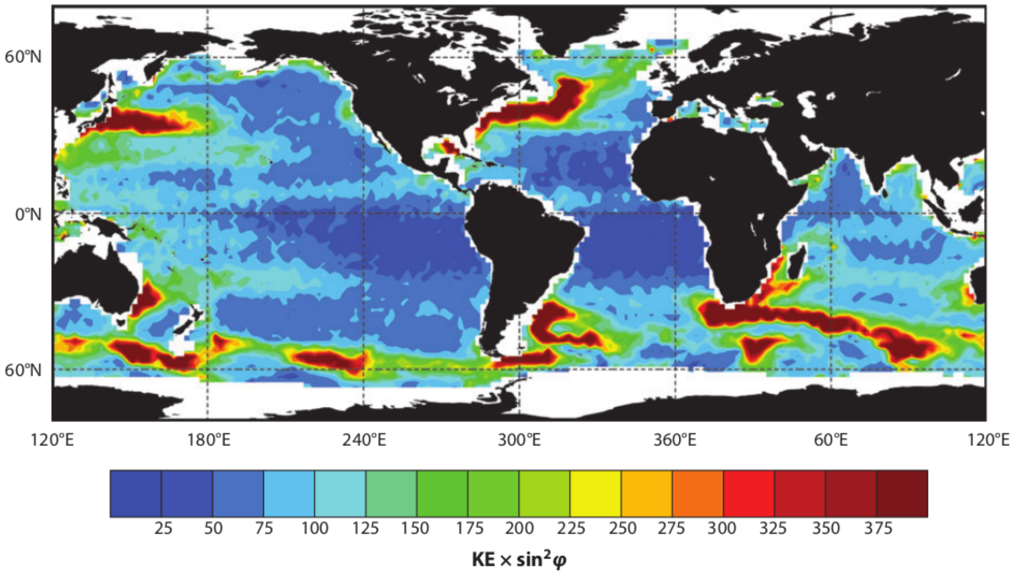

Figure 1.2.1: Oceanic geostrophic kinetic energy (cm^2 s^{-2}) over the world's ocean. To avoid the equatorial singularity, kinetic energy is multiplied by $\sin^2(\phi)$, where ϕ is latitude. Source: Ferrari and Wunsch (2009), orignally produced by Wunsch and Stammer (1998).

Studies have attempted to decompose the vertical structure of kinetic energy in mesoscale eddies. Wunsch (1997) detailed eddy kinetic energy to exist primarily in the barotropic and first baroclinic modes. These modes describe the vertical structure of the eddy, where barotropic is depth-independent, and baroclinic is depth-dependent. Examples of these modes can be seen in Fig. 1 of Wunsch (1997), and are also derived in chapter 3 for a simple two-layer model. Wunsch found that the majority of kinetic energy in the ocean was captured in the first baroclinic mode (60-70%), though some regions - e.g. south of the Gulf Stream - exhibited strong barotropic mode signals, containing 90% of kinetic energy. However, Wunsch argued that little kinetic energy contained in the barotropic mode can actually be inferred from sea surface height data. This is primarily because the sea surface height signal is dominated by the first baroclinic mode due to density anomalies.

Mesoscale eddy energy is therefore captured in the barotropic and first baroclinic modes as a result of eddy generation processes e.g. winds. Through the eddy stirring of density anomalies, a *forward cascade* directs potential energy in the horizontal from larger scales to smaller scales, until it undergoes a conversion into kinetic energy via baroclinic instability (see Fig. 1.2.2). The majority of this energy conversion takes place near length scales close to the first baroclinic Rossby radius of deformation, a length scale typical of mesoscale eddies (Scott and Arbic, 2007). Some of this conversion takes place at much smaller scales (submesoscale $\sim \Delta 1$ km), but can then be transferred back to mesoscale eddies via the *inverse cascade*. The inverse cascade is the upscale transfer of kinetic energy from smaller to larger scales through nonlinear interactions. Baroclinic kinetic energy is then either dissipated or transferred upscale where it can undergo *barotropisation*, a transfer from the first baroclinic mode to the barotropic mode (Smith and Vallis, 2001). However, in the presence of realistic ocean stratification, Smith and Vallis found barotropisation occurs less efficiently, meaning an accumulation of kinetic energy resides in the first baroclinic mode, and is captured at the sea surface. Scott and Wang (2005) then found an inverse cascade in the first baroclinic mode, which is contrary to classical geostrophic turbulence theory (Charney, 1971). A schematic of the energy cascade is illustrated in Fig. 1.2.2.

1.2.2 Eddy parameterisations

To better understand how the climate system is changing under increased greenhouse gas emissions, the scientific community typically employ global climate models (GCMs). GCMs include a variety of climate physics to model atmosphere, ocean, sea-ice, and land dynamics. Due to the size of the globe and the timescales needed (e.g. centennial), eddy-resolving ($1/10^{\circ}$) ocean models are impractical in terms of computational costs, and so GCM's often have coarse ocean resolution ($\sim 1^{\circ} \times 1^{\circ}$). The complex dynamics that take place below this coarse resolution (e.g. eddy transport) need to be represented in GCMs, and so numerous subgrid parameterisations have been devised (Moorthi and Suarez, 1992; Large et al., 1994; Gent and McWilliams, 1990). Two common eddy parameterisations exist, the Gent-McWilliams scheme (Gent and McWilliams, 1990) (GM), which parameterises the release of potential energy by baroclinic

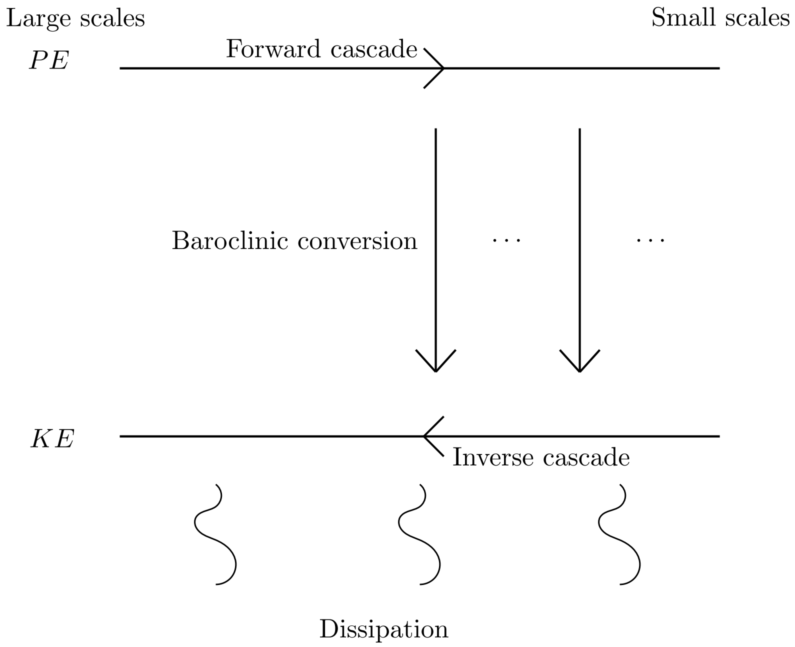

Figure 1.2.2: Schematic of energy cascade. Potential energy (PE) is supplied by external forcings such as large-scale winds, and then stirred by eddies, creating a forward cascade of PE from the largest to smallest scales. PE is then converted into kinetic energy (KE) by baroclinic conversion. KE then undergoes an inverse cascade where it is dissipated (e.g. by current-wind interactions, internal waves, or bottom drag), or transferred to larger scales.

instabilities, and the Redi scheme, which diffuses tracers along isopycnals (Redi, 1982). The GM scheme typically uses a variable coefficient, κ_{gm}, and can be thought of as an advective process (Gent et al., 1995). In contrast, the Redi scheme is employed as a diffusive process.

Since the inception of GM, improvements have been observed in the representation of global temperature distributions, ocean heat fluxes, deep-water formation, and model drift (Danabasoglu et al., 1994; Hirst and McDougall, 1996; Gordon et al., 2000; Griffies et al., 2015). Despite improvements to climate models, the GM scheme, by definition, releases potential energy, yet does not inject this energy into the kinetic energy field, rather it is dissipated. Based on the energy cascade theory discussed in section 1.2.1, this loss of energy caused by GM is inconsistent. Indeed, coarse resolution models that employ the GM scheme have much less kinetic energy than their eddy resolving counterparts (Kjellsson and Zanna, 2017). Kjellsson and Zanna showed that peak zonal jet velocities measured around 0.4 m s^{-1} in a high resolution model, but only 0.1 m s^{-1} in a coarse resolution model.

In order to resolve this loss of energy in coarse GCMs, GM type schemes have been proposed that calculate κ_{gm} based on a known eddy energy, providing a more energetically consistent eddy-induced advection. Eden and Greatbatch (2008) put forward a kinetic energy budget based eddy parameterisation, whereby the potential energy lost by the resolved flow is used as a source of subgrid scale kinetic energy. This new kinetic energy is then used to inform κ_{gm}, producing kinetic energy levels closer to those found in eddy-resolving ocean models. Building on this, Mak et al. (2017) utilised a variety of GM style coefficients and found the energy constrained form outlined in Marshall et al. (2012) improved simulations of the ACC through an emergence of eddy saturation. The form used by Mak et al is described by

$$\kappa_{gm} = \alpha E \frac{N}{M^2} \, , \tag{1.2.1}$$

where eddy energy is given by E, α is a non-dimensional tuning parameter, and M and N are horizontal and vertical buoyancy frequencies, respectively. This formulation of (1.2.1) has also been found to improve the sensitivity of ACC transport and the depth-integrated energy pattern in response to surface wind stress (Mak et al., 2018). Further parameterisations have also been developed, ensuring resolution aware GM coefficients (Jansen et al., 2019) and coupling GM with backscatter (Bachman, 2019), a process that re-injects the energy lost by the original GM scheme.

Nevertheless, using eddy energy to inform an appropriate GM style transfer coefficient in (1.2.1) requires knowledge of the eddy energy dissipation rate. Ill-constrained dissipation rates have recently been shown to affect Southern Ocean dynamics (Mak et al., 2022). In particular, Mak et al. show that varying the dissipation timescale can lead to monthly changes of around 20 Sv of ACC transport, 2 Sv of Atlantic Meridional Overturning Circulation, and 800 ZJ of ocean heat content anomaly. Such variation in ACC transport is significant when the total ACC transport is around 170 Sv (Donohue et al., 2016). Mak et al attributed these sensitivities to the fact that adding and removing energy from the system leads to changes in the isopycnals, and therefore impacting transport and heat content. In the next section, we will discuss in detail the various eddy energy dissipation mechanisms.

1.2.3 Eddy dissipation

A substantial amount of energy is supplied to the large-scale geostrophic circulation by atmospheric winds (~ 1 TW) (Wunsch, 1998), which makes its way into the mesoscale eddy field through a cascade of energy (Fig. 1.2.2). Mesoscale eddy energy is then dissipated and this dissipation has been attributed to a number of mechanisms, or in the words of Ferrari and Wunsch (2009) 'there are now too many candidates'. These candidates range from, but are not limited to, internal wave interactions, bottom drag, western boundary graveyard, and eddy-wind interaction. In this section we will discuss these eddy dissipation processes except eddy-wind interaction, which is presented in detail in section 1.2.4.

Near inertial waves

The interaction between mesoscale eddies and near-inertial waves has been considered as a mechanism for the exchange of energy in the ocean (Bühler and McIntyre, 2005; Polzin, 2010). Barkan et al. (2017) examined how eddy-wave interaction generated by a combination of low and high frequency wind induces a forward cascade to dissipation. They found a tenfold increase in dissipation of volume-averaged interior kinetic energy when eddies interacted with inertial waves. Moreover, cyclonic eddies exhibited 5 times the dissipation of anticyclones. Of the 0.5-1 TW of wind work on near inertial waves (Rimac et al., 2013), Barkan et al. estimated that eddy-wave interaction could dissipate

0.15-0.33 TW of geostrophic eddy kinetic energy. A recent study by Barkan et al. (2021) constrained this kinetic energy dissipation further by showing mesoscale eddies contained 25% less kinetic energy when internal waves were injected.

Bottom drag

Dissipation of eddy energy by bottom drag has been the focus of numerous studies and is a crucial element in the arrest of the energy cascade. Bottom drag has been shown to reduce the inverse barotropic cascade and its downwards vertical transfer of eddy kinetic energy, subsequently enhancing surface baroclinicity (Scott and Arbic, 2007; Trossman et al., 2017). Studies have also attempted to quantify the dissipation of energy by bottom drag processes. In a study by Sen et al. (2008) who employed data from near bottom moored current meters, a value of 0.2 TW globally was estimated to be removed by quadratic bottom drag. This value was also verified by Huang and Xu (2018) who found a slightly larger value of 0.26 TW, with a dominant Southern Ocean component of eddy kinetic energy dissipation. Huang and Xu also suggested that bottom dissipation could incorporate other damping mechanisms, such as lee waves and topographic blocking. Indeed, Yang et al. (2018) found that in the Southern Ocean, 0.12 TW of eddy energy was lost due to lee wave generation over rough topography. The addition of rough topography in an idealised western boundary set-up also enhanced the dissipation of eddy energy and was thought to be a result of lee waves (Yang et al., 2021).

Western boundary graveyard

The western boundary graveyard is a relatively new idea for eddy dissipation, and essentially involves the loss of eddy energy as mesoscale eddies propagate into the western boundary from the ocean interior. It was first proposed by Zhai et al. (2010) who set out to establish where eddies are dissipated, suggesting that once eddies reach the western boundary, their energy scatters to higher vertical modes and dissipates through viscous processes. In contrast, Tedesco et al. (2022) examined the evolution of eddy energy at a western boundary current, showing that the loss of eddy energy is a result of eddy-mean interactions, bottom friction, and a transfer to higher vertical baroclinic modes that do not undergo immediate dissipation.

1.2.4 Relative wind stress

Before discussing the dissipation of mesoscale eddies by eddy-wind interaction, we first discuss the prominent studies that raised the importance of this mechanism at the air-sea interface.

Surface atmospheric wind stress is parameterised using the following bulk formula

$$\boldsymbol{\tau}_{abs} = \rho_a C_d |\boldsymbol{u}_a| \boldsymbol{u}_a \ , \tag{1.2.2}$$

where ρ_a is air density, C_d is a drag coefficient, which is a function of wind speed, and $\boldsymbol{u}_a$ is a wind velocity 10 m above the ocean surface. This equation is termed *absolute wind stress* since it uses the absolute wind speed, $|\boldsymbol{u}_a|$, and assumes ocean current speeds are much smaller than the 10 m wind speed. The work done by wind stress $\boldsymbol{\tau}$, on the ocean surface $\boldsymbol{u}_s$, is described using

$$W = \boldsymbol{\tau} \cdot \boldsymbol{u}_s \ . \tag{1.2.3}$$

Using this formulation, Wunsch (1998) attempted to quantify the global integral of work done (*total wind power input*) by winds using (1.2.3) with (1.2.2). Wunsch used sea surface height data derived from satellite data products and found a total wind power input into the geostrophic ocean circulation of 0.88 TW, with around 90% of this value arising from the time-mean zonal wind stress and zonal geostrophic surface currents. Unsurprisingly, regions of the largest wind work were the western boundary current systems and the Southern Ocean. Prior to this work by Wunsch, some studies highlighted the importance of including an ocean surface current, $\boldsymbol{u}_s$, in the wind stress bulk formula. This formula is given by

$$\boldsymbol{\tau}_{rel} = \rho_a C_d |\boldsymbol{u}_a - \boldsymbol{u}_s| (\boldsymbol{u}_a - \boldsymbol{u}_s) \ , \tag{1.2.4}$$

and is termed *relative wind stress*, since it accounts for the relative motion between wind and ocean currents. The difference between absolute and relative wind stress is marginal (typically $\sim 1-2\%$) (Dawe and Thompson, 2006), though this has been shown to have a large impact on the ocean circulation. Pacanowski (1987) argued that ocean current velocities in the equatorial region could not be ignored since they were on the same order of magnitude as the wind [$O(1 \text{ m s}^{-1})$]. Pacanowski found current speeds in their model were reduced by around 30% when (1.2.4) was used instead of (1.2.2). Duhaut and Straub (2006) later considered the effect of using relative wind stress in a calculation of the total wind power input using a quasi-geostrophic double-gyre simulation, finding a reduction in wind power input of around 20-35% when using relative wind stress. In this work by Duhaut and Straub, eddies were realised to contribute to around a third of the reduction in total wind power input. In terms of the wind power input in to the ocean general circulation, Hughes and Wilson (2008) quantified this as 0.76 TW when using relative wind stress, a reduction on the value found by Wunsch (1998). It is clear that including the ocean surface current in the wind stress could have profound impacts on the large-scale geostrophic ocean circulation. In addition, wind work is also carried out on the ageostrophic ocean circulation, accounting for processes within the surface Ekman layer such as turbulence and mixing, as well as near-inertial motions. Wang and Huang (2004) found a wind power input of 3 TW into the Ekman layer, whilst Torres et al. (2022) revealed 5 TW of energy is supplied by winds to the combined geostrophic and ageostrophic ocean circulation.

One of the first studies to highlight the impact of relative wind stress on ocean eddies was that by Dewar and Flierl (1987). They revealed the eddy current

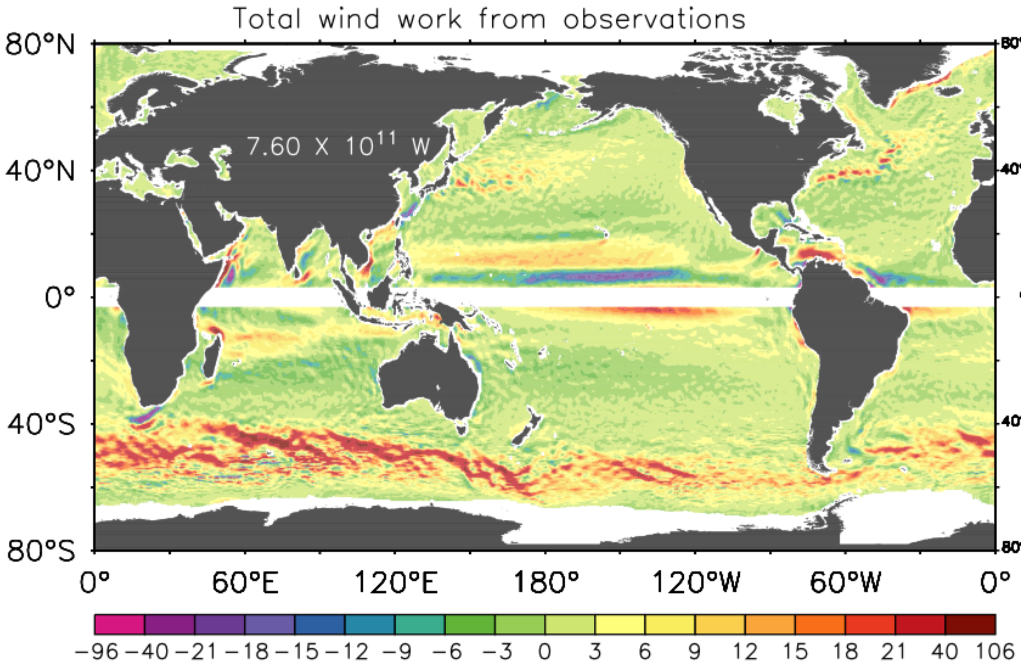

Figure 1.2.3: Total wind work over the global ocean. Units in 10^{-3} W m^{-2}. Source: Hughes and Wilson (2008).

played the role of a 'top drag' mechanism in the wind stress, enabling the decay of eddy interior motions. Zhai and Greatbatch (2007) looked at a model of the northwest Atlantic Ocean, home to the energetic Gulf Stream, and showed relative wind stress reduced the wind power input by 17% and eddy kinetic energy by 10%. Additional studies have further explored the role of relative wind stress on wind power input and damping of eddy kinetic energy (Seo et al., 2016; Renault et al., 2016b; Oerder et al., 2018), establishing its importance for eddy dissipation. In fact, Xu et al. (2016) determined a global integral of wind work on mesoscale eddies using relative wind stress to be around 27 GW, which produced an eddy decay timescale in the range of 1.6-3.7 years. This timescale compared well with the eddy lifetime of ~ 8 months put forward by Chelton et al. (2011).

Figure 1.2.4 illustrates how relative wind stress damps mesoscale eddies. Consider a large-scale background wind that blows over an isolated eddy with clockwise rotation. Without the eddy current in the wind stress (1.2.2), the wind stress is constant over the eddy (Fig. 1.2.4a). For the wind work on the eddy, the wind stress is multiplied by the eddy current. The eddy current is positive in the north and negative in the south, and since the wind stress is constant, the respective wind work at each side of the eddy is equal in magnitude but opposite in sign. The total wind power input is then $P_{abs} = 0$, implying absolute wind stress does no net wind work on the eddy. However, including the eddy current in (1.2.4) modifies the wind stress over the eddy and generates more (less) negative (positive) wind work at the south (north) side of the eddy (Fig. 1.2.4b). The total wind power input is then $P_{rel} < 0$ because $\boldsymbol{\tau}_{rel}$ is larger on the south side, where $\boldsymbol{\tau}_{rel} \cdot \boldsymbol{u}_s$ is negative. Therefore, relative wind stress damps the eddy.

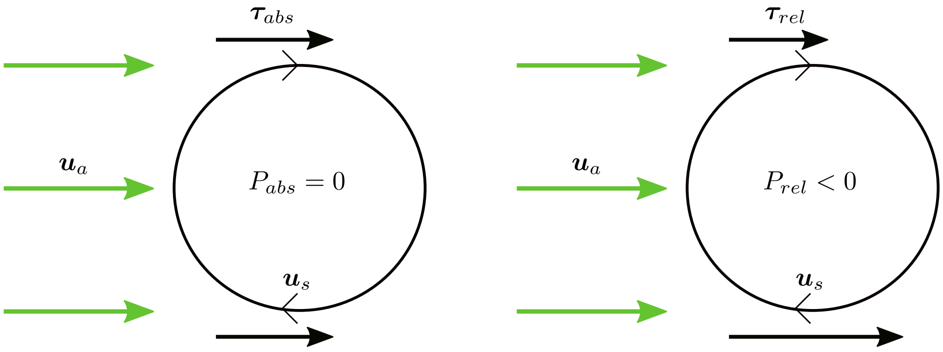

a) Absolute wind stress

b) Relative wind stress

Figure 1.2.4: Schematic depicting changes in wind stress ($\boldsymbol{\tau}$) and wind power input (P) over a clockwise rotating eddy. In a) absolute wind stress, and b) relative wind stress. Source: Wilder et al. (2022).

As we have seen, relative wind stress reduces the wind power input into the large-scale ocean circulation and damps mesoscale eddies. Recent work has now been carried out to establish what effect relative wind stress has on the climate system. In a study by Wu et al. (2017), the impact of relative wind stress on ocean heat transport and overturning circulations on decadal timescales was investigated in an eddy-permitting model. Relative wind stress was shown to reduce the Atlantic meridional overturning circulation from 20.6 Sv down to 18 Sv, which subsequently reduced the northward global ocean heat transport from 1.7 to 1.5 PW. In a Southern Ocean model, work by Munday et al. (2021) demonstrated that neglecting the ocean current in the wind stress could lead to an enhanced southward heat transport into the seasonal sea-ice zone. Various improvements have also been made to ocean current systems and eddy trajectories when employing relative wind stress. In an ocean-atmosphere coupled model, McClean et al. (2011) found an improvement in the variability of mesoscale eddies in the Agulhas region. Renault et al. (2019) found the Gulf Stream track matched the observed path when relative wind stress is used, in response to the damping of the energy cascade.

1.2.5 Eddy stability

There are clear mechanisms associated with the decay of mesoscale eddies; however, eddy longevity can also be modulated by their stability characteristics. For example, vertical and horizontal structures have been shown to affect the stability of mesoscale eddies.

Horizontal profiles of eddies are typically described using an exponential function

$$\eta = Ae^{-(r^{\alpha})/R^{\alpha}} , \tag{1.2.5}$$

where η is the sea surface height, A is the eddy amplitude, R is the eddy radius, and α is a steepness parameter. When $\alpha = 2$, this is referred to as a Gaussian eddy (Chelton et al., 2011).

The horizontal profile of Gaussian eddies can be thought of as monopolar, meaning a central relative vorticity sign is surrounded by an oppositely signed relative vorticity, and is considered an unstable profile (Carton et al., 1989). Gent and McWilliams (1986) studied the stability of barotropic columnar vortices for a variety of steepness values and found that larger α leads to a barotropically unstable eddy with azimuthal wavenumber, $l = 1$. Stegner and Dritschel (2000) used the 1-1/2 layer shallow water equations and also found the steepness parameter to be important in the stability of anticyclonic and cyclonic eddies. Stegner and Dritschel revealed an asymmetry in growth rates of the most unstable mode (azimuthal mode $l = 2$), with cyclones being more unstable than anticyclones when set up with equivalent velocity profiles.

Ageostrophic effects are thought to play a part in this eddy asymmetry. With increasing ageostrophy, measured by relative vorticity over Coriolis parameter, anticyclones stabilise and cyclones become more unstable (see Fig. 6 in Stegner and Dritschel (2000)).

Baroclinic eddies exhibit depth dependent flow that can alter the outcome of their evolution. In a two-layer quasi-geostrophic simulation, Ikeda (1981) established that an increase in baroclinic shear leads to a decrease in eddy stability and ultimate breakup of the original monopole eddy into two dipolar eddies. Helfrich and Send (1988) argued that barotropic flow could act as a stabilising mechanism in this two-layer setup. A counter-rotating deep flow - a flow opposing the surface flow - was later revealed by Dewar and Killworth (1995) to be the reason for eddy destabilisation. Eddies that have co-rotating flows, increased barotropic flow, display weak, or no unstable modes and also persist for much longer in time.

Dewar et al. (1999) further examined the apparent longevity of observed eddies. Eddies with opposing radial potential vorticity gradients between the upper and lower layer are baroclinically unstable, and also present large growth rates in the azimuthal mode, $l = 2$. It was shown that anticyclonic eddies stabilised abruptly when transitioning from a counter- to co-rotating regime, whilst co-rotating cyclonic eddies still exhibited a marginal unstable mode. Katsman et al. (2003) conducted a linear stability analysis, finding a change in growth rates of the most unstable mode as the eddy transitions between counter and co-rotating. Baroclinic instability is dominant in counter-rotating eddies, but in co-rotating eddies, barotropic mechanisms work against baroclinic processes, and act to stabilise the eddy. Further stability analyses by Mahdinia et al. (2017) highlight an asymmetry in modal growth rates between anticyclones and cyclones, showing that even eddy polarity can impact eddy longevity. Sutyrin (2016) modified the counter-rotating eddy setup of Dewar et al. (1999) by adding a middle layer of uniform potential vorticity, which subsequently stabilised the eddy, lengthening its lifetime, and preventing dipolar formation.

Currently, we know that relative wind stress damps the energy cascade and stabilises ocean current systems in coupled climate models (Renault et al., 2019). However, in spite of the research into eddy stability, it is not yet known whether relative wind stress could impact the stability of a mesoscale eddy. Therefore, one aim of this thesis is to investigate the impact of relative wind stress on mesoscale eddy stability.

1.3 A general overview of the general circulation model

This thesis will use a general circulation model, where detailed model setups are given in each chapter that lay out the specifics to reproduce each chapter experiment. Here, we give a general overview and description of the configuration used in the general circulation model, though not everything outlined here is used across all experiments.

The model employed is the Massachusetts Institute of Technology general circulation model (MITgcm) (Marshall et al., 1997a,b). This model can be used to simulate a wide variety of ocean and atmospheric processes across idealised, regional, and global configurations. Here we apply the MITgcm in ocean-only mode with parameterisations used to represent particular interactions at the air-sea interface e.g. momentum.

1.3.1 Equations and schemes

The MITgcm uses the Boussinesq, incompressible, and hydrostatic primitive equations in z-coordinates. The momentum equations are stepped forward in time using the second-order Adams-Bashforth method. Non-divergence of the flow is maintained by utilising the Arakawa C grid, which staggers the flow components in space. The thermodynamic equation employs a staggered time-stepping method that calculates variables using the most recent flow field, adding extra accuracy and stability. The advection of temperature makes use of the Prather scheme (Prather, 1986). This scheme ensures frontal features are properly represented and also limits spurious diapycnal mixing (Hill et al., 2012).

1.3.2 Viscosity and diffusion

The inclusion of viscous and diffusive processes in general circulation models is employed to maintain numerical stability, as well as offering dissipation of energy and diffusion of tracers at the grid scale (Jablonowski and Williamson, 2011). A biharmonic operator is considered an appropriate tool for numerical stability and friction purposes, as opposed to the Laplacian (Holland, 1978). If a Laplacian form of friction is used at a limit that prevents numerical instabilities, then an excessive amount of kinetic energy will likely be removed (Griffies and Hallberg, 2000). This is not the case for biharmonic friction, which is capable of damping instabilities but only removing minimal kinetic energy due to its scale selectivity. Therefore, a biharmonic friction parameter is chosen for momentum closure in this model. In terms of diffusion, again the biharmonic operator is used as this works to diffuse tracers at the smallest scales and allow the large-scale processes to mostly evolve.

1.3.3 Wind stress forcing

The parameterisation of surface wind stress is achieved using a bulk formula. For atmospheric winds, a wind stress described in Eq. (1.2.4), which is relative wind stress, is used for the stress arising due to winds over ocean currents. The drag coefficient, C_d, in Eq. (1.2.4) is formulated in Large and Yeager (2004), and ensures that changes in relative wind speed also impact the value of C_d.

1.3.4 Boundary conditions

Re-entrant boundary conditions are the default MITgcm conditions, and are used in these model experiments. Re-entrant boundaries allows the flow to leave the domain through one boundary edge and enter through the opposing side, and is suitable for the idealised studies we wish to carry out. In all model experiments, the eddy is placed at the centre of a large square domain. As the eddy evolves in time, waves are emitted that propagate towards the boundaries, and with re-entrant boundary conditions, can re-enter the domain and interact with the eddy. To avoid this, the restoring boundary condition package is employed in the MITgcm. A temperature sponge layer can be applied and restored daily so any temperature signals from the eddy are not able to re-enter the domain through the boundaries.

1.4 Thesis contribution to literature

This thesis aims to investigate, as a direct dissipation pathway of mesoscale eddy energy, relative wind stress. To date, studies have examined eddy energy in regional models in response to relative wind stress, revealing significant weakening of the eddy field and subsequent impacts to the climate system (McGillicuddy et al., 2007; Seo et al., 2016; Renault et al., 2019; Chen et al., 2020). Furthermore, energy budget-based eddy parameterisations are now proving useful (Mak et al., 2017). However, constrained eddy dissipation rates are still lacking (Mak et al., 2022). To our knowledge, there are limited studies that have attempted to quantify this damping in both theoretical and idealised settings, choosing to focus on seas of eddies, rather than a single isolated eddy. Investigating this interaction could possibly pave the way for future eddy-wind parameterisations that are missing from current global climate models, whilst also bringing to light key eddy dynamic responses to relative wind stress.

The first goal of this thesis is to verify whether the damping of anticyclonic and cyclonic total eddy energy by relative wind stress can be predicted using theory and analytical equations. In chapter 2, we first derive an analytical expression for the total wind power input into a Gaussian shaped eddy. This is then used to predict the decay of energy in a barotropic eddy by using a single-layer shallow water model. Results from this prediction are then validated by comparing them against a high resolution model, MITgcm (see section 1.3 for information on MITgcm). A decay timescale is also derived and compared with past estimates given by Gaube et al. (2015) and Xu et al. (2016). In chapter 3, we build on work from the previous chapter by considering the fact that the ocean's sea surface height primarily reflects the first baroclinic mode structure (Wunsch, 1997). This justifies the use of a two-layer shallow water model to theoretically predict the decay of energy in a baroclinic eddy, with results compared to continuously stratified MITgcm simulations.

In chapter 4, we conduct a dedicated study of an idealised anticyclonic mesoscale eddy when forced by relative wind stress. There are few, if any, idealised single eddy studies that have quantified eddy energy and its response to relative wind stress, therefore this work attempts to fill this gap in the literature. This work begins by examining the wind stress-induced vertical motions in the eddy. Next, we quantify the effects of relative wind stress on mean eddy energetics, and contrast with results from past studies (Renault et al., 2018; Shan et al., 2020). A scaling argument is also derived that supports the numerical findings. The work is concluded with an examination of the eddy's stability via turbulent fluxes and potential vorticity.

The final chapter looks at the sensitivity of the eddy response to relative wind stress due to changes in eddy parameters. This aims to establish under what conditions relative wind stress could impart a different effect on mesoscale eddies. We first explore the response of a cyclonic eddy to relative wind stress, highlighting energetic and stability differences compared with the anticyclonic eddy shown in chapter 4. We then investigate the impact of relative wind stress on an anticyclonic eddy that contains a smaller baroclinic component.

In chapter 6, we conclude this thesis with a summary of our findings, along with their respective limitations and suggestions for improvements. Further considerations are also made for additional studies into idealised eddy energetic studies, in particular a consideration towards the thermodynamic pathway and submesoscale.

2

Predicting the Damping of a Barotropic Eddy by Relative Wind Stress

As discussed in chapter 1, new eddy parameterisations based on energy budgets require a constrained dissipation rate (Mak et al., 2022). Indeed, eddy dissipation by relative wind stress is recognised as a significant candidate (Xu et al., 2016). Therefore, the main purpose of this chapter is to design an initial theoretical framework to predict the damping of barotropic total eddy energy in response to relative wind stress. The choice of a barotropic eddy is employed for its simplicity so that we can verify whether an analytical expression can be used to predict the decay of eddy energy. The framework of this analytical work will be devised around a few key eddy parameters, such as sea surface height, eddy radius, and ocean depth. This work is presented as the first step in constraining a dissipation rate for mesoscale eddies due to relative wind stress.

We begin this chapter by deriving an analytical equation for wind power input by relative wind stress. This is achieved by making use of simple theory obtained through observations (Chelton et al., 2011). A barotropic eddy energy equation is presented, and used to predict the damping of total eddy energy based on the eddy's sea surface height. A high resolution general circulation model is used to simulate a barotropic mesoscale eddy in response to relative wind stress forcing. The prediction and model simulation are compared to verify the analytical wind power input. We then consider under what parameters this prediction method breaks down, as well as the sensitivity to increased wind speeds. Spatial patterns of the model simulation are then investigated. Our findings are then summarised, with motivations given for chapter 3.

2.1 Theoretical components

2.1.1 Wind power input

We begin our theoretical framework by deriving the analytical expression for wind power input into the geostrophic surface motion. The total wind power input is given by

$$P = \int_S W\, dS = \int_S \boldsymbol{\tau} \cdot \boldsymbol{u}_{gs}\, dS \tag{2.1.1}$$

where $\boldsymbol{u}_{gs} = (u, v)$ are geostrophic horizontal velocity components at the sea surface, $\boldsymbol{\tau}$ is the wind stress, W is wind work, $\int \cdot dS$ is a horizontal integral over x and y space, and subscripts $\cdot_{gs}$ denote geostrophic surface. In order to derive this expression, analytical equations that describe a mesoscale eddy need to be introduced. We also re-introduce the wind stress parameterisations.

Analytical eddy

Eddies typically have a small Rossby number (Chelton et al., 2011), meaning their surface horizontal velocities are approximately in geostrophic balance, i.e.

$$u_{gs} = -\frac{g}{f}\frac{\partial \eta}{\partial y}\ , \tag{2.1.2a}$$

$$v_{gs} = \frac{g}{f}\frac{\partial \eta}{\partial x}\ , \tag{2.1.2b}$$

where f is the Coriolis parameter, g is the gravitational acceleration, and η is the sea surface height. Based on altimetry observations, eddy sea surface height, η, can be approximated using a Gaussian function (Chelton et al., 2011), given by

$$\eta = Ae^{-(x^2+y^2)/R^2} \,, \tag{2.1.3}$$

where A is the eddy amplitude, and R is the e-folding radius (point of zero relative vorticity). In addition, maximum geostrophic velocities occur at $L_s = 2^{-1/2}R$ (Chelton et al., 2011), which is the speed based radius. Chelton found (2.1.3) to approximate the inner 2/3rds of the average eddy sea surface height, making it a suitable equation to utilise in our theoretical framework. Examples of sea surface height and zonal velocities for a Gaussian eddy are shown in Fig. 2.1.1.

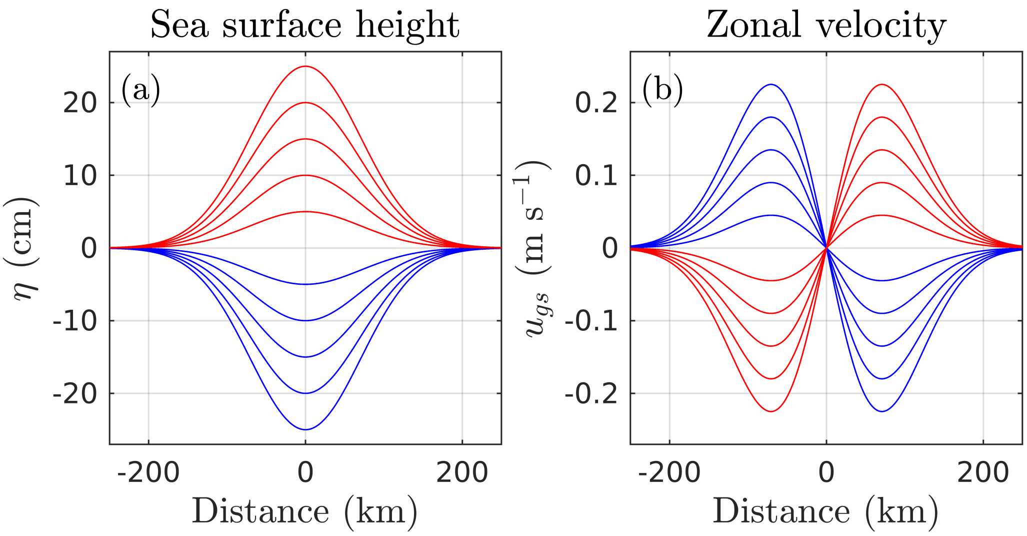

Figure 2.1.1: (a) Gaussian eddy sea surface height, η (in cm) and (b) zonal velocity component, u_{gs} (in m s^{-1}) for absolute amplitudes, $A = 5$, 10, 15, 20, 25 cm with e-folding radius, $R = 100$ km. Blue lines are cyclonic and red lines are anticyclonic. Velocity values in (b) increase with increasing absolute amplitude. Values are taken through the zonal origin, $x = 0$ km.

Wind stress parameterisation

A wind stress bulk formula describes the transfer of momentum between the atmosphere and ocean. Recall the absolute and relative wind stress bulk formulae described in chapter 1

$$\boldsymbol{\tau}_{abs} = \rho_a C_d \left|\boldsymbol{u}_a\right| \boldsymbol{u}_a \ , \tag{2.1.4a}$$

$$\boldsymbol{\tau}_{rel} = \rho_a C_d \left|\boldsymbol{u}_a - \boldsymbol{u}_{gs}\right| (\boldsymbol{u}_a - \boldsymbol{u}_{gs}) \ , \tag{2.1.4b}$$

where geostrophic surface velocities are employed.

To aid the derivation of the analytical wind power input, relative wind stress in (2.1.4b) is simplified by using an approximation due to Duhaut and Straub (2006) for the wind stress magnitude

$$\left|\boldsymbol{u}_a - \boldsymbol{u}_{gs}\right| \approx \left|\boldsymbol{u}_a\right| - \boldsymbol{u}_{gs} \cdot \boldsymbol{i} \ , \tag{2.1.5}$$

where $\boldsymbol{i}$ is a unit vector in the direction of the wind. Equation (2.1.5) assumes that only the wind aligned with the ocean current is the dominant contribution to the wind stress. Additionally, the drag coefficient, C_d, is a function of Eq. (2.1.5)

$$C_d = \frac{a_1}{\left|\boldsymbol{u}_a - \boldsymbol{u}_{gs}\right|} + a_2 + a_3 \left|\boldsymbol{u}_a - \boldsymbol{u}_{gs}\right| \ . \tag{2.1.6}$$

Equation (2.1.6) is taken from Large and Yeager (2004) and is introduced to account for changes in drag due to eddy currents. The constants in Eq. (2.1.6) are: $a_1 = 0.0027$ m s^{-1}; $a_2 = 0.000142$; $a_3 = 0.0000764$ m^{-1} s. The varying C_d formulation is also used in the MITgcm model, and is why we choose it over a constant value.

Visualising wind stress differences

The difference between absolute (Eq. (2.1.4a)) and relative (Eq. (2.1.4b)) wind stress is

$$\boldsymbol{\tau}_{diff} = \boldsymbol{\tau}_{abs} - \boldsymbol{\tau}_{rel} = \rho_a C_d \big(\left|\boldsymbol{u}_a\right| \boldsymbol{u}_{gs} + (\boldsymbol{u}_{gs} \cdot \boldsymbol{i}) \boldsymbol{u}_a - (\boldsymbol{u}_{gs} \cdot \boldsymbol{i}) \boldsymbol{u}_{gs} \big) \ , \tag{2.1.7}$$

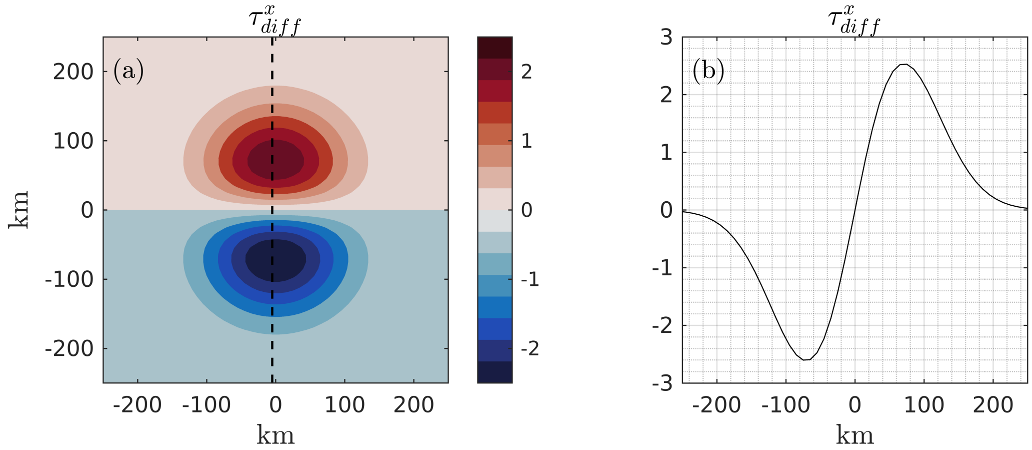

Figure 2.1.2: Difference between absolute and relative wind stress, τ^x_{diff}, for a uniform background wind of 7 m s^{-1} over a clockwise rotating Gaussian eddy with amplitude 15 cm, radius 100 km, and latitude 40°. In (a) contour of τ^x_{diff} , and (b) north-south cross section of $\boldsymbol{\tau}_{diff}$ through origin $x = 0$. τ^x_{diff} is in units of 10^{-3} N m^{-2}. Air density, $\rho_a = 1.2$ kg m^{-3}. Formulation for C_d is (2.1.6).

where $\boldsymbol{\tau}_{diff}$ is made up of a contribution of linear drag on the ocean surface velocity by the wind (first two terms on rhs), and a counteracting force by the ocean current (last term on rhs). In (2.1.7), C_d is kept as a constant for simplicity and to highlight the key differences between absolute and relative wind stress in their equation form, but varies according to (2.1.6) for Figs. 2.1.2 and 2.1.3. Figure 2.1.2a shows the spatial pattern of τ^x_{diff} for a uniform west to east background wind over a clockwise rotating Gaussian eddy (see section 2.2 for choice of wind velocity). The dipole pattern is born as a result of the eddy current in $\boldsymbol{\tau}_{rel}$, where the positive (negative) pole is due to a reduction (increase) in wind stress being imposed due to the eddy current. The south pole has a marginally larger wind stress - around 4% in absolute terms - than the north dipole since the wind opposes the eddy currents clockwise flow. This can be seen by comparing the maximum and minimum points in Fig. 2.1.2b for a north-south cross section through the origin of τ^x_{diff}.

The effects of the ocean surface velocity on wind work over the eddy are explored next. Wind work for each wind stress formula is shown in Fig. 2.1.3. Using relative wind stress reduces the amount of positive work done by the wind to the north and increases negative wind work to the south, in contrast to absolute

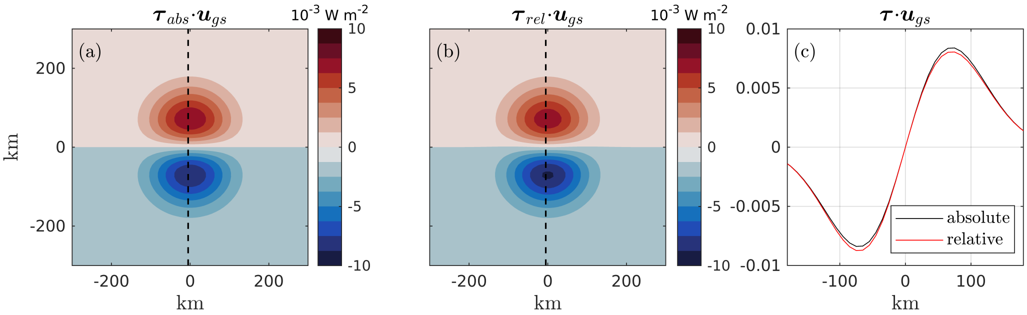

Figure 2.1.3: Work done using a uniform background wind of 7 m s^{-1} over a clockwise rotating Gaussian eddy with amplitude 15 cm, radius 100 km, and latitude 40°. In (a) $\boldsymbol{\tau}_{abs} \cdot \boldsymbol{u}_{gs}$, (b) $\boldsymbol{\tau}_{rel} \cdot \boldsymbol{u}_{gs}$, and (c) north-south cross section of absolute (black) and relative (red) wind work through origin $x = 0$. Units of wind work in 10^{-3} W m^{-2}. Air density, $\rho_a = 1.2$ kg m^{-3}. Formulation for C_d is (2.1.6).

wind stress (Fig. 2.1.3a,b). Cross sections (Fig. 2.1.3c) highlight north-south differences in wind work due to the eddy current. The increase in negative wind work and decrease in positive wind work from relative wind stress shows how it is an eddy damping mechanism.

Analytical wind power input

Finding the analytical wind power input begins by taking the dot product of $\boldsymbol{\tau}_{rel}$ and $\boldsymbol{u}_{gs}$, using (2.1.5), then expanding into component form,

$$W = \boldsymbol{\tau}_{rel} \cdot \boldsymbol{u}_{gs} \ , \tag{2.1.8a}$$

$$W = \rho_a \left(\frac{a_1}{|\boldsymbol{u}_a - \boldsymbol{u}_{gs}|} + a_2 + a_3 \left| \boldsymbol{u}_a - \boldsymbol{u}_{gs} \right| \right) \left| \boldsymbol{u}_a - \boldsymbol{u}_{gs} \right| (\boldsymbol{u}_a - \boldsymbol{u}_{gs}) \cdot \boldsymbol{u}_{gs} \ , \tag{2.1.8b}$$

$$\begin{aligned} W = \rho_a \Big[& a_1 (u_a u_{gs} - u_{gs}^2 - v_{gs}^2) + \\ & a_2 (|u_a| \, u_a u_{gs} - |u_a| \, u_{gs}^2 - u_a u_{gs}^2 + u_{gs}^3 - |u_a| \, v_{gs}^2) + \\ & a_3 (|u_a|^2 \, u_a u_{gs} - |u_a|^2 \, u_{gs}^2 + u_a u_{gs}^3 - 2 \, |u_a| \, u_a u_{gs}^2 + 2 \, |u_a| \, u_{gs}^3 - |u_a|^2 \, v_{gs}^2) \Big] \ . \end{aligned} \tag{2.1.8c}$$

The wind vector is assumed constant in the zonal direction, and no meridional component exists (i.e. $v_a = 0$). Terms of $\boldsymbol{u}_{gs}^4$ in (2.1.8c) are neglected. Next, analytical horizontal velocities are found by using the Gaussian sea surface height

(2.1.3) and the geostrophic balance horizontal velocities (2.1.2)

$$(u, v)_{gs} = \left(\frac{g}{f}\frac{2Ay}{R^2}\eta,\ \frac{g}{f}\frac{2Ay}{R^2}\eta\right) . \tag{2.1.9}$$

The total wind power input for relative wind stress can be found by integrating Eq. (2.1.8c) in the limits of $x, y \to \pm\infty$,

$$P = \int_{-\infty}^{\infty}\int_{-\infty}^{\infty} W\ dxdy , \tag{2.1.10a}$$

$$P = -\rho_a\Big(2a_1 + 3a_2\,|u_a| + 4a_3\,|u_a|^2\Big)\frac{g^2A^2\pi}{2f^2} . \tag{2.1.10b}$$

The solution shown in Eq. (2.1.10b) implies that any uniform background wind will remove power from the eddy regardless of direction, since it depends on the magnitude of the wind and not its sign. Also, the eddy polarity (sign of A) has no effect on the sign of the power input due to the quadratic dependence. Therefore, anticyclonic or cyclonic eddies should undergo equal amounts of wind damping when their amplitudes are the same. It was shown in Fig. 2.1.3a that there was equal positive and negative wind work over the eddy, and it is for this reason that wind power input for absolute wind stress is zero. It is also interesting to note the lack of dependence of P on the eddy e-folding radius, R. This is because through the spatial integral of wind work to the limits of ∞, R cancels out, meaning the sum of positive and negative wind work will not change with increasing radius.

Suppose that a constant drag coefficient is used in the wind power input, then the wind power input will be,

$$P = -3\rho_a C_d\,|u_a|\,\pi\frac{g^2A^2}{2f^2} . \tag{2.1.11}$$

This equation is analogous to forms found in Gaube et al. (2015); Jullien et al. (2020). The difference between Eq. (2.1.10b) and (2.1.11) is that the first and last terms inside the brackets of Eq. (2.1.10b) are not included, and $a_2 = C_d$.

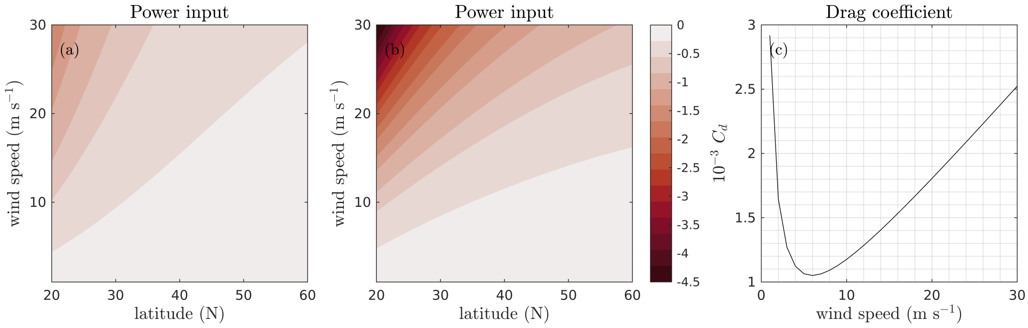

Figure 2.1.4: Wind power input P (in W) for varying latitude (deg N) as a function of wind velocity u_a (m s^{-1}) for an eddy with amplitude 15 cm and radius 100 km. In (a) constant drag coefficient of 1.1×10^{-3} (2.1.10b), (b) non-constant drag coefficient (2.1.11), and (c) drag coefficient C_d as a function of wind speed $\boldsymbol{u}_a$ only. Wind power input in units of 10^8 W. Air density, $\rho_a = 1.2$ kg m^{-3}.

Figure 2.1.4a,b shows how the wind power input varies for a constant and non-constant drag coefficient. For wind speeds around 7 m s^{-1} near to 40°N there is little variation between each wind power input. This is because C_d in the non-constant solution is near to the constant value of 1.1×10^{-3} (Fig. 2.1.4c). For higher wind speeds, e.g. 25 m s^{-1}, the wind power input at 40°N is markedly different (60% damping increase for non-constant C_d against constant C_d - values not shown explicitly). Again, the explanation is down to the value of the drag coefficient, where the non-constant C_d is double (2.2×10^{-3}) the value of the constant C_d. Moreover, for small wind speeds (e.g. 2 m s^{-1}), the wind power input is close to zero in each case, showing the convergence of relative wind power input towards absolute wind power input in this case. What this brief analysis shows is that wind speed variations in C_d should be accounted for when calculating the wind power input by relative wind stress, particularly for high wind speed events.

2.1.2 Barotropic energy equation

A barotropic eddy can be thought of as being a homogeneous ocean slab with a surface displacement. A schematic of this setup is shown in Fig. 2.1.5, which also shows a wind stress acting on the ocean surface. To predict eddy energy, the total energy equation for the barotropic eddy needs to be found. In this section, velocities are assumed to be geostrophic.

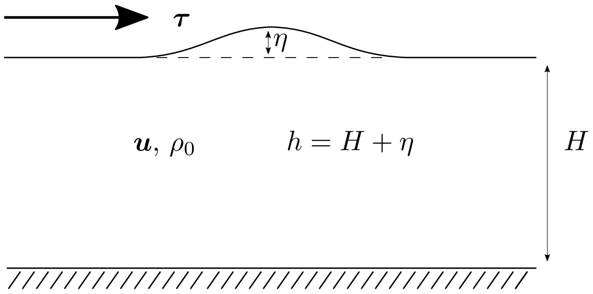

Figure 2.1.5: Schematic showing model setup for a barotropic eddy.

The shallow water equations with the hydrostatic approximation are used to describe the barotropic eddy

$$\frac{D\boldsymbol{u}}{Dt} + f\boldsymbol{k} \times \boldsymbol{u} = -g\nabla_h \eta + \frac{\boldsymbol{\tau}}{\rho_0 h} \ , \tag{2.1.12a}$$

$$\frac{\partial h}{\partial t} + \nabla_h \cdot (h\boldsymbol{u}) = 0 \ , \tag{2.1.12b}$$

where $\boldsymbol{u} = (u, v)$ are horizontal velocities, ρ_0 is a reference ocean density, $h = H + \eta$, with H being the resting depth of the ocean and η being the surface displacement, $\boldsymbol{k}$ is a vertical unit vector, and ∇_h is a horizontal gradient. Equation (2.1.12a) is the horizontal momentum equations, and Eq. (2.1.12b) is the continuity equation. Also,

$$\frac{D}{Dt} = \frac{\partial}{\partial t} + u\frac{\partial}{\partial x} + v\frac{\partial}{\partial y} \ , \tag{2.1.13}$$

is the material derivative.

The kinetic energy equation is found by multiplying (2.1.12a) by $h\boldsymbol{u}$

$$\frac{\partial}{\partial t}\Big(h\frac{1}{2}\boldsymbol{u}\cdot\boldsymbol{u}\Big) + \nabla_h \cdot \Big(\big(\frac{1}{2}\boldsymbol{u}\cdot\boldsymbol{u} + g\eta\big)h\boldsymbol{u}\Big) - g\eta\nabla_h \cdot (h\boldsymbol{u}) = \frac{\boldsymbol{\tau}\cdot\boldsymbol{u}}{\rho_0} \ , \tag{2.1.14}$$

where use of the vector invariant identity $(\boldsymbol{u}\cdot\nabla)\boldsymbol{u} = (\nabla\times\boldsymbol{u})\times\boldsymbol{u} + \nabla\frac{1}{2}\boldsymbol{u}\cdot\boldsymbol{u}$ and continuity equation (2.1.12b) has been made. The potential energy equation is found by multiplying Eq. (2.1.12b) by $g\eta$,

$$\frac{\partial}{\partial t}\Big(\frac{1}{2}g\eta^2\Big) + g\eta\nabla_h \cdot (h\boldsymbol{u}) = 0 \; . \tag{2.1.15}$$

Adding kinetic (2.1.14) and potential (2.1.15) energy equations, the total energy equation for a barotropic eddy can be described by

$$\frac{\partial}{\partial t}\rho_0\Big(h\frac{1}{2}\boldsymbol{u}\cdot\boldsymbol{u} + \frac{1}{2}g\eta^2\Big) + \nabla_h \cdot \Big(\rho_0(g\eta + \frac{1}{2}\boldsymbol{u}\cdot\boldsymbol{u})h\boldsymbol{u}\Big) = W \; , \tag{2.1.16}$$

where kinetic energy and potential energy make up the first two terms in the brackets on the left hand side, respectively, the second term on the left is the divergence of kinetic and potential energy, and the term on the right hand side is work done by wind on the eddy. Equation (2.1.16) in domain integrated form is

$$\frac{\partial}{\partial t}(KE + PE) = P \; , \tag{2.1.17}$$

where the divergence of energy is zero under no normal flow, or re-entrant boundary conditions. An expression for P has been derived in section 2.1.1; we now derive an expression for $KE + PE$. This is done by employing the Gaussian sea surface height (2.1.3) and the geostrophic velocities (2.1.2) and inputting into the following integral

$$KE + PE \equiv E = \int_S \rho_0\Big(h\frac{1}{2}\boldsymbol{u}\cdot\boldsymbol{u} + \frac{1}{2}g\eta^2\Big)\, dS \; , \tag{2.1.18}$$

to give

$$KE + PE \equiv E = \rho_0\Big(\Big(\frac{g^2H\pi}{2f^2} + \frac{gR^2\pi}{4}\Big)A^2 + \frac{2g^2\pi}{9f^2}A^3\Big) \; . \tag{2.1.19}$$

Combined kinetic and potential energy depend on key eddy parameters, such as eddy amplitude, A and eddy radius, R. Equation (2.1.22) can be used to predict eddy energy evolution over time.

2.1.3 Outline of prediction method

The method to predict eddy energy is now presented. The prediction method is primarily dependent on the eddy amplitude as initial energy and wind damping are calculated using this term.

1. **Find the initial energy of the eddy,** $E^{n=1}$.

   Initial energy is found using Eq. (2.1.19)

   $$E^n = C(A^n)^2 + D(A^n)^3 \ , \tag{2.1.20}$$

   where

   $$C = \rho_0\Big(\frac{g^2 H\pi}{2f^2} + \frac{gR^2\pi}{4}\Big) \ ,$$
   $$D = \rho_0\frac{2g^2\pi}{9f^2} \ ,$$

   are coefficients that contribute to the defined combined kinetic and potential energy based on the Gaussian eddy in geostrophic balance. The superscript $\cdot^n$ represents a timestep. Initial barotropic energy $E^{n=1}$ is then found using the initial eddy amplitude $A^{n=1}$.

2. **Find** E^{n+1} **using a discrete timestep solver**.

   To find barotropic energy at the next timestep (n+1), the following equation is solved using a discrete timestep solver

   $$\frac{\partial}{\partial t}(KE + PE) = P \ . \tag{2.1.22}$$

   Two timestep methods are used to solve (2.1.22): the fourth order Runge-Kutta (RK); and the third-order Adams-Bashforth (AB). The first initial timesteps ($n = 2, 3$) use RK since it only requires one previous timestep, whilst also maintaining a high degree of accuracy. The RK method is,

$$\begin{aligned}
k_1 &= \Delta t P^n,\\
k_2 &= \Delta t(P^n + k_1/2),\\
k_3 &= \Delta t(P^n + k_2/2),\\
k_4 &= \Delta t(P^n + k_3),\\
E^{n+1} &= E^n + \frac{k_1}{6} + \frac{k_2}{3} + \frac{k_3}{3} + \frac{k_4}{6}\ .
\end{aligned}$$

Once all information has been gathered at timesteps $n = 2$ and $n = 3$, AB is used to step forward in time ($n = 4, \cdots$), maintaining third-order accuracy and consistency with the MITgcm, then

$$E^{n+3} = E^{n+2} + \frac{\Delta t}{12\rho_0}\Big(23P^{n+2} - 16P^{n+1} + 5P^n\Big)\ .$$

3. **Find the amplitude, A^{n+1} from E^{n+1} using a root finder algorithm**. The predicted eddy amplitude A^{n+1} is found from E^{n+1} by applying the Newton-Raphson root finder method to Eq. (2.1.20). This amplitude is then used to find the wind power input P^{n+1}.

4. **Repeat steps 2 and 3 for the desired number of timesteps**.

5. **Find separate kinetic and potential energy**.

   Once A has been found for all timesteps, kinetic and potential energy are calculated to complete the method.

2.1.4 A barotropic decay timescale

A decay time scale for eddy energy due to wind damping can be found by

$$T_{bt} = E/P\ , \tag{2.1.24a}$$

$$T_{bt} = \frac{2\rho_0}{\rho_a\Big(2a_1 + 3a_2\,|u_a| + 4a_3\,|u_a|^2\Big)}\left[\frac{R^2 f^2}{4g} + \frac{H}{2} + \frac{2A}{9}\right]. \tag{2.1.24b}$$

The term involving A comes from the fact that the surface displacement η was included in the barotropic kinetic energy per unit volume. Inserting typical parameters into (2.1.24b), such as $A = 15$ cm, $R = 100$ km, $f = 10^{-4}$ s^{-1}, $H = 4000$ m, $\rho_0 = 1026$ kg m^{-3} and $\rho_a = 1.2$ kg m^{-3}, we can inspect the order of magnitude of each term in the square brackets of (2.1.24b). These parameters tell us that the second term involving ocean depth is dominant by at least four orders of magnitude. The first and third terms are small in comparison and can be neglected. This tells us that the decay timescale varies primarily with ocean depth and wind speed. So

$$T_{bt} \approx \frac{\rho_0 H}{\rho_a \Big(2a_1 + 3a_2 \left|u_a\right| + 4a_3 \left|u_a\right|^2 \Big)} , \tag{2.1.25}$$

which is comparable to the eddy attenuation timescale found by Gaube et al. (2015) via a barotropic vorticity balance approach. Using a fixed ocean depth of 4000 m, the eddy's lifetime is shown in Fig. 2.1.6 to have an almost exponential-like variability with wind speed. The timescale predicts eddy lifetimes to range from $\sim$ 2000 days for a 6 ms^{-1} wind to $\sim$ 100 days for a 30 ms^{-1} wind. The values of these predicted timescales are consistent with past estimates (Chelton et al., 2011; Gaube et al., 2015; Xu et al., 2016). Gaube et al. (2015) showed eddy lifetimes were shortened with a shallower ocean depth. This timescale (2.1.25) will be compared with the prediction and results from MITgcm.

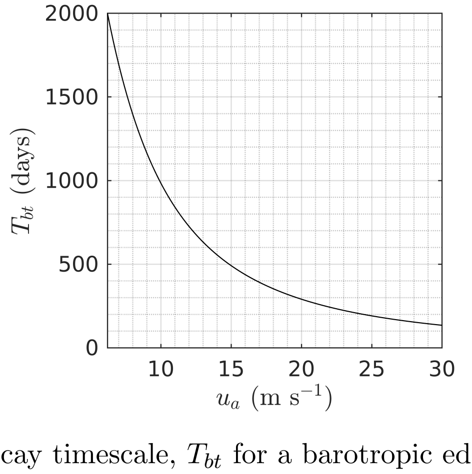

Figure 2.1.6: Eddy decay timescale, T_{bt} for a barotropic eddy using Eq. (2.1.25) as a function of wind velocity u_a with a fixed ocean depth of $H = 4000$ m.

2.2 Experimental design

Numerical simulations are carried out using the hydrostatic MIT general circulation model (Marshall et al., 1997b,a). The primary intention of this numerical model is to verify if we can predict the damping of total eddy energy using the analytical expression (2.1.10b).

The model is set up on an f-plane with experiments that span five northern latitudes, 20°N - 60°N in 10° increments. The model domain spans 1000 km in each x, y direction and uses doubly re-entrant boundary conditions i.e. anything that leaves through the northern boundary enters through the southern boundary. Grid spacing in the horizontal is $\Delta x, \Delta y = 2.5$ km, and allows eddies with the smallest length scale to be fully resolved (i.e. 50 km). The horizontal domain size is designed to accommodate a variety of eddy radii, eddy propagation, and initial gravity wave dispersion. The ocean depth is 4000 m deep with one vertical z-layer and has a flat bottom. This depth is typical of the mid ocean. There is a free-slip bottom boundary condition, used to avoid adding any additional friction or damping to the eddy. This model domain is computationally inexpensive meaning a wide array of parameter experiments can be performed. Key experimental parameters are summarised in Table 2.1.

Initial conditions for each eddy are derived from geostrophically balanced velocities using (2.1.2) with a Gaussian function (2.1.3). Experiments vary eddy amplitude from weak to strong ($A = 5$, 15, 25 cm) and radii from small to large ($R = 50$, 100, 150 km). The surface wind forcing in (2.1.4b) uses a west-east background wind speed of 7 m s^{-1} and provides the models only explicit form of dissipation (though some numerical dissipation is expected). This means damping of total eddy energy by surface winds can be accurately quantified. The choice of wind has been made arbitrarily and is done to fulfil the idealised nature of this experiment. The choice is made because similar idealised studies have implemented a $\sim$ 7 m s^{-1} wind speed (Dewar and Flierl, 1987; McGillicuddy, 2015; Chen et al., 2020). If the experiment made use of regional

Parameter	Symbol	Value	Units
Eddy amplitude	A	5, 15, 25	cm
Eddy radii	R	50, 100, 150	km
Horizontal grid spacing	$\Delta x, y$	2.5	km
Domain size	$L_{x,y}$	1000	km
Ocean depth	H	4000	m
Latitude	f	20, 30, 40, 50, 60 N	s^{-1}
Reference density	ρ_0	1026	kg m^{-3}
Atmospheric surface density	ρ_a	1.2	kg m^{-3}
Wind velocity	$\boldsymbol{u}_a$	7, 14, 21	m s^{-1}
Thermal expansion coeficient	α	2×10^{-4}	°C^{-1}
Timestep	Δt	100	s

Table 2.1: Experimental parameter values.

in-situ data (e.g. Brannigan et al. (2017)), then it might be more appropriate to choose a surface wind field taken from observations, e.g. data taken from a research vessel's meteorological tower.

Model simulations are a three-part process: two adjustment stages and the full model run. The model is initialised using geostropic velocity defined in Eq. (2.1.2) and Gaussian sea surface height from Eq. (2.1.3), and then run for 6 days allowing for any numerical adjustment to take place. The next part is a 400 day model run that uses absolute wind stress (2.1.4a). This wind forcing does not remove any energy, but the model run time is sufficient to allow any inertial waves generated by the wind to disperse. This second adjustment phase is extended to 800 and 1200 days when wind speeds are increased. The final process is the experimental simulations that take into account relative wind stress damping. These are integrated forward in time for 200 days ($\sim$ 6 months), which is thought to be adequate to compare with the prediction method. Using typical wind speeds of 7 m s^{-1}, 90 simulations are conducted. A further 4 are carried out for increased wind speeds of 14 and 21 m s^{-1}, as these have been consistently observed over the ocean (Ebuchi et al., 2002). All of these simulations are carried out for anticyclonic and cyclonic cases.

2.2.1 Diagnosing MITgcm energetics

Eddy energy in the MITgcm is calculated using the definitions from section 2.1.2, which are repeated here

$$KE = \rho_0 h \frac{1}{2} \boldsymbol{u} \cdot \boldsymbol{u} \ , \tag{2.2.1a}$$

$$PE = \rho_0 \frac{1}{2} g \eta^2 \ . \tag{2.2.1b}$$

Both $\boldsymbol{u}$ and η are daily time-mean quantities from MITgcm. Horizontal velocities $\boldsymbol{u}$ are total velocity i.e. geostrophic and ageostrophic parts, taken from the MITgcm diagnostic output. For the wind power input, we make use of the wind stress MITgcm diagnostic and multiply each component with their respective geostrophic velocity component calculated from η, rather than total velocity. Multiplying wind stress by the geostrophic velocity component removes some of the oscillations that appear in the wind power input due to ageostrophic effects, enabling a better comparison to be made with the prediction (see Fig. 2.3.1).

2.3 Results and discussion

We now present the results of the eddy energy prediction method (Pred) alongside the high resolution numerical simulations (MIT) for anticyclones (ACE) and cyclones (CE).

2.3.1 Using theory to predict eddy energy

In this section, the focus is on ACE's and CE's at the midlatitudes (40° N) with absolute amplitudes of 15 cm and a radius of 100 km.

Results of the prediction method are shown in Fig. 2.3.1. As expected, eddy energy and eddy amplitude (Fig. 2.3.1a,b,d,e) decay for ACE and CE in response to relative wind stress damping (Fig. 2.3.1c,f). Predicted energy values (red line) are comparable with MITgcm values (black line), and suggest equivalent spin down timescales. The barotropic decay timescale T_{bt} in (2.1.25) implies an eddy spin down time of around 2000 days. The similar decay rate between Pred and MIT is a result of their wind power inputs being close in value. This verifies that the analytical expression provides an equivalent level of damping as the numerical model.

In addition, differences between Pred and MIT are present. In terms of energy, this is thought to be a symptom of using the post-adjusted eddy amplitude from MITgcm as the initial amplitude in the prediction (Fig. 2.3.1a,d). Figure 2.3.1b,e initially shows the ACE to have $A \sim 14.7$ and CE to have $A \sim -15.25$. This is consistent with Pred ACE having less initial energy than Pred CE. The disparity between energy values in Pred and MIT could be due to equation imbalances between each eddy polarity.

The predicted method assumes a geostrophically balanced eddy, which is well documented to be the case in the literature (Chelton et al., 2011). Other studies have used a gradient wind balance (Lee and Niiler, 1998; Nardelli, 2013). Our results do point towards a departure from geostrophy, with a readjustment to gradient-wind balance (GWB). GWB is a balance of terms between the centrifugal (CG), Coriolis (CF), and pressure gradient (PGF) terms in the equations of motion,

$$-\frac{u_\theta^2}{r} - f u_\theta = -\frac{1}{\rho_0}\frac{\partial p}{\partial r} \; , \tag{2.3.1}$$

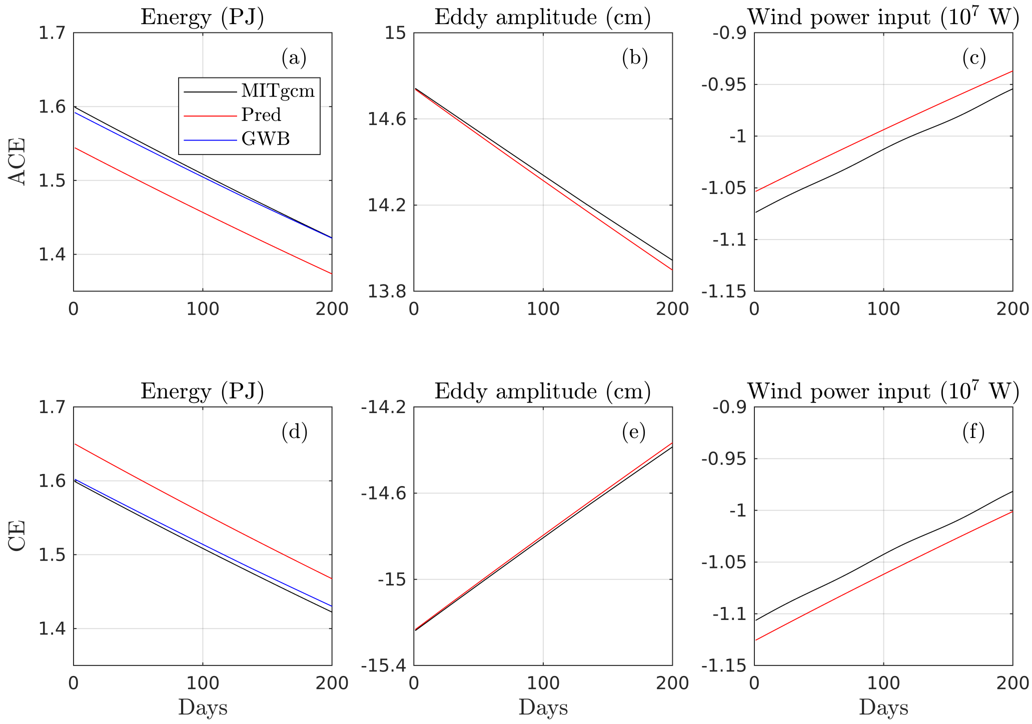

Figure 2.3.1: Time-series of eddy energy (left), eddy amplitude (middle), and wind power input (right) for an anticyclonic (top) and cyclonic (bottom) eddy. Black line is MITgcm and red line is predicted. Blue line uses a gradient wind balance to calculate eddy energy. Parameters: $R = 100$ km, $f = 40$ °N, $A = |15|$ cm, and $U = 7$ m s^{-1}. Energy is in units of PJ, amplitude is in cm, and wind power input in W.

which is written in polar coordinates. Here, u_θ is the azimuthal velocity, and $r = \sqrt{x^2 + y^2}$ is the radial distance. The first term in Eq. (2.3.1) is CG, the second is CF, and the last is PGF. Energy in both ACE and CE MIT simulations are equivalent even though eddy surface displacements are different. The reason for this is a consequence of an additional term in the momentum balance, the centrifugal term. In CE, CG and CF balance with PGF, and in ACE, CG and PGF balance with CF. The blue lines in Fig. 2.3.1a,d show eddy energy calculated from a gradient wind balance, assuming a Gaussian sea surface height structure that uses the eddy amplitude output from MITgcm experiments. GWB energy is seen to fit alongside MIT nicely. To confirm this properly would require finding a new analytical solution using a GWB approach, which is not pursued here.

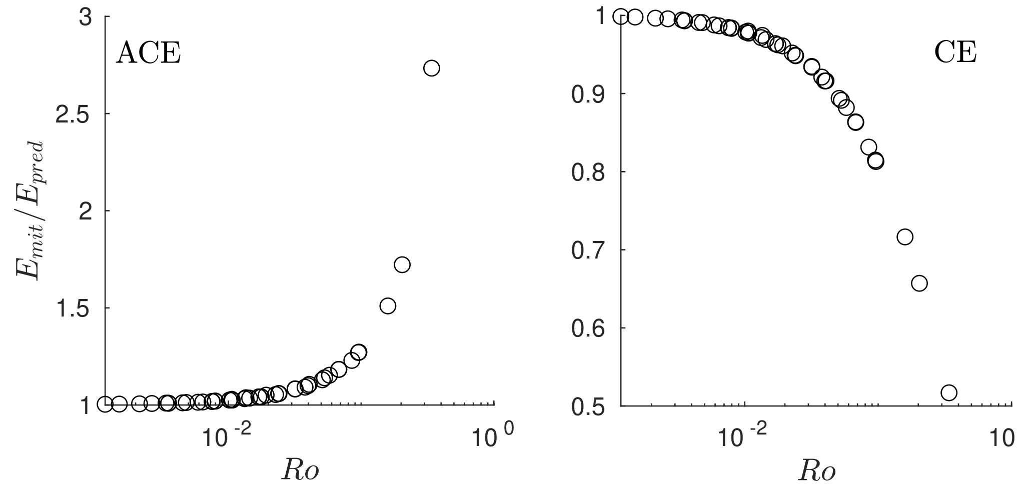

Figure 2.3.2: Ratio E_{mit}/E_{pred} at day 1 of simulation plotted against Ro for ACE (left) and CE (right).

2.3.2 Why might we expect the theory to break down?

We have verified the prediction method for a moderate-in-strength mid-latitude eddy. The analysis is now extended to cover more eddy parameter values to establish where the prediction method outlined in section 2.1 may not be suitable e.g. due to departures from geostrophic balance. We calculate a ratio of MIT energy to Pred energy, E_{mit}/E_{pred}, and plot this against the Rossby number, $Ro = U/fR$ (Fig. 2.3.2). The U in the case of Ro is the maximum velocity. The energy ratio is plotted at day 1 to illustrate how the parameter choices could influence the prediction. Numerous simulations (see Sec. 2.2) have been run at different latitudes for different amplitude eddies, and put in terms of Ro.

Having a ratio $E_{mit}/E_{pred} \approx 1$ is means predicted energy is close to energy in the numerical simulation, as seen in Fig. 2.3.1. When this occurs, Fig. 2.3.2 shows that $Ro \ll 1$, implying that advective processes are negligible and the eddy is in a geostrophic balanced state. When E_{mit}/E_{pred} deviates from unity in each eddy Ro increases, suggesting that the prediction method is not suitable when advection of momentum is non-negligible. This could reinforce the idea that a gradient wind balance would be more appropriate for this prediction approach when Ro is large. However, Fig. 2.3.2 shows that eddies with small Ro are well suited to this prediction method. Moreover, Chelton et al. (2011) measured the number of observed eddies and recorded their Rossby number, finding very few to actually have $Ro > 0.1$. In fact, the right panel of Fig. 12 in Chelton et al. (2011) shows eddy length scales are large near the equator and get smaller with increasing latitude. The cases with a large Rossby number explored in this analysis are few and far between in the global ocean, suggesting that this prediction method is in fact robust for observed eddies.

2.3.3 Increased wind forcing

In this section, the prediction method and analytical wind power input is examined for increased wind speed. It was shown in section 2.1.1, Fig. 2.1.4 that increased wind speeds will generate higher levels of wind damping. Fig. 2.3.3 shows that increasing wind speeds does lead to higher levels of damping in total eddy energy and amplitude for ACE and CE. This is the case in MIT and Pred, which are tracked nicely alongside each other for their respective wind speeds. Note that the eddy chosen here has a small Ro and so the prediction method, as expected, holds nicely. When wind speeds increase from 7 to 21 m s^{-1}, damping of total eddy energy is enhanced from around 11% to 50% in both eddies for MIT and Pred. These percentages of damping equate to spin down times of around 2000 days for 7 m s^{-1} and 400 days for 21 m s^{-1}, which are both similar to timescales suggested by the barotropic timescale in section 2.1.4, Fig. 2.1.6.

Looking at eddy amplitudes, the rate of decay is slightly more than half the decay seen in energy. That is, an increase in wind speed from 7 to 21 m s^{-1} causes a reduction in amplitude from around 5% up to 30%, for both ACE and CE in MIT and Pred. This is because energy and amplitude are related through the cubic polynomial (2.1.20). If the cubic term is neglected, then there exists a square root function like $A = \sqrt{E/C^2}$, plotted in Fig. 2.3.4, showing how both terms

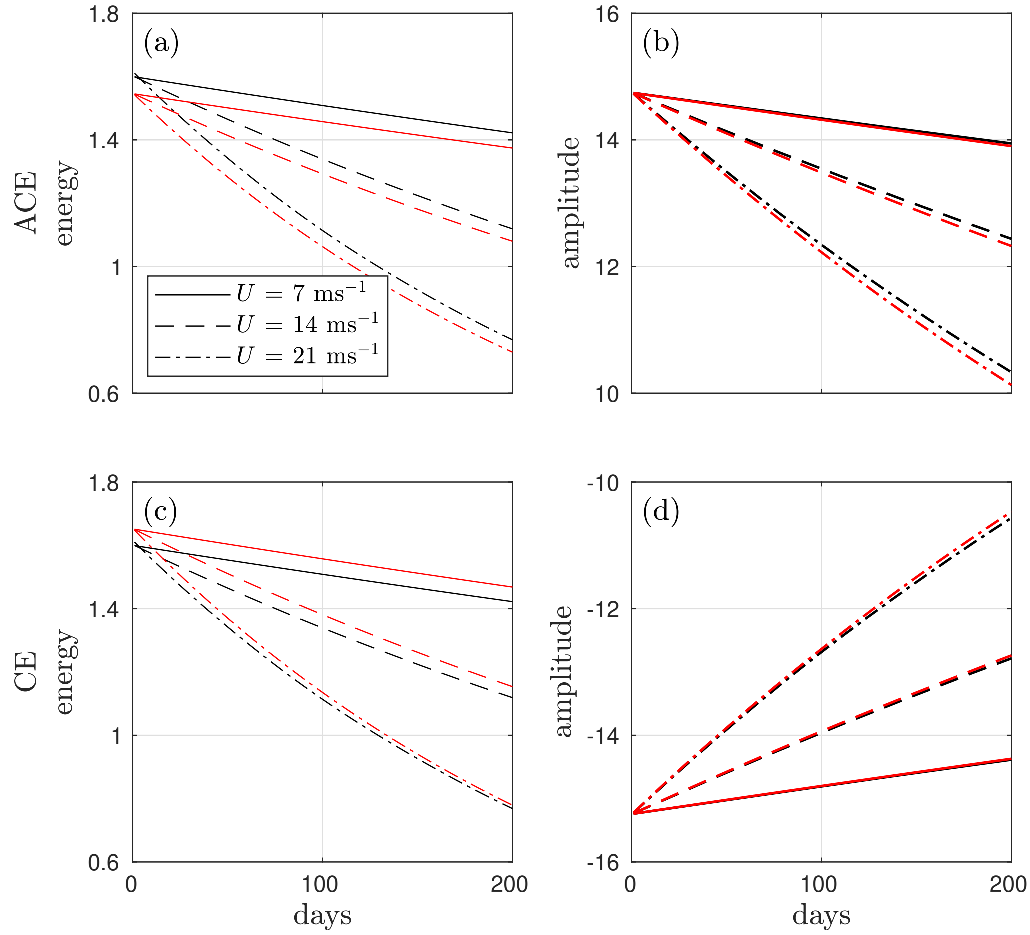

Figure 2.3.3: Damping of total eddy energy and amplitude for three wind speeds 7, 14, 21 m s^{-1}. In a) ACE energy, b) ACE amplitude, c) CE energy, and d) CE amplitude, MITgcm shown by black lines, predicted shown by red lines. Eddy parameters are $A = 15$ cm and $R = 100$ km.

are related to each other. The E/C^2 term decays around twice the rate of the amplitude A.

2.3.4 Horizontal maps of wind work, kinetic energy, and relative vorticity

It was shown in section 2.3.1 that eddy energy decays under relative wind stress forcing. Here, horizontal profiles of wind work, kinetic energy, and normalised relative vorticity are displayed for MIT to illustrate the damping effect on each of the anticyclone and cyclone. Eddy parameters use $A = 15$ cm, $R = 100$ km

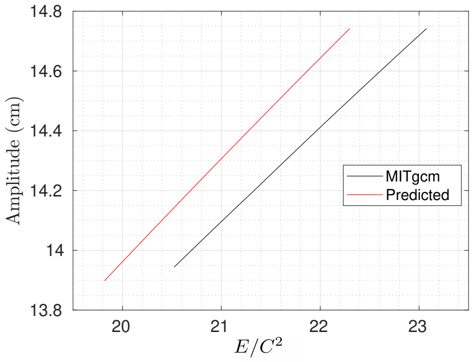

Figure 2.3.4: Eddy amplitude plotted against E/C^2 for the ACE in section 2.3.1.

at latitude 40° N with $\boldsymbol{u}_a = 7$ m s^{-1}. Again, all quantities are daily time-mean MITgcm diagnostics, except $\boldsymbol{u}$ in wind work, which is the geostrophic component.

Wind work

Wind work patterns and a meridional cross section are shown at day 1 and day 200 for the ACE (Fig. 2.3.5) and CE (Fig. 2.3.6). In each profile there exist dipoles of positive and negative wind work in the north-south regions of the eddy, much like Fig. 2.1.3 in section 2.1.1. Because we are only looking at relative wind stress, negative values dominate over positive, highlighting how relative wind stress works on the eddy surface. With more negative work than positive, the total wind work amounts to a decay of energy, as seen in Fig. 2.3.1c,f. Between each eddy polarity, the dipoles have been flipped on their north-south axis. This is because the direction of rotation is opposite in each eddy case. Over the course of the simulation, shading in contour values of wind work in each eddy has become smaller, implying a reduction in wind damping is taking place as the eddy weakens. This reduction is also seen through the cross sections in the right panels of Figs. 2.3.5 and 2.3.6. Recall the amplitude A in each eddy decays (Fig. 2.3.1), and it was shown that total wind power input depends on this parameter (see Eq. 2.1.10b). A reduction in eddy amplitude is consistent with a contraction of the central contours in Figs. 2.3.5 and 2.3.6.

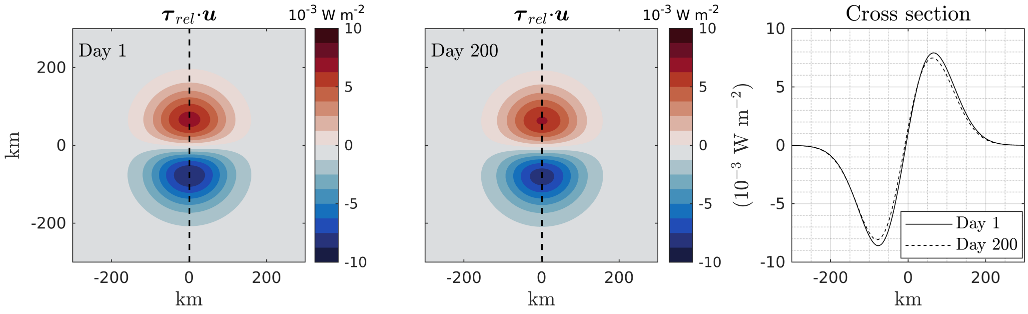

Figure 2.3.5: Wind work $\boldsymbol{\tau}_{rel} \cdot \boldsymbol{u}$ using $\boldsymbol{u}_a = 7$ m s^{-1} on the anticyclonic eddy with amplitude 15 cm, radius 100 km, and latitude 40°. Left panel is day 1, middle panel is day 200, and right panel is a meridional cross section through $x = 0$ at day 1 and day 200. Units of wind work in 10^{-3} W m^{-2}.

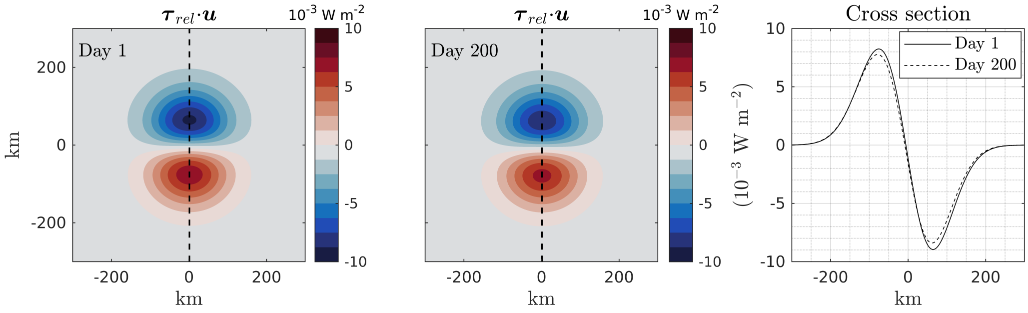

Figure 2.3.6: Wind work $\boldsymbol{\tau}_{rel} \cdot \boldsymbol{u}$ using $\boldsymbol{u}_a = 7$ m s^{-1} on the cyclonic eddy with amplitude 15 cm, radius 100 km, and latitude 40°. Left panel is day 1, middle panel is day 200, and right panel is a meridional cross section through $x = 0$ at day 1 and day 200. Units of wind work in 10^{-3} W m^{-2}.

Kinetic energy and relative vorticity

Kinetic energy and normalised relative vorticity are now shown at day 1 and day 200 for the ACE (Fig. 2.3.7) and CE (Fig. 2.3.8). Beginning with the ACE, kinetic energy at day 1 displays a circular symmetric pattern with the highest levels found at the eddy speed based radius, $L_s \approx 75$ km. By day 200, kinetic energy has decreased as a result of relative wind stress damping (Fig. 2.3.5). In the CE, kinetic energy similarly decreases.

Normalised relative vorticity (ζ/f) is the dynamical Rossby number and can be used to illustrate the ageostrophy of the eddy. In each eddy, ζ/f exhibits a monopole profile of vorticity, where a band of oppositely signed relative vorticity encircles the primary relative vorticity of the eddy. From day 1 to 200, ζ/f at each eddy centre is damped, implying a reduction in strength of the eddy flow.

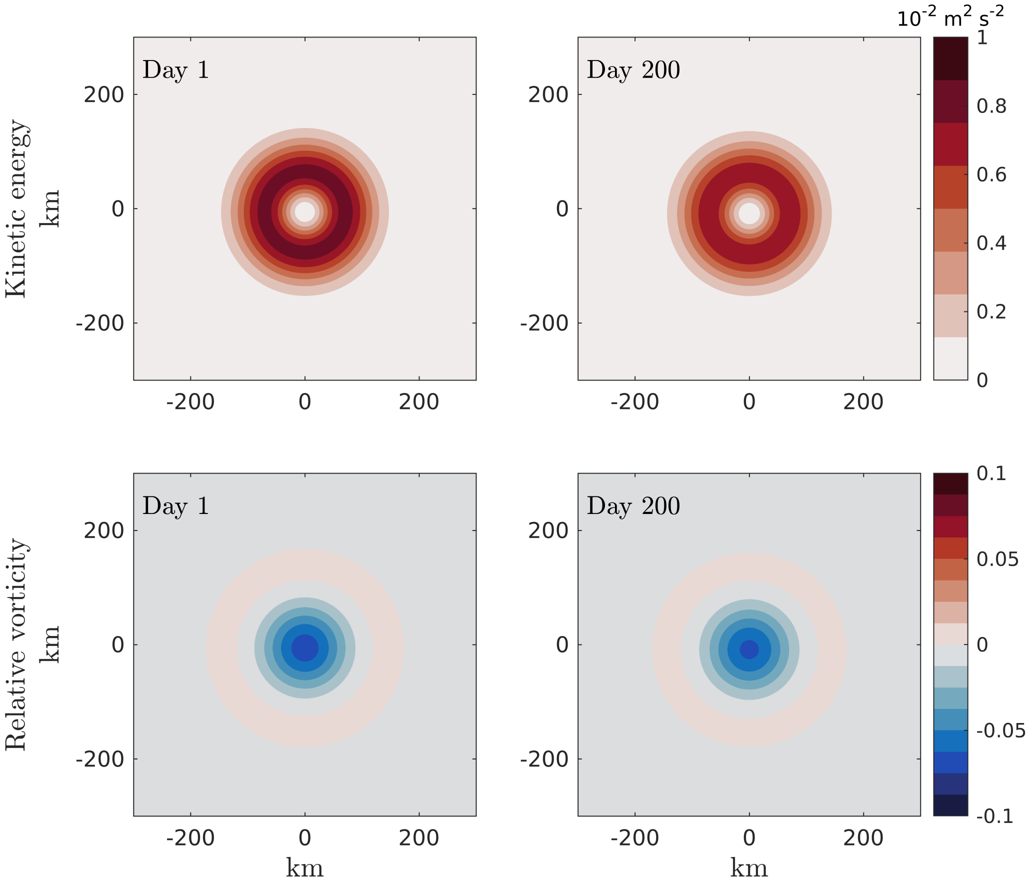

Figure 2.3.7: Kinetic energy ($\frac{1}{2}\boldsymbol{u}\cdot\boldsymbol{u}$) in top panels and normalised relative vorticity (ζ/f) in bottom panels for an anticyclonic eddy with amplitude 15 cm, radius 100 km, and latitude 40°. Day 1 in left panels and day 200 in right panels. Kinetic energy in units of m^2 s^{-2}.

However, despite the damping process, each eddy preserves its circular shape, suggesting the wind has no impact on its symmetry over the simulation period.

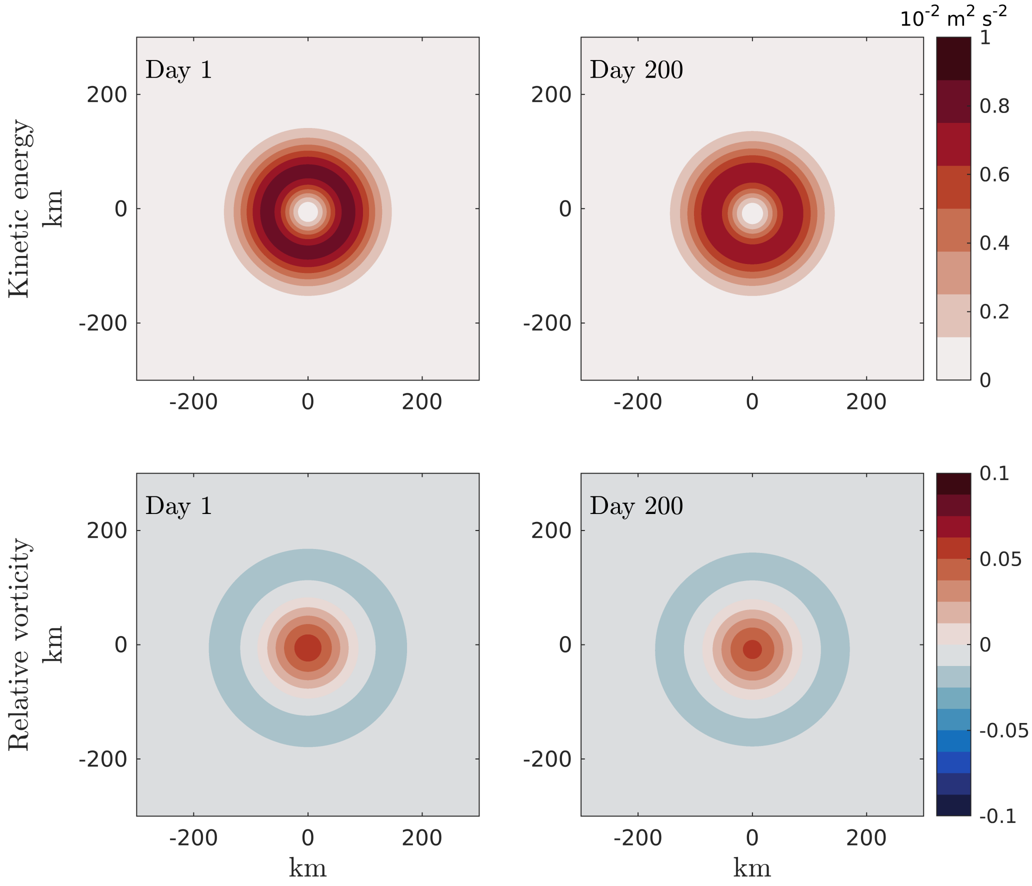

Figure 2.3.8: Kinetic energy ($\frac{1}{2}\boldsymbol{u}\cdot\boldsymbol{u}$) in top panels and normalised relative vorticity (ζ/f) in bottom panels for a cyclonic eddy with amplitude 15 cm, radius 100 km, and latitude 40°. Day 1 in left panels and day 200 in right panels. Kinetic energy in units of m^2 s^{-2}.

2.4 Concluding chapter remarks

In this chapter we developed a theoretical framework for the prediction of barotropic eddy energy evolution due to relative wind stress damping. To begin with, an analytical expression for wind power input due to relative wind stress was derived from simple analytical equations that described the eddy structure. The wind field used in this expression was zonally uniform. The mesoscale eddy was assumed to be in geostrophic balance and display a Gaussian sea surface height. Then, a barotropic energy equation was presented with energy change dependent on the analytical wind power input. The prediction method was then described in detail, requiring only a few key parameters, such as eddy amplitude and ocean depth. From this theory, a barotropic decay timescale was also found, showing similarities with past formulations (Gaube et al., 2015).

Making use of a high resolution numerical model, MITgcm, we were able to verify whether the analytical wind power input could be used to predict the damping of total eddy energy. For a midlatitude anticyclonic or cyclonic eddy, the prediction of energy was in close agreement to that in MITgcm simulations, with all other quantities decaying at similar rates. Calculating total energy based on a gradient wind balance approach achieved values even closer to those seen in MITgcm. This suggests a gradient wind balance may be more suitable than geostrophic balance for use in the prediction method, depending on eddy parameters. We then tested the prediction method by varying eddy amplitude, eddy radius, and latitude. The prediction method is shown to be less suitable when the eddy has a Rossby number greater than 0.1. For eddies with $Ro > 0.1$, a gradient wind balance approach should be considered. In terms of increased wind speed, the prediction method holds up nicely. As wind speeds increase, the rate of decay also increases, which is similarly matched by MITgcm simulations. Finally, horizontal maps of wind work, kinetic energy, and relative vorticity from MITgcm simulations were shown to exhibit a decay in their values, consistent with relative wind stress damping.

The overall message to take from this work is that the rate of damping by relative wind stress is well approximated by the analytical wind power input. This work opens the door for future implementation in eddy energy parameterisations (Marshall et al., 2012; Mak et al., 2018), as well as extending the theory to represent baroclinic mesoscale eddies (see chapter 3).

The analytical wind power input is derived on the basis of a uniform zonal background wind, which acts to dampen the eddy with relative wind stress. However, a wind field may vary in space. For example, the wind speed may vary linearly in the meridional direction e.g. $u_a = \beta y + u_0$, where u_0 is the constant wind field, and β adds in a meridional wind gradient. The effects of such a wind field over a mesoscale eddy were discussed in the supporting documents of Xu et al. (2016). They descibed how this wind profile could dampen or energise the eddy depending on the eddy rotation (illustrated in Xu et al. (2016) Fig. S3 and S4). This idea was considered and even attempted briefly. However, we encountered modelling issues through the variation in Ekman transport over the domain and across the doubly periodic boundaries i.e. discontinuities in sea surface height at the northern and southern boundaries. Nevertheless, this is certainly an interesting idea to pursue within this modelling framework with suitable changes to the model domain.

In MITgcm, it is interesting that the eddies remain stable over $\sim$ 600 days of model integration. This implies that the eddy parameters we have employed here are not unstable, or rather the unstable modes have very small growth rates. It was shown by Carton et al. (1989) that there exists a critical steepness parameter $\alpha_c = 1.8 - 1.9$ where unstable modes will begin to grow in a barotropic eddy, and the eddy's shape will deviate from its monopolar structure (see section 1.2.5 in chapter 1). The Gaussian shape we employ here has steepness parameter $\alpha = 2$, which is on the threshold of being stable, and thus may explain why the eddy does not destabilise. To verify this we would have to run simulations using steepness parameters beyond $\alpha = 2$.

In the next chapter, we will build on this theoretical framework to encompass a more realistic ocean eddy setup.

3

Predicting The Damping of Baroclinic Geostrophic Eddy Energy

In this thesis so far, we have developed a theoretical framework to predict the damping of barotropic total eddy energy due to relative wind stress. This enabled us to verify the use of the analytical wind power input for the dissipation of mesoscale eddy energy. However, although sea surface height data can be used to infer barotropic kinetic energy in some regions (Baker-Yeboah et al., 2009), it is known to primarily reflect the main thermocline and baroclinic eddy structure (Wunsch, 1997). In this chapter, we extend the barotropic framework to account for a baroclinic mesoscale eddy. The question we want to answer here is, can the damping of baroclinic total eddy energy be predicted using the analytical wind power input derived in chapter 2?

This chapter begins by introducing the two-layer shallow water equations that contain a first baroclinic mode structure. An analytical energy equation is then derived from this, whilst also making use of theory first outlined in chapter 2. The barotropic prediction method described in chapter 2 is thus extended for the baroclinic eddy. This prediction method is compared with eddies in a continuously stratified high resolution general circulation model. This will enable us to verify whether this method has validity in the realms of mesoscale eddy prediction or parameterisations. The eddy spatial patterns diagnosed from the numerical model are also examined. We end the chapter with a summary of our conclusions, and discuss limitations and future work.

3.1 Theory

3.1.1 Baroclinic energy equation

To start, a baroclinic eddy is described using the two-layer shallow water equations

$$\frac{D\boldsymbol{u}_1}{Dt} + f\boldsymbol{k} \times \boldsymbol{u}_1 = -g\nabla_h \eta_1 + \frac{\boldsymbol{\tau}}{\rho_0 h_1} + A_4 \nabla_h^4 \boldsymbol{u}_1 \ , \tag{3.1.1a}$$

$$\frac{D\boldsymbol{u}_2}{Dt} + f\boldsymbol{k} \times \boldsymbol{u}_2 = -g\nabla_h \eta_1 - g'\nabla_h \eta_2 + A_4 \nabla_h^4 \boldsymbol{u}_2 \ , \tag{3.1.1b}$$

$$\frac{\partial h_1}{\partial t} + \nabla_h \cdot (h_1 \boldsymbol{u}_1) = 0 \ , \tag{3.1.1c}$$

$$\frac{\partial h_2}{\partial t} + \nabla_h \cdot (h_2 \boldsymbol{u}_2) = 0 \ , \tag{3.1.1d}$$

where subscript $\cdot_1$ is the upper layer and $\cdot_2$ is the lower layer. In Eq. (3.1.1), $\boldsymbol{u}_i = (u_i, v_i)$ are horizontal geostrophic velocity components in the zonal and meridional direction, f is the Coriolis frequency, g is the gravitational acceleration, ρ_0 is a reference ocean density, η_1 is the surface displacement, η_2 is the interface displacement between the two layers, $g\prime = g(\rho_2 - \rho_1)/\rho_2$ is the reduced gravity - change in acceleration of gravity due to buoyant forces - found using upper and lower layer density, $h_1 = H_1 + \eta_1 - \eta_2$ and $h_2 = H_2 + \eta_2$ are the respective layer depths of which $H_{1,2}$ is the reference layer depth, $\boldsymbol{\tau}$ is a wind stress, and A_4 is a constant viscous coefficient that depends on the grid scale and timestep. The subscript $\cdot_g$ has been left off the velocity vectors for readability. This shallow water model includes the effects of stratification through $g\prime$, which accounts for the adjustment between the two layers due to gradients in density. Equations (3.1.1a) and (3.1.1b) are momentum equations and Eqs. (3.1.1c) and (3.1.1d) are continuity equations. The second term on the right hand side of Eq. (3.1.1a) is the wind forcing. The third term on the right hand side of Eqs. (3.1.1a) and (3.1.1b) represents biharmonic viscosity and is

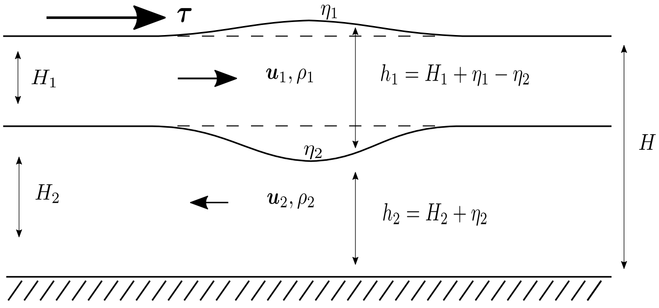

Figure 3.1.1: Schematic depicting the two-layer model described in Eq. (3.1.1).

included for completeness as it is present in the MITgcm model.

The choice of this two-layer shallow water model in representing a baroclinic eddy is drawn from past studies. Overall, eddy variability is well captured by sea surface height. Wunsch (1997) found sea surface height to be a good representation of the first baroclinic mode (BC1), and to therefore also reflect the motion of the main thermocline, or vertical eddy structure. Additionally, Wunsch also showed the sea surface height to contain the majority of ocean's surface kinetic energy. Furthermore, Stammer (1997) found eddy length scales to be proportional to the scale of the first baroclinic mode. What is more, studies have since been carried out that explore features of mesoscale eddies through sea surface altimeter data (Chaigneau et al., 2008; Chelton et al., 2011; Chen et al., 2019). By considering eddies that exhibit vertical structures described by their surface profile, we can attempt to infer the decay of mesoscale eddy energy using this two-layer model.

For a baroclinic eddy, variations of the interface displacement are proportional to the surface displacement by $\eta_2(x, y, t) = \eta_1(x, y, t)/\mu$ (Gill, 1982) and following Cushman-Roisin and Beckers (2006), proportionality can be found between layer velocities using $\boldsymbol{u}_2 = \lambda \boldsymbol{u}_1$. The proportionality coefficients μ and λ provide the dynamical structure of the eddy through normal modes. Normal modes exhibit wave patterns that depend on these coefficients. For the two-layer model there exist two pairs of solutions for μ and λ, a barotropic mode (BT) and first baroclinic mode (BC1). Definitions of these coefficients can be found by equating

(3.1.1b) with (3.1.1a) and neglecting dissipation terms to give

$$\lambda = \frac{g\mu + g'}{g\mu} \; . \tag{3.1.2}$$

Also, the continuity equation (3.1.1d) is equated with (3.1.1c) giving

$$\frac{1}{\mu - 1} = \frac{H_2 \lambda}{H_1} \; . \tag{3.1.3}$$

Then Eqs. (3.1.2) and (3.1.3) are then used to form an equation for λ

$$H_2 \lambda^2 + (H_1 - H_2)\lambda - H_1 = 0 \; . \tag{3.1.4}$$

Eq. (3.1.4) has two solutions for λ that relate to either BT or BC1. BT is given by $\lambda = 1$ and $\mu = H/H_2$ since there is no change in density between the two layers, i.e. depth independent flow. Here, $H = H_1 + H_2$ is the depth of the ocean. BC1 has $\lambda = -H_1/H_2$ and $\mu = -g'H_2/gH$. The value of μ for BC1 will be used in our two-layer model to incorporate the interface displacement of the baroclinic eddy. For an anticyclonic (cyclonic) eddy, BC1 has a peak (trough) in sea surface height and a trough (peak) in its thermocline displacement. The eddy will also exhibit depth-dependent flow. On the other hand, the barotropic mode has only a sea surface height displacement and exhibits depth-independent flow, which was studied in chapter 2.

Two-layer energy equations are now derived using the same method as for the barotropic eddy in chapter 2. Kinetic and potential energy equations for the first layer are found by multiplying (3.1.1a) by $h_1 \boldsymbol{u}_1$ and (3.1.1c) by $g\eta_1$ and also substituting in $h_1 = H_1 + \eta_1 - \eta_2$, which gives

$$\begin{gathered} \frac{\partial}{\partial t}\Big(h_1 \frac{1}{2} \boldsymbol{u}_1 \cdot \boldsymbol{u}_1\Big) + \nabla_h \cdot \Big((\frac{1}{2}\boldsymbol{u}_1 \cdot \boldsymbol{u}_1 + g\eta_1) h_1 \boldsymbol{u}_1\Big) - g\eta_1 \nabla_h \cdot (h_1 \boldsymbol{u}_1) = \\ \frac{\boldsymbol{\tau} \cdot \boldsymbol{u}_1}{\rho_0} + h_1 \boldsymbol{u}_1 A_4 \nabla_h^4 \boldsymbol{u}_1 \; , \end{gathered} \tag{3.1.5a}$$

$$\frac{\partial}{\partial t}\Big(\frac{1}{2} g\eta_1^2\Big) - g\eta_1 \frac{\partial \eta_2}{\partial t} + g\eta_1 \nabla_h \cdot (h_1 \boldsymbol{u}_1) = 0 \; . \tag{3.1.5b}$$

The second layer kinetic and potential energy equations are found by multiplying (3.1.1b) by $h_2\boldsymbol{u}_2$ and (3.1.1d) by $g\prime\eta_2$ and also substituting in $h_2 = H_2 + \eta_2$, which gives

$$\begin{aligned} &\frac{\partial}{\partial t}\Big(h_2\frac{1}{2}\boldsymbol{u}_2\cdot\boldsymbol{u}_2\Big)+\nabla_h\cdot\Big((\frac{1}{2}\boldsymbol{u}_2\cdot\boldsymbol{u}_2+g\eta_1+g\prime\eta_2)h_2\boldsymbol{u}_2\Big)- \\ &\qquad g\eta_1\nabla_h\cdot(h_2\boldsymbol{u}_2)-g\prime\eta_2\nabla_h\cdot(h_2\boldsymbol{u}_2)=h_2\boldsymbol{u}_2A_4\nabla_h^4\boldsymbol{u}_2\ , \end{aligned} \tag{3.1.6a}$$

$$\frac{\partial}{\partial t}\Big(\frac{1}{2}g\prime\eta_2^2\Big)+g\prime\eta_2\nabla_h\cdot(h_2\boldsymbol{u}_2)=0\ . \tag{3.1.6b}$$

Now, combining Eqs. (3.1.5a)-(3.1.6b) and making use of the fact that $\partial\eta_2/\partial t = \partial h_2/\partial t$ in Eq. (3.1.5b), the total energy equation is

$$\begin{aligned} &\frac{\partial}{\partial t}\Big(\rho_0\big(h_1\frac{1}{2}\boldsymbol{u}_1\cdot\boldsymbol{u}_1+h_2\frac{1}{2}\boldsymbol{u}_2\cdot\boldsymbol{u}_2+\frac{1}{2}g\eta_1^2+\frac{1}{2}g\prime\eta_2^2\big)\Big)+ \\ &\quad\nabla_h\cdot\Big(\rho_0(\frac{1}{2}\boldsymbol{u}_1\cdot\boldsymbol{u}_1+g\eta_1)h_1\boldsymbol{u}_1+\rho_0(\frac{1}{2}\boldsymbol{u}_2\cdot\boldsymbol{u}_2+g\eta_1+g\prime\eta_2)h_2\boldsymbol{u}_2\Big)= \\ &\qquad\qquad\boldsymbol{\tau}\cdot\boldsymbol{u}_1+\rho_0h_1\boldsymbol{u}_1A_4\nabla_h^4\boldsymbol{u}_1+\rho_0h_2\boldsymbol{u}_2A_4\nabla_h^4\boldsymbol{u}_2\ . \end{aligned} \tag{3.1.7}$$

In Eq. (3.1.7), terms in the top row in order from left to right are: upper layer kinetic energy, lower layer kinetic energy, upper layer potential energy, and lower layer potential energy. Terms in the middle are divergence of kinetic and potential energy. In the bottom row: work done by winds on the surface geostrophic motion, upper layer viscosity, and lower layer viscosity.

It is possible to go one step further by utilising analytical equations to find a simple expression for the two-layer baroclinic eddy energy equation. Hereon, we make some simplifications to Eq. (3.1.7). First, in a domain integrated energy equation, the divergence term will equal zero, and so it is neglected from this point. We also use the knowledge that the interface displacement and lower layer velocities can be calculated by their proportionality with upper layer values, i.e. $\eta_2 = \eta_1/\mu$ and $\boldsymbol{u}_2 = \lambda\boldsymbol{u}_1$. We also refamiliarise the reader with, $h_1 = H_1+\eta_1-\eta_2$, $h_2 = H_2+\eta_2$, and $H = H_1+H_2+\eta_1$. With this, Eq. (3.1.7) in domain integral form is

$$\begin{aligned}\frac{\partial}{\partial t}\int_S \Big[\rho_0\Big(\big(H_1+\eta_1-\frac{\eta_1}{\mu}+\lambda^2(H-H1+\frac{\eta_1}{\mu})\big)\frac{1}{2}\boldsymbol{u}_1\cdot\boldsymbol{u}_1+\big(g+\frac{g\prime}{\mu^2}\big)\frac{\eta_1^2}{2}\Big)\Big]\,dS \\ =\int_S \boldsymbol{\tau}\cdot\boldsymbol{u}_1\,dS \\ +\int_S \Big[\rho_0\big(H_1+\eta_1-\frac{\eta_1}{\mu}+\lambda^2(H-H1+\frac{\eta_1}{\mu})\big)\boldsymbol{u}_1 A_4\nabla_h^4\boldsymbol{u}_1\Big]\,dS\;. \end{aligned} \qquad (3.1.8)$$

In this equation, the only information we require at depth is the depth of the thermocline, H_1, and lower layer density, ρ_2. All other information can be inferred from surface and topographic data. The first term in the integral on the left-hand-side of Eq. (3.1.8) is total kinetic energy (KE), and the second term is total potential energy (PE). On the right-hand-side, the first term is total wind power input (P), and the second term is total biharmonic viscous dissipation (D_{visc}). Then, the total energy equation in shorthand is

$$\frac{\partial}{\partial t}(KE+PE)=P+D_{visc}\;. \qquad (3.1.9)$$

Now, analytical expressions for $KE+PE$ and D_{visc} need to be found to proceed with the prediction of baroclinic eddy energy. First, recall the eddy sea surface displacement is approximated by a Gaussian function (Chelton et al., 2011)

$$\eta = Ae^{-(x^2+y^2)/R^2}\;, \qquad (3.1.10)$$

where A is the eddy sea surface amplitude, and R is the eddy e-folding radius. Eddy horizontal velocities are also in geostrophic balance

$$u=-\frac{g}{f}\frac{\partial\eta}{\partial y}\;, \qquad (3.1.11a)$$

$$v=\frac{g}{f}\frac{\partial\eta}{\partial x}\;. \qquad (3.1.11b)$$

Total energy, wind power input, and viscous dissipation are found by spatially integrating their respective terms in Eq. (3.1.8) in the limits of $\pm\infty$ in the x, y

direction, and making use of Eqs. (3.1.10) and (3.1.11). Total energy is

$$\begin{aligned} KE + PE \equiv E = \rho_0 \pi \Big(&\big((H_1 - \lambda^2 H_1 + \lambda^2 H)\frac{g^2}{2f^2} + R^2 \frac{g}{4} + R^2 \frac{g\prime}{4\mu^2}\big) A^2 \\ &+ \big((1 - \frac{1}{\mu} + \frac{\lambda^2}{\mu})\frac{2g^2}{9f^2}\big) A^3 \Big) \ , \end{aligned} \tag{3.1.12}$$

which defines total baroclinic eddy energy, and is measured in units of kg m^2 s^{-2}. Terms including eddy radius, R, are potential energy, and all others contribute to kinetic energy. In chapter 2 we found an expression for wind power input due to relative wind stress of a uniform zonal background wind,

$$P_{rel} = \int_S \boldsymbol{\tau}_{rel} \cdot \boldsymbol{u}_1 \, dS \ , \tag{3.1.13a}$$

$$P_{rel} = -\rho_a \Big(2a_1 + 3a_2 \left| u_a \right| + 4a_3 \left| u_a \right|^2 \Big) \frac{g^2 A^2 \pi}{2f^2} \ , \tag{3.1.13b}$$

where ρ_a is air density, a_1, a_2, a_3 are constants taken from Large and Yeager (2004), and u_a is the 10 m wind velocity. The units of P_{rel} are measured in kg m^2 s^{-3}. It was shown in chapter 2 that an absolute wind stress does not remove energy from the eddy, so $P_{abs} = 0$. Subscripts $\cdot_{rel}$ and $\cdot_{abs}$ are relative and absolute, respectively. To find D_{visc}, the biharmonic viscous term is simplified using the identity

$$\boldsymbol{u} A_4 \nabla_h^4 \boldsymbol{u} = A_4 \Big(\nabla^4 (\frac{1}{2} \boldsymbol{u} \cdot \boldsymbol{u}) - \nabla^2 (\nabla \boldsymbol{u})^2 - (\nabla^2 \boldsymbol{u})^2 \Big) \ . \tag{3.1.14}$$

In (3.1.14), the first two terms on the right-hand side represent diffusion, and can be written as the divergence of a flux. The first term on the right hand side is diffusion of kinetic energy and the second is gradients of velocity. The third term contributes to the rate of change of energy through viscous dissipation. Integrating the last term in (3.1.8) using the identity in (3.1.14) along with no normal flow boundary conditions over the whole domain, the first two terms in

(3.1.14) vanish, whilst the third term gives D_{visc} as

$$\begin{aligned} D_{visc} = -A_4\rho_0\frac{g^2}{f^2}\Big(\pi(1-\lambda^2)\big(H_1\frac{24A^2}{R^4}+\frac{384A^3}{27\mu R^4}\big) \\ +\lambda^2 H\frac{24A^2}{R^4}-\frac{384A^3}{27R^4}\Big) \,, \end{aligned} \tag{3.1.15}$$

which is measured in units of kg m^2 s^{-3}. We now have all the expressions for an analytical two-layer energy equation with a first baroclinic mode structure.

3.1.2 Outline of prediction method

We now present the prediction method for the two-layer model.

1. **Find the initial energy of the eddy,** $E^{n=1}$.

   Initial eddy energy is found using Eq. (3.1.12)

   $$E^n = C(A^n)^2 + D(A^n)^3 \,, \tag{3.1.16}$$

   where

   $$C = \rho_0\pi\Big((H_1-\lambda^2H_1+\lambda^2H)\frac{g^2}{2f^2}+R^2\frac{g}{4}+R^2\frac{g\prime}{4\mu^2}\Big) \,, \tag{3.1.17a}$$

   $$D = \rho_0\pi\Big((1-\frac{1}{\mu}+\frac{\lambda^2}{\mu})\frac{g^2}{9f^2}\Big) \,, \tag{3.1.17b}$$

   are coefficients that contribute to the combined kinetic and potential energy based on the Gaussian eddy in geostrophic balance with a first baroclinic mode structure. The superscript $\cdot^n$ represents a timestep. The initial baroclinic energy $E^{n=1}$ is found by putting the initial eddy amplitude $A^{n=1}$ and eddy parameters into Eq. (3.1.16).

2. **Find** E^{n+1} **using a discrete timestep solver**.

   To find baroclinic energy at the next timestep $(n+1)$, Eq. (3.1.9)

   $$\frac{\partial E}{\partial t} = P + D_{visc} \tag{3.1.18}$$

needs to be solved using a discrete timestep solver. To begin the solver, the Runge-Kutta method is used for timesteps $n = 2, 3$ as only information from the previous timestep is required to achieve a high order of accuracy. Then for timesteps $n = 4, 5, \cdots$ the Adams-Bashforth third order multistep method is used to maintain consistency with the MITgcm timestepping. (see chapter 2 for time-stepping method details)

3. **Find the amplitude, A^{n+1} from E^{n+1} using a root finder algorithm**. When E has been solved at timestep $n+1$, A^{n+1} can be recovered by applying the Newton-Raphson root finder method to Eq. (3.1.16). This amplitude is then used to find the wind power input P^{n+1}.

4. **Repeat steps 2 and 3 for the desired number of timesteps**.

5. **Find separate kinetic and potential energy**.
   Once A has been found for all timesteps, kinetic and potential energy are calculated to complete the method.

3.1.3 A baroclinic decay timescale

A decay timescale for the baroclinic eddy due to relative wind stress damping can be found from

$$T_{bc} = E/P_{rel} \; , \tag{3.1.19}$$

where E is the domain integral of baroclinic energy (3.1.16) and P_{rel} is wind power input due to relative wind stress (3.1.13b). Choosing the following parameter values: $H = 4000$ m, $H_1 = 800$ m, $\rho_1 = 1026$ kg m^{-3}, $\rho_2 = 1029$ kg m^{-3}, $R = 100$ km, $f = 10^{-4}$, the viscous damping term is an order of magnitude smaller [$O(10^6)$] than P_{rel} [$O(10^7)$], and can be neglected. Putting the above parameter values into (3.1.19), a decay timescale to leading order looks like

$$T_{bc} \approx \frac{\rho_0 R^2 g\prime f^2}{2\rho_a\left(2a_1 + 3a_2\left|u_a\right| + 4a_3\left|u_a\right|^2\right)g^2\mu^2} \; . \tag{3.1.20}$$

Compared to the barotropic timescale, T_{bt} (Eq. (2.1.25) in chapter 2), we see that T_{bc} includes additional parameters ($g\prime$, μ, and R) as a result of the two-layer stratification. In addition, T_{bc} to leading order is not dependent on eddy amplitude, A, despite both E and P_{rel} being functions of A. Here, the leading order term comes from the potential energy of the eddy's interface displacement, η_1/μ, as this is the largest contributor to total baroclinic eddy energy. This dominance of potential energy was not the case in the barotropic timescale, which was found to depend on kinetic energy. Therefore, the baroclinic decay timescale depends on relative wind stress' ability to dampen this interface displacement. This is consistent with the notion that relative wind stress attenuates eddies by relaxing their interface displacements via wind-induced Ekman pumping (Dewar and Flierl, 1987). The barotropic decay timescale, T_{bt} and the timescale put forward by Gaube et al. (2015) ask how quickly relative wind stress can dampen the eddy motion. Instead, T_{bc} asks on what timescale relative wind stress can dampen potential energy, a considerably larger reservoir of energy compared to kinetic energy (Lorenz, 1955).

Figure 3.1.2 shows how the baroclinic decay timescale (3.1.20) varies with wind speed and eddy radius. A typical midlatitude eddy with radius 100 km and wind speed 7 m s^{-1} gives a decay timescale of around 1000 days. As the eddy radius increases, the timescale to dissipation increases too. This is because potential energy held by the interface displacement depends on R, whilst the wind power input due to relative wind stress is independent of R. Modifying wind speed is also expected to have an impact since increasing wind speed increases the wind power input (see Fig. 2.1.4 in chapter 2).

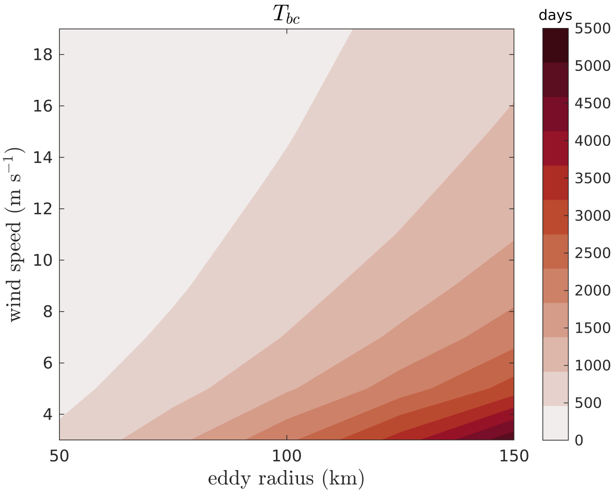

Figure 3.1.2: Baroclinic decay timescale, T_{bc} from (3.1.20) plotted as a function of wind velocity, u_a and eddy e-folding radius, R. Timescale is in days.

3.2 Experimental design

3.2.1 Numerical model design

The numerical model used to examine the accuracy of the two-layer prediction in section 3.1.2 is the hydrostatic MIT general circulation model (Marshall et al., 1997b,a). Here, we outline the general design for MITgcm.

All experiments use the equations of motion on an f-plane, Cartesian grid with Boussinesq and hydrostatic approximations. The linear equation of state for density is employed, taking into account only temperature. The model grid uses a vertical resolution of 91 z-levels over a depth of 4000 m, starting with grid spacings of 5 m near the surface, and 100 m at the ocean bottom. This grid is generated using Stewart et al. (2017) and is designed to ensure that baroclinic modes are correctly resolved in z-coordinate ocean models. In the horizontal, the domain spans 2000 km in the x and y directions with equal grid spacing of 10 km. This ensures mesoscale dynamics can be well represented whilst also being computationally inexpensive. The ocean bottom is flat and a free-slip boundary condition is used, along with no bottom drag. Neglecting bottom drag may have repercussions for the growth of the barotropic mode (Scott and Arbic, 2007).

Parameter	Symbol	Value	Units
Horizontal grid spacing	$\Delta x, y$	10	km
Vertical grid spacing	Δz	5 to 100	m
Domain size	$L_{x,y}$	2000	km
Reference density	ρ_0	1026	kg m^{-3}
Atmospheric surface density	ρ_a	1.2	kg m^{-3}
Thermal expansion coeficient	α	2×10^{-4}	$^{\circ}$C^{-1}
Biharmonic viscous coefficient	A_4	8×10^{10}	m^4 s^{-1}
Biharmonic diffusive coefficient	κ_4	3.2×10^9	m^4 s^{-1}
Vertical viscous coefficient	A_z	10^{-4}	m^2 s^{-1}
Vertical diffusive coefficient	κ_z	10^{-5}	m^2 s^{-1}
Timestep	Δt	400	s

Table 3.1: Key MITgcm parameters.

However, its neglect means damping by relative wind stress can be isolated in our model. The north-south and east-west boundaries are doubly re-entrant, so anything that leaves will re-enter from the boundary edge. A temperature sponge layer of 100 km is used at all boundary edges to ensure no waves emitted from the eddy re-enter the domain. A timestep of $\Delta t = 400$ s is employed, satisfying the CFL condition.

The model employs biharmonic viscosity to parameterise the dissipation of energy at small scales whilst allowing the larger scales to evolve freely. This ensures numerical stability over the total model simulation. We find that smaller biharmonic viscosity produces a less stable eddy, whilst larger values produce long lasting stable eddies. Katsman et al. (2003) note that large viscosity values suppress the growth of instabilities, assisting in eddy longevity. It will be shown in section 3.3 that a potentially unstable eddy occurs within a reasonable timeframe ($\sim$ 6 months). Temperature is also subject to biharmonic diffusion. The Prather advection scheme (Prather, 1986) is used in the temperature equation to preserve any sharp frontal structures that might arise in the flow. The use of the Prather scheme has been found to reduce levels of spurious diapycnal mixing in high resolution z-level models (Hill et al., 2012; Ilıcak et al., 2012). In the vertical, viscosity and diffusivity is applied to provide some vertical mixing. A convective adjustment parameter is also applied to avoid static instability. Model parameters are found in Table 3.1.

3.2.2 Model initialisation

The intention is to assign initial conditions to MITgcm that approximately resemble the two-layer shallow water equations of (3.1.1).

Stratification

To investigate the spin-down of an eddy, the eddy profile needs to be in an initial state of balance. Therefore, temperature and density profiles are created a-priori, and velocities are determined from the 3D temperature field and sea surface height.

From Dunphy (2009), a background density is given by

$$\rho_{ref}(z) = \rho_0(1 - N_0^2(z/g)) + 0.5\Delta\rho(1 - \tanh(B(z + H_1)/H)) \,, \tag{3.2.1}$$

where N_0 is a reference buoyancy frequency, z is depth, $\Delta\rho$ is the difference in density between the surface and ocean bottom, B is the gradient of the density profile. The subscript $\cdot_{ref}$ implies the reference background state. Key eddy parameter values are stated in Table 3.2. The choice of a small N_0 is based on wanting a $\rho_{ref}(z)$ that is almost constant in each layer, something that resembles the two-layer model (Sec. 3.1.1), but one that will also not give a zero vertical density gradient. Maximum values of buoyancy frequency are around $N = 10^{-3}$ s^{-1} (Fig. 3.2.1c), consistent with other eddy studies (Molemaker and Dijkstra, 2000). The vertical temperature profile is found by inverting the linear equation

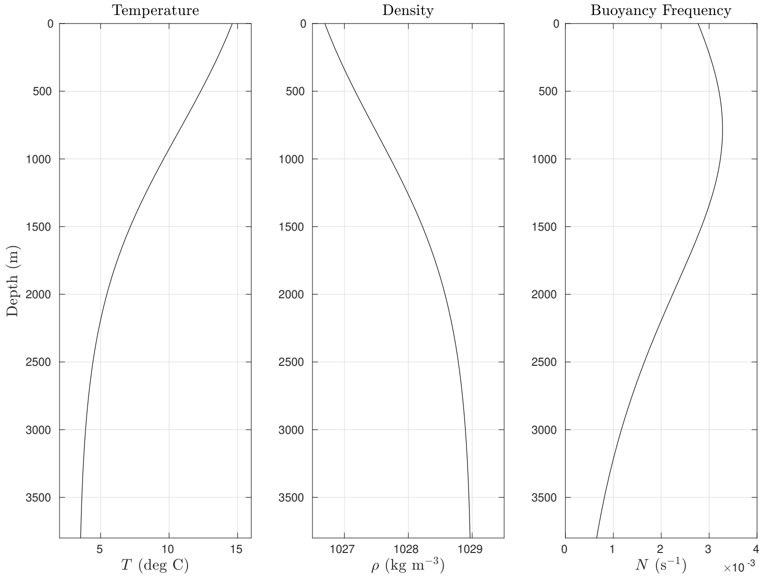

Figure 3.2.1: Typical temperature, density and buoyancy frequency profiles of MITgcm model.

of state

$$T_{ref}(z) = -\Big(\frac{\rho_{ref}(z) - \rho_0}{\alpha\rho_0} - T_0\Big) \ , \tag{3.2.2}$$

where α is the thermal expansion coefficient, and T_0 is a reference ocean temperature in degrees Celsius. It is noted that ρ_{ref} and T_{ref} remain equivalent in anticyclone and cyclone setups. The 3D temperature field is calculated using a Gaussian function and an exponential decay in the vertical

$$T(x, y, z) = T' e^{-(x^2+y^2)/R^2} e^{-\gamma(z/D)} + T_{ref}(z) \ , \tag{3.2.3}$$

where T' is the eddy temperature anomaly, and γ and D both govern the stratification down the water column. This setup was devised so that the layer depths between the two-layer model and MITgcm match i.e. H_1 is the same in each setup. Figures 3.2.2a and 3.2.2b show this temperature profile in depth for an anticyclone and cyclone, respectively; the isopycnals are depressed in the anticyclone and raised in the cyclone.

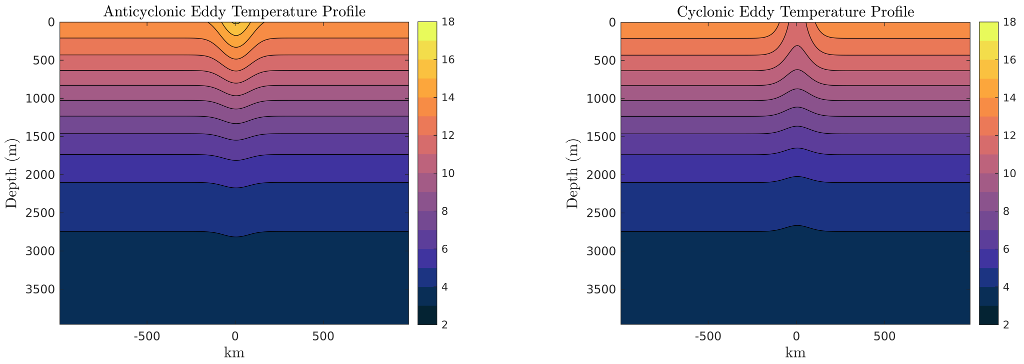

(a) (b)

Figure 3.2.2: Transects of typical initial temperature profiles for an a) anticyclone and b) cyclone. Contour values are shown in deg C.

Parameter	Symbol	Value	Units
Density, layer 1	ρ_1	1026	kg m^{-3}
Density, layer 2	ρ_2	1029	kg m^{-3}
Reference buoyancy frequency	N_0	10^{-5}	s^{-1}
Density profile gradient	B	3	-
Ocean depth, layer 1	H_1	800	m
Ocean depth, total	H	4000	m
ACE Eddy amplitude	A	25	cm
CE Eddy amplitude	A	-25	cm
Reference temperature	T_0	18	°C
ACE Temperature anomaly	T'	2.5	°C
CE Temperature anomaly	T'	-2.5	°C
Temperature gradient	γ	1	-
Coriolis freqeuncy	f	9.3461×10^{-5}	s^{-1}

Table 3.2: Initialisation parameter values in MITgcm.

Velocity Profile

Using the Gaussian sea surface height

$$\eta(x, y) = Ae^{(-(x^2+y^2)/R^2)}\ , \tag{3.2.4}$$

and the 3D temperature field in Eq. (3.2.3), initial velocities are found through geostrophic and thermal wind balance

$$u(x,y,z) = -\frac{g}{f}\frac{\partial \eta}{\partial y} - \frac{g\alpha}{f}\int_H^z \frac{\partial T}{\partial y}\,dz\ , \tag{3.2.5a}$$

$$v(x,y,z) = \frac{g}{f}\frac{\partial \eta}{\partial x} + \frac{g\alpha}{f}\int_H^z \frac{\partial T}{\partial x}\,dz\ . \tag{3.2.5b}$$

The first part of each equation is the surface velocity derived from the sea surface height, and the second part is the vertical shear derived through thermal wind balance. Because the two-layer shallow water model in Eq. (3.1.1) is chosen to exhibit a first baroclinic mode, this implies that the depth-average flow is zero, i.e. no barotropic mode. In setting up these initial conditions, the aim is to minimise the depth-average flow as much as possible in a realistic stratification, and this is done by choosing appropriate model parameters, such as A, T', γ and D, displayed in Tables 3.1 and 3.2. However, we anticipate there to be a mixture of barotropic and baroclinic modes in the MITgcm, as is the case in the real ocean (Wunsch, 1997; Arbic and Flierl, 2004).

A consequence of the parameters chosen is also that kinetic energy will differ between the two-layer model and MITgcm. For example, choosing parameters from Table 3.2 to use in the two-layer model, the maximum velocity at the eddy speed based radius ($\sim$ 75 km) in the two-layer model exceeds MITgcm in the upper layer (Fig. 3.2.3). Nevertheless, we can ensure a few of the salient features in each setup are consistent, such as layer depth, sea surface height, and opposing flow in each layer. Fig. 3.2.4 shows distinct upper and lower layers for an anticyclone in MITgcm that display counter-rotating velocities, which is also a feature of a dominant first baroclinic mode setup (Cushman-Roisin and Beckers, 2006). Some points on potential energy will be made in section 3.2.3.

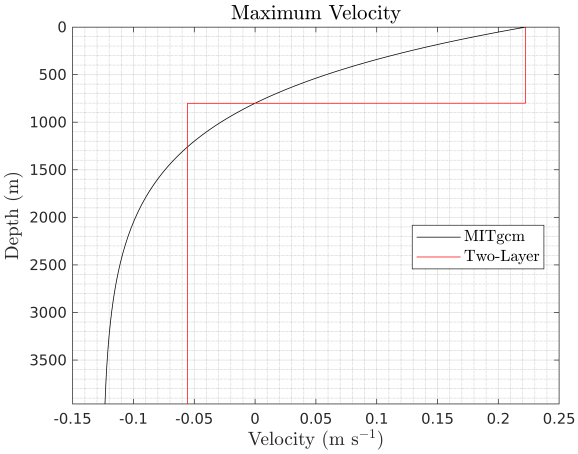

Figure 3.2.3: Comparison of zonal velocity at eddy speed based radius ($L_s = 2^{-1/2}R = 75$ km) between MITgcm (black) and two-layer (red) for a typical midlatitude anticyclonic eddy. Eddy parameters are found in Table 3.2.

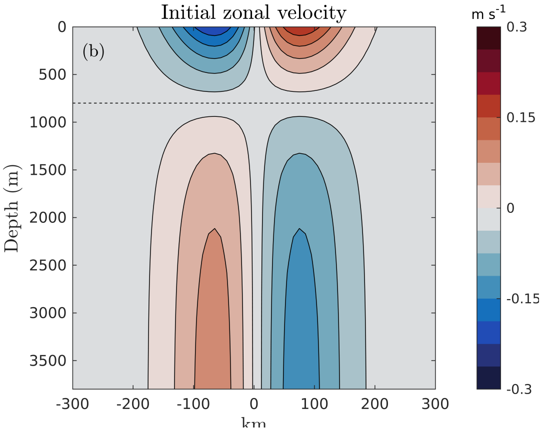

Figure 3.2.4: Meridional transect displaying upper and lower layer zonal velocities in MITgcm for an anticyclonic eddy. Units in m s^{-1}. Dashed line is the depth of the thermocline, $H_1 = 800$ m. Eddy parameters are found in Table 3.2.

Model Adjustment

Prior to starting the numerical experiments, a model adjustment phase of 10 days is run. This allows any imbalances in either sea surface height, velocity or temperature to die down before turning on the wind forcing. For an eddy with initial sea surface height amplitude of 25 cm, Fig. 3.2.5 shows how the value adjusts to around 25.68 cm over the first day. Starting the model experiments from model day 10 means that any disturbances caused by an initial imbalance will have little effect on the eddy. This approach is clearly different to our barotropic case where we could allow any initial imbalances a much longer time period to die down. This is because the eddy setup chosen here is unlikely to remain coherent, and will destabilise as a result of the opposing flow in the upper and lower layer (Dewar and Killworth, 1995). Therefore, a shorter period of adjustment is acceptable. Wilder et al. (2022) describe in more detail the conditions under which the eddy departs from its initial coherent structure.

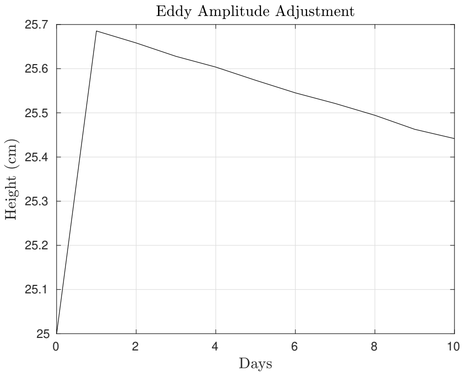

Figure 3.2.5: Typical adjustment of maximum eddy sea surface height over 10 days for an anticyclonic eddy.

Wind Profile

Following McGillicuddy (2015), a constant background wind begins in the zonal direction, and is then rotated $2\pi/64$ every hour, meaning the wind vectors make one full rotation every 64 hrs. The wind vectors are

$$u_a^n = \cos\left(\frac{2\pi}{64}\right)u_a^{n-1} - \sin\left(\frac{2\pi}{64}\right)v_a^{n-1}\ , \tag{3.2.6a}$$

$$v_a^n = \sin\left(\frac{2\pi}{64}\right)u_a^{n-1} + \cos\left(\frac{2\pi}{64}\right)v_a^{n-1}\ , \tag{3.2.6b}$$

where superscripts $\cdot^n$ denote the vector iteration, or hour. Choosing this rotation period avoids resonance with the inertial frequency, f. If the wind rotation and eddy evolve at the same frequency, this could create unphysical interactions. Furthermore, the rotating wind also minimises disturbances in eddy shape and discontinuities in sea level height at the boundary edges due to horizontal Ekman transport.

3.2.3 A note on the prediction method

For the prediction method, potential energy is matched because it dominates over kinetic energy (Lorenz, 1955), and it will be seen that this is the case in section 3.3.1. Potential energy cannot be varied in MITgcm as the stratification has been used to produce a kinetic energy profile with consistent features across each setup e.g. layer depths and eddy amplitude. Therefore, potential energy is matched to MITgcm levels by adjusting the lower layer density, ρ_2 in the two-layer model, for which an approximate value is chosen to be 1026.9 kg m^{-3}. The advantage of this allows the prediction method to find an eddy amplitude that is based on equivalent energy levels.

3.2.4 Diagnosing MITgcm energetics

To validate the evolution of energy in the two-layer model (3.1.1), time-mean kinetic and potential energy, and wind damping for the continuously stratified MITgcm model need to be defined. In the following terms, the time-mean is taken to be a 16-day rolling average. This time-mean is chosen to avoid aliasing a signal that might occur from averaging a non integer multiple of wind rotations (see 3.2.2). The following are mean potential energy, mean kinetic energy, and wind power input

$$PE = -\int_V \frac{g}{2n_0(z)}\overline{\rho^*(x,y,z,t)}^2 \, dV \ , \quad \text{and} \tag{3.2.7}$$

$$KE = \int_V \frac{\rho_0}{2}(\overline{u}_g^2 + \overline{v}_g^2) \, dV \ , \tag{3.2.8}$$

$$P = \int_S \overline{\boldsymbol{\tau}} \cdot \overline{\boldsymbol{u}}_{gs} \, dS \ , \tag{3.2.9}$$

where $\bar{\cdot}$ represents a 16 day time-mean, $\rho^*(x,y,z,t) = \rho(x,y,z,t) - \rho_{ref}(z)$ is a density anomaly relative to a constant-in-time reference background density state, $n_0(z)$ is the vertical gradient of $\rho_{ref}(z)$, u_g and v_g are geostrophic velocity components in the zonal and meridional direction, subscripts $\cdot_{gs}$ are geostrophic surface, and $\int_V$ is a volume integral. Definitions of $\rho(x,y,z,t)$, ρ_{ref} and geostrophic velocity are found in section 3.2.2. The use of potential energy anomaly informs how much potential energy can be converted into kinetic energy, as opposed to how much potential energy exists within the stratification. Choosing the potential energy definition in (3.2.7) implies a quasi-geostrophic framework and has been employed in previous energy analyses (Chen et al., 2014; Youngs et al., 2017).

3.3 Results

The following sections present findings of the prediction method (Pred) and continuously stratified model (MIT) for an anticyclone (ACE) and cyclone (CE), where both are subject to absolute (AW) and relative (RW) wind stress. All simulations are run for 330 days.

3.3.1 Anticyclonic and cyclonic eddy prediction

Here, we present results for the prediction method based on matching potential energy levels between the prediction and MITgcm. The idea is to validate this prediction method, whilst suggesting possible reasons for any differences that occur.

Total energy and dissipation

A time series of domain integrated eddy energy ($KE + PE$) for an ACE and CE is shown in Fig. 3.3.1. The first thing that can be seen is the initial offset in total energy between Pred and MIT in ACE and CE. In this case, potential energy is being matched. However, it was mentioned in section 3.2 that kinetic energy is not equivalent between Pred and MIT, and this is the reason for the initial energy offset. Moving onto the ACE, the decay rates of Pred and MIT are fairly consistent (Fig. 3.3.1a). In the absolute wind stress case (AW), viscous dissipation erodes the eddy's energy, and so AW Pred and MIT lose 0.1 PJ up to day 150. Beyond day 170, Pred and MIT time-series begin to diverge, with MIT undergoing a sudden reduction in total energy of around 10% over 30 days, whilst Pred continues with a linear decay. This divergence indicates that MIT is no longer evolving linearly, suggesting the eddy undergoes an instability process. In the relative wind stress case (RW), there is an additional decay of energy in response to the negative wind power input by relative wind stress (Fig. 3.3.2a). Up to day 150, RW Pred loses 0.38 PJ whilst RW MIT loses around 0.4 PJ, relative to day 31 in RW time-series. If the MIT eddy energy were to decay linearly for all time, a baroclinic decay timescale would come out at around 3700 days, in line with the the analytical decay timescale (3.1.20). This damping is similar because the wind power input in Pred and MIT is around -3×10^7 W. The sudden reduction in total eddy energy (of ∼10%) also takes place in RW but earlier by ∼ 10 days. This may suggest that relative wind stress introduces instability processes earlier in RW MIT. These non-linearities also impact the relative wind power input, since P_{rel} displays a sharp increase in negative wind power input (Fig. 3.3.2).

Similar results are also observed for the CE (Fig. 3.3.1b). The decay rate in total eddy energy follows roughly the same outline as the ACE for 150 days, with more damping taking place in RW Pred and RW MIT than in the AW case due to negative wind power input (Fig. 3.3.2b). As was shown in chapter 2, wind power input due to relative wind stress is independent of eddy polarity, so no bias in damping rate should exist. Over the first 130 days, RW Pred is damped by 0.37 PJ, and RW MIT is damped by 0.26 PJ. The lesser MIT decay is observed through the converging total energy values at around day 115. After day 150, MIT exhibits a sudden reduction in total energy with each wind stress, which happens earlier in RW. Moreover, in contrast to the ACE, the timescale for this sudden reduction to take place in the CE is around 15-20% smaller. This points to an anticyclone-cyclone asymmetry, which has been recognised in past studies (Chelton et al., 2011; Mkhinini et al., 2014; Mahdinia et al., 2017).

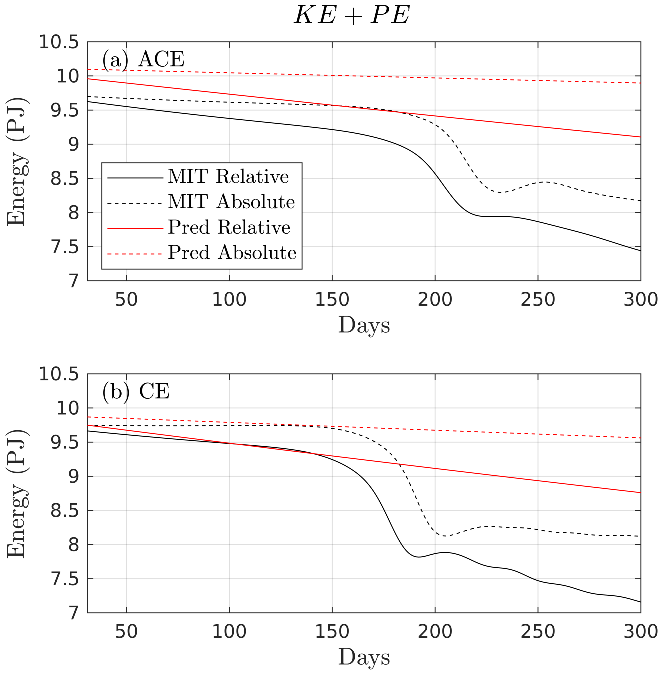

Figure 3.3.1: Time-series of total eddy energy for a) anticyclone, and b) cyclone. MITgcm shown in black, and predicted shown in red, with absolute wind stress in dashed line and relative wind stress in full line. Units of energy in PJ. MITgcm values are 16 day time-means.

Another difference between each eddy type is the slight increase in CE AW MIT total energy. A simple explanation for this total energy increase is due to the production of potential energy caused primarily by vertical diffusive processes. This offers a reason for the different decay in total energy between Pred and MIT. A more thorough examination of the cyclonic eddy response to relative wind stress is made in chapter 5.

Decomposed energy

Further insights into possible discrepancies in decay rate can be gained by decomposing total energy into kinetic (KE) and potential (PE) energy, shown in Fig. 3.3.3. Beginning with the ACE (Fig. 3.3.3a,b), PE is almost an order of magnitude larger than KE, therefore much of the total energy (Fig. 3.3.1a) is governed by the evolution of PE. For AW, the decay rate of MIT PE and KE fits well with Pred for at least 150 days. The decay rate of Pred KE and PE

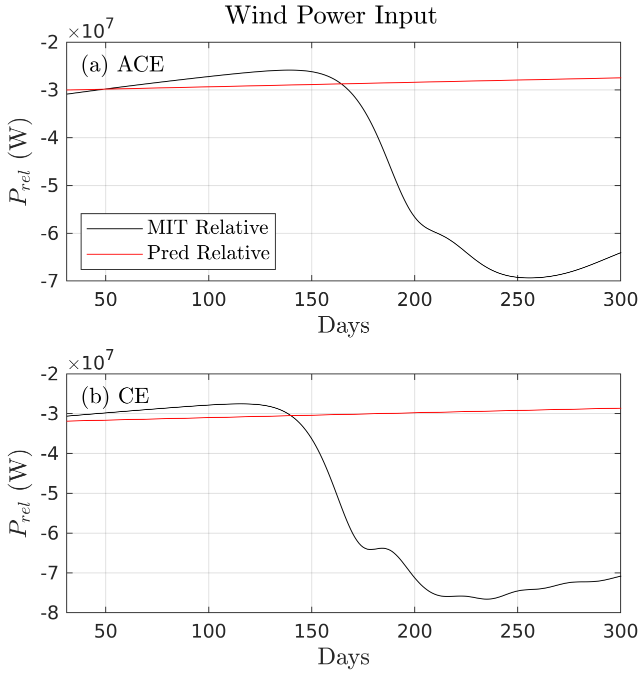

Figure 3.3.2: Time-series of total wind power input in relative wind stress simulation for a) anticyclone and b) cyclone. MITgcm in black line and predicted in red line. Units of power in W. MITgcm values are 16 day time-means.

match the evolution of Pred SSH (Fig. 3.3.4a), since both energy terms are calculated using these SSH values acquired from the prediction method. The difference in KE values between MIT and Pred is a consequence of the continuous stratification employed in the MITgcm setup (see Sec. 3.2.2). This mismatch in KE values also generates the mismatch in total energy (Fig. 3.3.1a). In MIT, the sudden reduction in PE coincides with a sharp rise in KE, indicating that a common cause exists between these two quantities.

Now for RW, MIT and Pred PE are damped similarly by relative wind stress (Fig. 3.3.3a).The sudden reduction in PE and growth in KE take place earlier (Fig. 3.3.3a,b), as seen in total energy (Fig. 3.3.1a). Also, relative wind stress damps Pred KE due to its negative wind power input (Fig. 3.3.2a). However, MIT KE is found to undergo less damping than it experiences in AW, contrary to the picture shown by Pred. The correlation between PE and KE can give some idea why less MIT KE damping takes place. This is examined in detail in chapter 4 and in Wilder et al. (2022). However, we mention a possible reason for the differences in RW Pred and MIT here. Building upon the suggestion

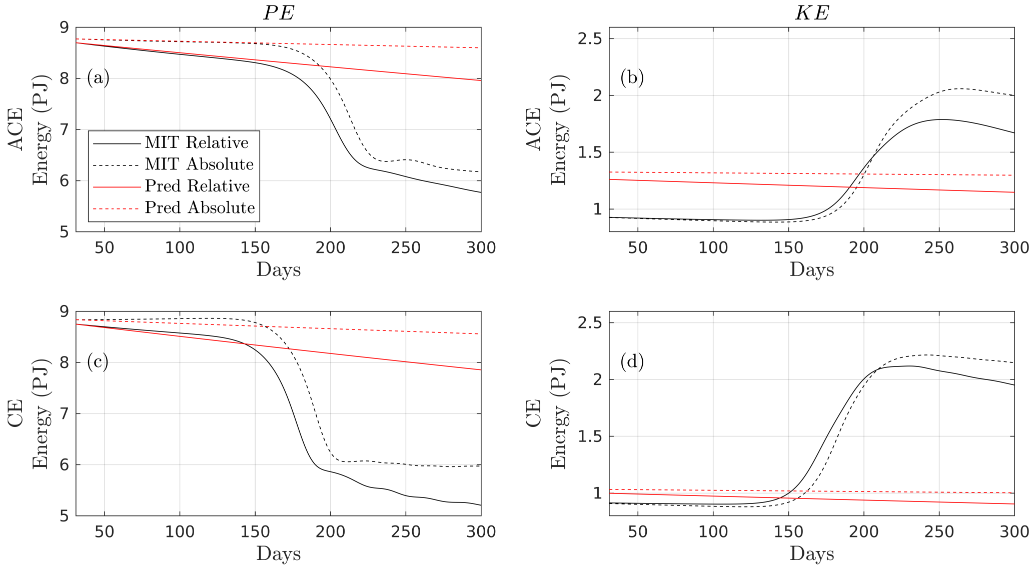

Figure 3.3.3: Time-series of: a,c) potential energy and b,d) kinetic energy for top) anticyclone, and bottom) cyclone. MITgcm shown in black, and predicted shown in red, with absolute wind stress in dashed line and relative wind stress in full line. Units of energy in PJ. MITgcm values are 16 day time-means.

that PE is correlated with changes in KE, RW MIT could initiate a transfer of PE into KE, which cannot be efficiently removed by P_{rel}. In the two-layer energy equation (3.1.7), there are no terms that represent the transfer of energy between potential and kinetic energy, so no conversion of energy takes place in Pred. Therefore, Pred exhibits damping by relative wind stress in a completely efficient manner i.e. relative wind stress is nothing but a drag on the eddy.

The CE's overall response is similar to the ACE, along with its shorter timescale for changes in KE and PE (Fig. 3.3.3c,d). Nevertheless, a few points are worth mentioning. First, the increase in AW MIT total energy observed in Fig. 3.3.1b is seen in AW MIT PE. Changes to ρ^* from Eq. (3.2.7) are likely due to vertical diffusion, though why this is more prevalent in CE than ACE is unclear. Second, Pred and MIT KE are closer in value in CE than they are in ACE. This is because in Pred the interface displacement in ACE (CE) is depressed (raised), producing a thicker (thinner) upper layer, and subsequently higher (lower) levels of KE. However, ACE MIT and CE MIT both use the same background density profile with oppositely signed density anomalies, thus producing the same levels of kinetic energy.

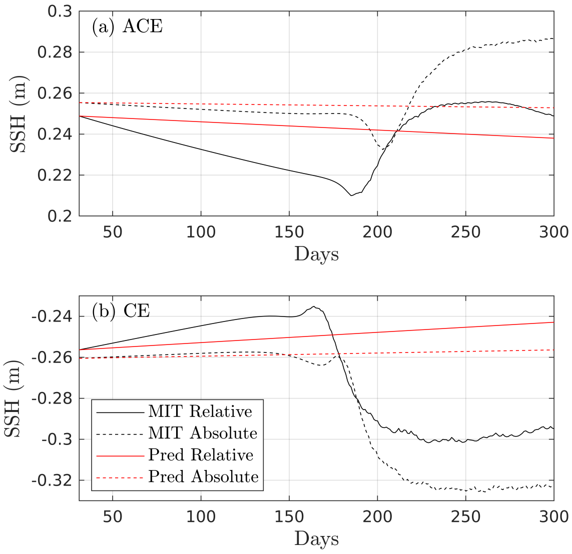

Figure 3.3.4: Time-series of sea surface height for a) anticyclone and b) cyclone. MITgcm shown in black, and predicted shown in red, with absolute wind stress in dashed line and relative wind stress in full line. Units in m. MITgcm are daily time-mean values.

Sea surface height

We now explore the evolution of eddy sea surface height shown in Fig. 3.3.4, and attempt to make links with the energy prediction results, as well as theory. Fig. 3.3.4 shows a clear downward trend in SSH across Pred and MIT over the first 150 days. This trend is also consistent with a decrease in total energy (Fig. 3.3.1), which points towards the relaxation of the main thermocline displacement. In ACE, AW SSH is closely aligned in Pred and MIT, until MIT undergoes sudden changes. In RW, the rate of decay is divergent, with MIT displaying a reduction of 3 cm over 150 days, whilst Pred decreases by only 0.5 cm over this time frame. The case is similar in the cyclonic eddy, though the rate of decay is smaller in RW, in line with results seen in total energy (Fig. 3.3.1b).

We now attempt to link the evolution of SSH and eddy energy with some well known literature. Because SSH reflects the first baroclinic mode (BC1), which dominates the surface geostrophic kinetic energy (Wunsch, 1997), an SSH decay could imply a dampening of BC1. Looking at the anticyclonic eddy (Fig. 3.3.4a), the decay in RW Pred SSH, as well as PE and KE (Fig. 3.3.3a,b) suggests a damping of BC1 by relative wind stress, since the theory only contains BC1 structure. Yet in RW MIT, the decay in SSH and PE does not coincide with a decay in KE. Speculatively, this might imply that the ACE is no longer exhibiting a dominant first baroclinic mode structure, where in fact energy is cascading away from BC1, possibly into the barotropic mode. Indeed, a downwards vertical transfer of kinetic energy collected in the barotropic mode prior to bottom drag dissipation is a recognised process (Scott and Wang, 2005). What is more, the rate at which RW SSH decays compared to AW SSH in MIT suggests that relative wind stress may also enhance this cascade. This mechanism fits with our hypothesis that PE might be supplying KE. The next logical step to see whether this is taking place would be to follow the analysis as per Scott and Wang (2005), however, this is beyond the scope of this current work.

Furthermore, we can also consider the decay rate of SSH and total eddy energy, highlighting their dependence. Following the quadratic dependence of eddy energy on eddy amplitude in the barotropic eddy (chapter 2), a similar response in the baroclinic eddy is expected. By day 150, ACE RW Pred total energy (Fig. 3.3.3a) has decayed by around 4%, whilst RW Pred SSH (Fig. 3.3.4) has decayed by only 2%.

Prediction break down

We can offer reasons for the break down in eddy energy prediction. It is known that the stability of mesoscale eddies depends on the direction of deep layer flow with respect to its surface rotation, i.e. counter-rotating eddies are unstable (Dewar et al., 1999). The numerical model is set up to match the two-layer theory as closely as possible, in terms of matching energy. This setup produces an anticyclone and cyclone with a counter-rotating lower layer, which have unstable azimuthal wavenumbers (Katsman et al., 2003). Therefore, it is not unreasonable to suggest that the method breaks down due to the eddy being initially unstable.

It is also worth mentioning that the barotropic eddy in chapter 2 showed no signs of departure between Pred and MIT. This can be explained through the lack of any baroclinic component and it also being stable to barotropic instability.

3.3.2 Horizontal maps of kinetic energy

We now examine horizontal patterns of MITgcm kinetic energy in an attempt to illustrate why the prediction method breaks down. Figure 3.3.5 displays kinetic energy profiles averaged over the top 800 m at days 100 and 150 for the anticyclone and cyclone. The choice of days will show the eddy evolving into an unstable state. Beginning with the anticyclone under absolute wind stress, at day 100 the eddy appears circular and stable (Fig. 3.3.5a). By day 150, the ACE is elliptical and has two regions of strong kinetic energy in its east and west sides (Fig. 3.3.5b), indicating a growth of the second azimuthal wavenumber (Baey and Carton, 2002). In the relative wind stress experiment, the ACE evolves similarly but kinetic energy is weaker due to relative wind stress damping (Fig. 3.3.5e,f). However, this damping of kinetic energy is not consistent with the domain integrated timeseries data in Fig. 3.3.3b, suggesting there must be vertical variations in kinetic energy.

Under absolute wind stress, the cyclonic eddy displays a circular shape at day 100 (Fig. 3.3.5c). By day 150 there exists a departure from this circular symmetry (Fig. 3.3.5d). In relative wind stress, CE kinetic energy is weaker at day 100, but slightly larger than AW levels at day 150 (Fig. 3.3.5g,h). Domain integrated KE at day 150 is also greater in RW than AW (Fig. 3.3.3c). CE at day 150 exhibits slightly more pronounced spiral arms than the ACE and indicates the eddy has entered a highly unstable state. The departure of each eddy from its initial symmetrical state offers further reason why the prediction method breaks down.

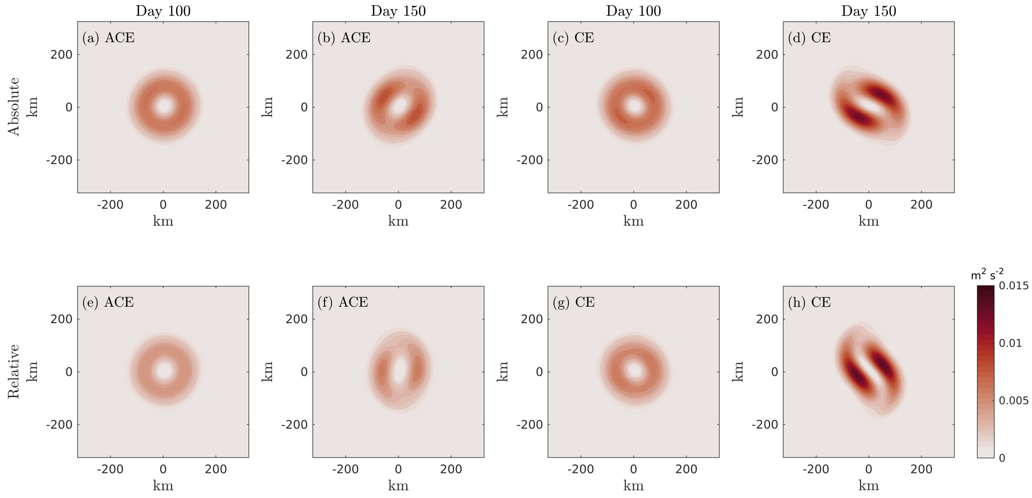

Figure 3.3.5: Horizontal patterns of kinetic energy ($\frac{1}{2}(\overline{\boldsymbol{u}} \cdot \overline{\boldsymbol{u}})$) averaged over top 800 m for a,b,e,f) anticyclone and c,d,g,h) cyclone. Top) absolute wind stress simulation, and, bottom) relative wind stress simulation. Values are 16 day time-means and units in m^2 s^{-2}.

3.4 Concluding chapter remarks

This chapter set out to validate whether the damping of baroclinic total eddy energy by relative wind stress in an idealised numerical model could be predicted using simple theoretical techniques. Being able to accurately predict the decay of baroclinic eddies in the global ocean is vital to offer improved estimates of global ocean heat transport and uptake (Mak et al., 2022). The prediction method devised in chapter 2 has thus been extended to account for a two-layer baroclinic eddy, consistent with the ubiquitous nature of baroclinic eddies in the ocean (Chelton et al., 2011). From this extended theory, a baroclinic decay timescale was derived, showing relative wind stress attenuates the interface displacement, or largest reservoir of potential energy.

In section 3.3.1 we ensured the prediction had equivalent total energy with respect to MITgcm. Both anticyclonic and cyclonic eddies were examined. The analytical wind power input derived in chapter 2 was found to produce rates of decay similar to that seen in the MIT relative wind stress simulation for each eddy polarity (Fig. 3.3.1). A decay timescale (3.1.20) of $\sim$ 3700 days for a completely stable eddy was found, around three times past estimates for eddy lifetime (Xu et al., 2016). The eddy's unstable nature prevents a complete use of (3.1.20) in this setup. Eddy attenuation by interface relaxation is exhibited though the reduction in potential energy in Pred and MIT through each eddy. However, it was interesting to observe the lack of damping in RW MIT KE, along with an enhanced decay of sea surface height in RW MIT. To this end, it was put forward that an energy conversion takes place that directs energy away from the first baroclinic mode, thus damping SSH but not KE.

The robustness of this prediction method is found to break down when the eddy enters an unstable regime. This is made clear by the sudden exponential changes in MIT kinetic and potential energy (e.g. Fig. 3.3.1 in section 3.3.1), and also through the non-circular horizontal eddy shape, shown in section 3.3.2. The horizontal profiles of MIT KE provide further evidence as to why the prediction method breaks down. The elliptical evolution and spiral arms imply the eddy is becoming unstable as a result of its counter-rotating structure, and hence contribute to a break down of the prediction method.

The prediction method is clearly capable of predicting the damping of total eddy energy in the first baroclinic mode in response to relative wind stress. Therefore, a simple parameterisation for eddy damping by relative wind stress could be proposed from this work. However, mesoscale eddy stability could pose limitations to this method. A further direction in this regard would be to incorporate the implied energy conversion and unstable changes in eddy energetics into the parameterisation.

In the next chapter, a detailed examination of the dynamical response of the baroclinic eddy to absolute and relative wind stress is carried out. The purpose of this next work is to further understand the eddy response to relative wind stress, with a particular focus on its energetics.

4

The Response of a Baroclinic Anticyclonic Eddy to Relative Wind Stress Forcing

---

Preamble This study has been published in Journal of Physical Oceanography with the same title by Thomas Wilder, Xiaoming Zhai, David Munday and Manoj Joshi. From hereon it will be referred to as Wilder et al. (2022). The text in this chapter is mostly unchanged, except for some minor corrections and the inclusion of the final section 4.6. The work has been carried out mostly by TW, under supervision by XZ and MJ at University of East Anglia, and DM at British Antarctic Survey.

4.1 Abstract

Including the ocean surface current in the calculation of wind stress is known to damp mesoscale eddies through a negative wind power input, and have potential ramifications for eddy longevity. Here, we study the spin-down of a baroclinic anticyclonic eddy subject to absolute (no ocean surface current) and relative (including ocean surface current) wind stress forcing by employing an idealised high-resolution numerical model. Results from this study demonstrate that relative wind stress dissipates surface mean kinetic energy (MKE) and also

generates additional vertical motions throughout the whole water column via Ekman pumping. Wind stress curl-induced Ekman pumping generates additional baroclinic conversion (mean potential to mean kinetic energy) that is found to offset the damping of surface MKE by increasing deep MKE. A scaling analysis of relative wind stress-induced baroclinic conversion and relative wind stress damping confirms these numerical findings, showing that additional energy conversion counteracts relative wind stress damping. What is more, wind stress curl-induced Ekman pumping is found to modify surface potential vorticity gradients that lead to an earlier destabilisation of the eddy. Therefore, the onset of eddy instabilities and eventual eddy decay takes place on a shorter timescale in the simulation with relative wind stress.

4.2 Introduction

Baroclinic mesoscale eddies exist across much of the ocean and evolve on timescales of months to years (Chelton et al., 2011). Anticyclonic (cyclonic) eddies are categorised as having positive (negative) sea level and temperature anomalies that typically display depressed (raised) isopycnal surfaces. Eddies are energetic features that dominate the ocean's kinetic energy budget (Ferrari and Wunsch, 2009), making them efficient at redistributing oceanic properties (Zhang et al., 2014; Thompson et al., 2014). Interactions between atmospheric winds and mesoscale eddies have important consequences for ocean dynamics, and as such have been the focus of numerous studies (Gaube et al., 2013; Xu et al., 2016; Oerder et al., 2018; Song et al., 2020).

The dissipation of eddies has been attributed to a handful of mechanisms, ranging from bottom drag (Arbic and Scott, 2008), internal lee waves (Clément et al., 2016), western boundary graveyard effects (Zhai et al., 2010), and ocean current-wind interaction, known herein as 'relative wind stress' (Duhaut and Straub, 2006; Zhai and Greatbatch, 2007; Zhai et al., 2012). Relative wind stress takes into account the relative motion between surface winds and ocean currents. It is parameterised by

$$\boldsymbol{\tau}_{rel} = \rho_a C_d |\boldsymbol{u}_a - \boldsymbol{u}_s|(\boldsymbol{u}_a - \boldsymbol{u}_s) \ , \tag{4.2.1}$$

where ρ_a is air density, C_d is a drag coefficient that is a function of wind speed, $\boldsymbol{u}_a$ is the atmospheric wind 10 m above the ocean surface, and $\boldsymbol{u}_s$ is the ocean surface current. Neglecting $\boldsymbol{u}_s$ in Eq. (4.2.1) gives

$$\boldsymbol{\tau}_{abs} = \rho_a C_d |\boldsymbol{u}_a| \boldsymbol{u}_a \ , \tag{4.2.2}$$

which is ‘absolute wind stress”. Throughout, subscripts $\cdot_{abs}$ and $\cdot_{rel}$ imply absolute and relative, respectively. The total wind power input into the geostrophic circulation can be computed as

$$P = \int_S \boldsymbol{\tau} \cdot \boldsymbol{u}_{gs} \, dS \ , \tag{4.2.3}$$

where $\boldsymbol{\tau} \cdot \boldsymbol{u}_{gs}$ is defined as work done by winds on the geostrophic ocean surface, $\int_S$ is the integral over horizontal space, and the subscript $\cdot_{gs}$ denotes geostrophic surface motion. P has units of kg m^2 s^{-3}.

Relative wind stress acts to reduce the total wind power input into large-scale geostrophic motions by $\sim 20-35\%$, ultimately slowing down the ocean circulation (Duhaut and Straub, 2006; Hughes and Wilson, 2008). Relative wind stress is also found to reduce mesoscale eddy kinetic energy by $\sim$ 30% (Seo et al., 2016; Renault et al., 2016b; Oerder et al., 2018). The damping mechanism is illustrated in Fig. 4.2.1 for a circular anticyclonic eddy in geostrophic balance. As a surface wind blows over the eddy, the wind stress becomes modified by the eddy current, producing a larger (smaller) wind stress at the southern (northern) side of the eddy compared with when the eddy current is not considered. Because the wind stress is largest at the southern side and opposes the eddy current, there is more negative wind work than positive. When wind work is integrated over space, total wind power input is negative and energy is removed from the eddy. The result is the same for a geostrophically balanced cyclonic eddy, as the eddy circulation is

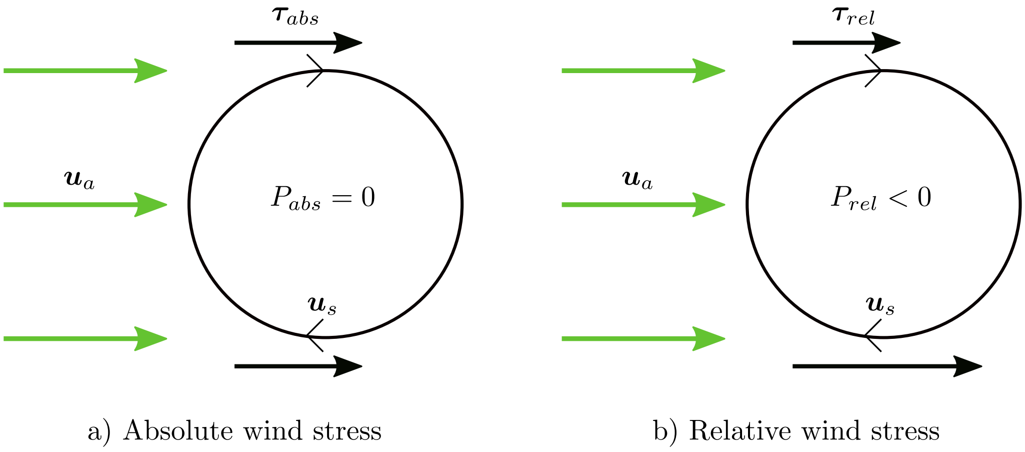

Figure 4.2.1: Schematic depicting changes in wind stress ($\boldsymbol{\tau}$) and wind power input (P) over an isolated anticyclonic eddy. A wind that blows west to east over an eddy will produce a wind stress that generates positive and negative wind work at its northern and southern sides. For an absolute wind stress in a) $\boldsymbol{\tau}_{abs}$ is constant over the eddy, meaning there are equal amounts of positive and negative wind work at each north and south side of the eddy. A sum of total wind work over this eddy gives zero wind power input and no eddy damping. In b) relative wind stress gives more wind stress on the southern side and less on the northern side. The asymmetry in the wind stress produces more negative than positive wind work. Summing over the whole space gives a net negative wind power input, and energy is systematically removed from the eddy.

merely directed in an anticlockwise manner, rather than clockwise.

Relative wind stress damping has other important effects on ocean processes. Through a reduction in ocean current speeds by relative wind stress, numerical simulations displayed improvements in their representation of equatorial currents (Pacanowski, 1987) and western boundary current systems (Ma et al., 2016; Renault et al., 2016a). Without this damping mechanism, however, eddy features in the Agulhas Current are poorly characterised (McClean et al., 2011) and total heat transport in the Southern Ocean is overestimated (Munday et al., 2021).

A further dynamical response of relative wind stress is the production of vertical motions via Ekman pumping, which is found to attenuate eddies by flattening their isopycnals (Dewar and Flierl, 1987). However, relative wind stress-induced Ekman pumping could be a potential route for the supply of energy through baroclinic conversion (Renault et al., 2018). Shan et al. (2020)

show that the conversion of potential into kinetic energy could partially compensate the damping of kinetic energy by relative wind stress. In addition, Ekman pumping due to relative wind stress is also known to play an important role in the supply of nutrients from the deep ocean into the euphotic zone (McGillicuddy et al., 2007; Gaube et al., 2014).

The structure of eddies can also impact their lifetime. For example, the stability of monopole baroclinic eddies is found to decrease with an increase in baroclinic shear, leading to a breakup of the initial vortex structure (Ikeda, 1981). Eddies with strong baroclinic components typically exhibit a deep flow that is counter to its surface rotation, destabilising baroclinic eddies (Dewar and Killworth, 1995). In this counter-rotating setup, upper and lower layer potential vorticity gradients oppose each other, providing a necessary condition for baroclinic instability (Pierrehumbert and Swanson, 1995). Dewar et al. (1999) found that eddy stability can be enhanced by a stronger barotropic component, a deep co-rotating flow, implying a reduction of opposing potential vorticity gradients between upper and lower layers. In a linear stability analysis, Katsman et al. (2003) reveal growth rates of the most unstable azimuthal modes are drastically reduced when the vertical eddy structure transitioned from counter- to co-rotating.

This paper aims to examine the role that relative wind stress has on a baroclinic anticyclonic eddy. First, when the eddy is subject to relative wind stress and its associated negative wind power input, does this lead to a complete eddy spin-down? Second, can Ekman pumping generate additional kinetic energy through baroclinic conversion that offsets relative wind stress damping? Finally, how might the stability of a baroclinic counter-rotating eddy be affected by relative wind stress? In section 4.3, descriptions of the model setup and key theoretical techniques are given. In section 4.4, we present our main findings, showing how the eddy responds to each wind stress formula. In section 4.5, we summarise and discuss the results.

4.3 Methods

4.3.1 Experimental setup

The MIT general circulation model (Marshall et al., 1997a) is employed in this study. The model is set in an idealised configuration, whereby a single eddy is allowed to evolve in a box-like domain whilst being forced by a surface wind stress. The idealised approach allows the underlying physics of eddy-wind interactions to be diagnosed.

The eddy sits on an f-plane at a latitude of 40°N and the domain spans 2000 km in each horizontal direction with mesoscale resolving resolution of 10 km. In the vertical, the domain is 4000 m deep and has 91 z-levels with grid spacing of 5 m at the surface and 100 m near the bottom. Generated using Stewart et al. (2017), this vertical grid is designed to ensure that baroclinic modes are correctly resolved in z-coordinate ocean models. At the boundary edges the flow is re-entrant, meaning what leaves the north (east) boundary re-enters through the south (west), and vice versa. A temperature sponge layer of width 100 km is applied at each boundary edge and is restored daily, making sure that any temperature signals propagated from the eddy do not cross the boundary edge and re-enter the domain. At the bottom boundary, a free-slip condition is used along with zero bottom drag. Values of key parameters can be found in Table 4.1.

At the grid scale, energy dissipation and temperature diffusion are parameterised using biharmonic operators. The Prather advection scheme (Prather, 1986) is used in the temperature equation to preserve any sharp frontal structures that might arise in the flow. Moreover, the use of the Prather scheme has been found to reduce levels of spurious diapycnal mixing in high resolution z-coordinate models (Hill et al., 2012). In the vertical, constant viscous and diffusive coefficients are employed, as well as convective adjustment to remove static instability.

Table 4.1: Key model parameters

Symbol	Value	Description
$L_{x,y}$	2000 km	Domain size
H	4000 m	Ocean depth
H_1	800 m	Upper layer ocean depth
$\Delta x, y$	10 km	Horizontal grid resolution
Δz	5 m to 100 m	Vertical grid spacing
f	9.3461×10^{-5} s^{-1}	Coriolis frequency
A	25 cm	Eddy amplitude
R	100 km	Eddy e-folding radius
$\boldsymbol{u}_a$	7 m s^{-1}	Wind speed
T'	2.5 °C	Temperature anomaly
γ, B	1, 3	Governs stratification
ρ_0	1026 kg m^{-3}	Reference ocean density
$\Delta\rho$	3 kg m^{-3}	Density difference between layers
N_0	10^{-5} s^{-1}	Reference buoyancy frequency
A_4	8×10^{10} m^4 s^{-1}	Biharmonic viscous coefficient
A_z	1×10^{-4} m^{2}s^{-1}	Vertical viscous coefficient
κ_4	3.2×10^{9} m^4 s^{-1}	Biharmonic diffusive coefficient
κ_z	4×10^{-5} m^{2}s^{-1}	Vertical diffusive coefficient

Initial eddy conditions are derived from a thermal wind balance and employ a Gaussian function for its sea surface height and horizontal temperature profile (Chelton et al., 2011). The sea surface height is given by

$$\eta(x, y) = Ae^{-(x^2+y^2)/R^2} , \tag{4.3.1}$$

where A is the eddy sea surface amplitude and R is the e-folding radius, which is the point of zero vorticity. Maximum geostrophic velocities occur at $L_s = 2^{-1/2}R$, the speed-based radius (Chelton et al., 2011). The temperature profile is

$$T(x, y, z) = T' e^{-(x^2+y^2)/R^2} e^{-\gamma(z/H_1)} + T_{ref}(z) \;, \tag{4.3.2}$$

where T' is the temperature anomaly, γ governs the stratification of the water column, and H_1 is the effective thermocline depth. Figure 4.3.1a shows a transect of this temperature profile. The use of γ in Eq. (4.3.2) produces a temperature profile that decays with depth, necessary to generate a counter-rotating lower layer. The reference background temperature profile, $T_{ref}(z)$, is found using the linear equation of state, where the reference background density profile is given by

$$\rho_{ref}(z) = \rho_0(1 - N_0^2(z/g)) + 0.5\Delta\rho(1 - \tanh(B(z + H_1)/H)) \;, \tag{4.3.3}$$

where ρ_0 is a reference density, N_0 is a reference buoyancy frequency, g is the gravitational constant, z are vertical grid levels, $\Delta\rho$ is the difference in density between the surface and bottom, B is the gradient of the density profile, and H is the depth of the ocean.

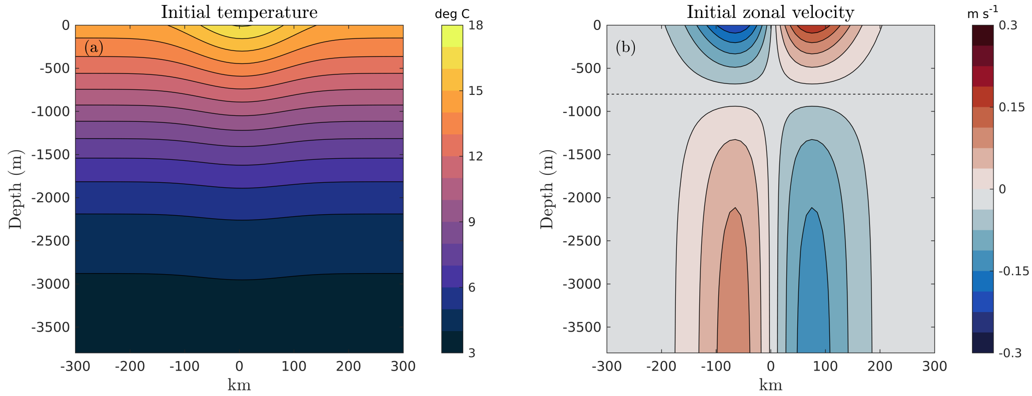

Figure 4.3.1: Meridional transects through the eddy centre of: a) initial temperature (in deg C) and b) zonal velocity (in m s^{-1}). The horizontal dashed line in b) is the depth of the upper layer, $H_1 = 800$ m.

Horizontal velocity components of the eddy are in geostrophic balance

$$\boldsymbol{u}_g(x, y, z) = \frac{g}{f}\boldsymbol{k} \times \left[\nabla\eta + \alpha \int_z^0 \nabla T \, dz\right] \;, \tag{4.3.4}$$

where f is the Coriolis frequency, α is the thermal expansion coefficient, and $\boldsymbol{u}_g = (u_g, v_g)$ are zonal and meridional geostrophic velocity components. The subscript $\cdot_g$ symbolises geostrophic components. The first term in the square brackets is the surface velocity derived from the Gaussian sea surface height, and the second term is the vertical shear derived through thermal wind balance. Figure 4.3.1b displays a transect of initial velocity, with the counter-rotating setup clearly visible.

The wind setup follows McGillicuddy (2015). A spatially uniform background wind begins in the west to east direction and rotates $2\pi/64$ every hour, meaning the wind vectors make one full rotation every 64 hrs. Choosing this rotation period avoids inertial disturbances developing in the eddy shape, and also minimises Ekman transport that could lead to sea level height discontinuities at the boundary edges.

In this analysis, two main simulations are carried out: absolute wind stress (AW); and relative wind stress (RW). An additional simulation with no-wind forcing is run as our control experiment and shows how the eddy evolves on its own. Prior to any analysis, a ten day model adjustment phase is run to allow any waves to die down. After this adjustment, the wind is turned on immediately and each simulation is run for 400 days in total.

4.3.2 Ekman pumping

Total Ekman pumping is defined following Stern (1965)

$$W_{tot} = \frac{1}{\rho_0}\boldsymbol{k}\cdot\nabla\times\left[\frac{\boldsymbol{\tau}}{(f+\zeta_g)}\right], \tag{4.3.5}$$

$$= \underbrace{\frac{\boldsymbol{k}\cdot\nabla\times\boldsymbol{\tau}}{\rho_0(f+\zeta_g)}}_{W_c} + \underbrace{\frac{1}{\rho_0(f+\zeta_g)^2}\left(\tau^x\frac{\partial\zeta_g}{\partial y} - \tau^y\frac{\partial\zeta_g}{\partial x}\right)}_{W_\zeta}, \tag{4.3.6}$$

where ζ_g is the geostrophic relative vorticity, and τ^x and τ^y are zonal and meridional wind stress components, respectively. W_{tot} is calculated using daily time-mean quantities, as is the case for all terms except energetics in section 4.3.3.

Total Ekman pumping, W_{tot}, consists of two components: linear Ekman pumping, W_c - induced by a wind stress curl - and, non-linear Ekman pumping, W_ζ - induced by vorticity gradients. For a uniform background wind, relative wind stress generates a wind stress curl because of its spatial variability over the eddy, whereas absolute wind stress is constant everywhere and no gradients in wind stress will exist (see Fig. 4.2.1). Therefore, only relative wind stress induces linear Ekman pumping, which produces upwelling at the centre of anticyclonic eddies, enabling spin-down through a flattening of isopycnals (Dewar and Flierl, 1987). On the other hand, non-linear Ekman pumping takes place irrespective of the wind stress formula, and will exhibit dipoles of up/down-welling. The primary effect of W_ζ is to advect the eddy by tilting isopycnals (Stern, 1965). Similarly to Gaube et al. (2015), we expect W_c to be the dominant attenuation process in this eddy setup.

4.3.3 Energetics

To understand the eddy spin-down process, we make use of the quasi-geostrophic energetic framework defined by von Storch et al. (2012). In the following definitions, the time-mean refers to a 16 day rolling average, and turbulent terms are perturbations from this mean. The choice of this 16 day time-mean is made to avoid aliasing any unwanted signal that might come from averaging a non-integer multiple of wind rotations i.e. 16 days works out at 6 full wind rotations. Mean energy terms help diagnose the total evolution of the eddy, and are denoted by $\cdot_M$. Turbulent energy terms are useful to examine eddy instability pathways, and are denoted by $\cdot_T$. Conversions between energy reservoirs are symbolised by $C(X, Y)$. For $C(X, Y) > 0$, X is converted to Y, and $C(X, Y) < 0$, Y is converted to X.

Mean potential and mean kinetic energy are described using

$$PE_{_M} = -\int_V \frac{g}{2n_0} \overline{\rho^*(x,y,z,t)}^2 \, dV \ , \quad \text{and} \tag{4.3.7}$$

$$KE_{_M} = \int_V \frac{\rho_0}{2} (\overline{u}_g^2 + \overline{v}_g^2) \, dV \ , \tag{4.3.8}$$

where $\bar{\cdot}$ represents a time-mean, $\rho^*(x,y,z,t) = \rho(x,y,z,t) - \rho_{ref}(z)$ is a density anomaly relative to a constant-in-time reference background density state, n_0 is the vertical gradient of $\rho_{ref}(z)$, from Eq. (4.3.3), and $\int_V$ is the volume integral. Both $PE_{_M}$ and $KE_{_M}$ have units kg m^2 s^{-2}. This quasi-geostrophic framework has been employed in previous energy analyses (Chen et al., 2014; Youngs et al., 2017).

The mean kinetic energy describes the strength of the eddy flow, and its temporal evolution is governed by energy conversions, wind work and viscous dissipation

$$\frac{\partial KE_{_M}}{\partial t} = C(PE_{_M}, KE_{_M}) + P + \epsilon(KE_{_M}) \ , \tag{4.3.9}$$

where,

$$C(PE_{_M}, KE_{_M}) = -\int_V g\overline{\rho}\,\overline{w} \, dV \ , \ \text{and} \tag{4.3.10}$$

$$P = \int_S \overline{\boldsymbol{\tau}} \cdot \overline{\boldsymbol{u}}_{gs} \, dS \ . \tag{4.3.11}$$

In Eq. (4.3.9), divergence and advection terms have been neglected because they do not contribute to the time evolution of domain-integrated $KE_{_M}$. Eq. (4.3.10) describes the conversion between $PE_{_M}$ and $KE_{_M}$, and has units of kg m^2 s^{-3}. When $C(PE_{_M}, KE_{_M}) > 0$, $PE_{_M}$ is transferred to $KE_{_M}$, and this can be thought of as baroclinic conversion. This term is governed by fluxes of density up and down the water column and may be an important term because it could be affected by relative wind stress-induced Ekman pumping. Eq. (4.3.11) is wind power input, also shown in Eq. (4.2.3). In the case of a uniform background wind and relative wind stress, P will dissipate mesoscale eddies (Xu et al., 2016). The last term $\epsilon(KE_{_M})$ is made up of turbulent momentum transfers and viscous processes.

Diagnosing turbulent eddy terms can inform on the presence of eddy instabilities. Turbulent kinetic energy is

$$KE_T = \int_V \frac{\rho_0}{2} \overline{(u_g'^2 + v_g'^2)}\, dV \ , \tag{4.3.12}$$

where $\cdot'$ are fluctuations from their time-mean. KE_T has units of kg m^2 s^{-2}. Conversion terms that transfer turbulent energy in and out of KE_T are given by

$$C(KE_T, KE_M) = \int_V \left(\rho_0 \overline{u_g' \boldsymbol{u'}} \cdot \nabla \overline{u}_g + \rho_0 \overline{v_g' \boldsymbol{u'}} \cdot \nabla \overline{v}_g\right) dV \ , \tag{4.3.13}$$

$$C(PE_T, KE_T) = -\int_V g \overline{\rho' w'}\, dV \ , \tag{4.3.14}$$

where $\boldsymbol{u} = (u_g, v_g, w)$. Equation (4.3.13) is the conversion between turbulent kinetic energy and mean kinetic energy by momentum fluxes. This is the barotropic pathway and barotropic instability takes place when shear in the mean flow produces turbulent kinetic energy, i.e. $C(KE_T, KE_M) < 0$. Equation (4.3.14) is the generation of turbulent kinetic energy from turbulent potential energy by perturbation vertical density fluxes. This is the baroclinic pathway and baroclinic instability occurs when vertical density fluxes restratify the tilted isopycnals, i.e. $C(PE_T, KE_T) > 0$. Equation (4.3.13) and (4.3.14) have units kg m^2 s^{-3}. A full derivation of these energetic terms can be found in von Storch et al. (2012) and Chen et al. (2014), so we will not cover them here.

4.3.4 Potential vorticity

Potential vorticity is used here to diagnose changes in the stability of the anticyclonic eddy from relative wind stress. Following Hoskins et al. (1985), potential vorticity, Q, is defined as

$$Q = (f + \zeta_g)\partial_z b - (\partial_z v_g)(\partial_x b) + (\partial_z u_g)(\partial_y b) \ , \tag{4.3.15}$$

where $b = -g\rho/\rho_0$ is the buoyancy. A necessary condition for the growth of eddy instabilities is the existence of a sign change in radial potential vorticity gradient ($\partial_r Q$) in either the radial or vertical direction (Vallis, 2006). When $\partial_r Q$ changes sign in the horizontal it indicates barotropic instabilities, and when the sign of $\partial_r Q$ varies in the vertical, this indicates baroclinic instabilities. In the counter-rotating eddy setup, $\partial_r Q$ changes sign in the vertical and it is thus baroclinically unstable (Dewar et al., 1999).

4.4 Results

4.4.1 Wind-induced vertical motions

Normalised relative vorticity, ζ_g/f, non-linear Ekman pumping, W_ζ, and vertical velocity, w, are displayed in Fig. 4.4.1 for the absolute wind stress simulation (AW). W_ζ in this case accounts for total Ekman pumping. These quantities are plotted using daily time-mean model output at day 100, and show the eddy approximately mid way through its lifetime. ζ_g/f maintains a circular symmetric profile with strong anticyclonic vorticity at its centre and weak cyclonic vorticity at its periphery (Fig. 4.4.1a). W_ζ displays a dipole pattern of upwelling and downwelling at the eddy centre (Fig. 4.4.1b), generated through the interaction of constant $\boldsymbol{\tau}_{abs}$ and horizontal relative vorticity gradients. The dipole orientation is also dependent on the direction of the wind. w is shown at a depth of 5 m (Fig. 4.4.1c), the first z-layer below the surface. The pattern of w is similar to W_ζ in its shape and magnitude. W_ζ reaches 0.065 m day^{-1} whilst w exhibits values over 0.1 m day^{-1}. In w, a spiral arm can be seen at the outer edge of each dipole, pointing to a possible growth of azimuthal wavenumber $l = 2$ in the counter-rotating eddy setup (Katsman et al., 2003). Plotting w at 5 m depth is done because W_ζ is valid at the base of the Ekman layer. The depth of the Ekman layer is defined using $\delta_E = \sqrt{(2A_z)/f}$ (Vallis, 2006), and gives, $\delta_E \approx 1.5$ m.

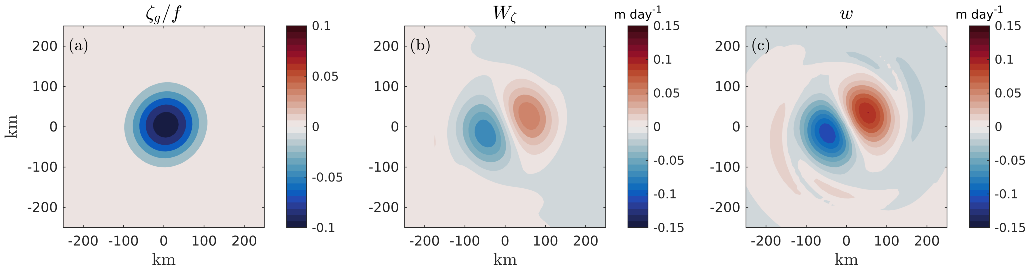

Figure 4.4.1: Horizontal patterns at day 100 in absolute wind stress simulation of: a) surface normalised relative vorticity, b) non-linear Ekman pumping (in m day^{-1}), and c) model output vertical velocity (in m day^{-1}) at a depth of 5 m. Quantities are calculated using MITgcm daily time-mean output.

In the relative wind stress simulation (RW), additional quantities are presented in Fig. 4.4.2, showing relative wind stress curl, $\nabla \times \boldsymbol{\tau}_{rel}$, linear Ekman pumping, W_c, and total Ekman pumping, W_{tot}. At day 100, an eddy weakening can first be observed in RW by looking at the plan views of ζ_g/f (Figs. 4.4.1a and 4.4.2a). Anticyclonic vorticity in RW is weaker than AW as can be seen by the reduction in contour saturation at the eddy centre. This damping of relative vorticity is due to the imposed relative wind stress curl that injects oppositely signed vorticity into the eddy (Fig. 4.4.2b). Like AW, RW has a dipole pattern in W_ζ, but more downwelling takes place (Fig. 4.4.2d) due to $\boldsymbol{\tau}_{rel}$ introducing asymmetry. Additionally, W_ζ is overall weaker than AW, with values around 0.058 m day^{-1}, consistent with the damping of ζ_g/f. W_c (Fig. 4.4.2e) is generated via the wind stress curl, displaying a monopole of upwelling (0.12 m day^{-1}) surrounded by weak downwelling (0.02 m day^{-1}), attenuating the eddy by flattening its isopycnals. W_{tot} has even stronger central upwelling (0.14 m day^{-1}) and is clearly dominated by the upwelling nature of W_c (Fig. 4.4.2f). As with AW, w (Fig. 4.4.2c) has similar patterns to W_{tot} but is greater in value as it is deeper than $\delta_E \approx 1.5$ m. Gaube et al. (2015) and Chen et al. (2020) also found similar Ekman pumping patterns to the ones shown here.

Further examination of the eddy vertical velocity field is made in Fig. 4.4.3. Away from the eddy surface, horizontal patterns of vertical velocity take on a different shape. Fig. 4.4.3a,b show w at day 100 averaged over the top 800 m for absolute and relative wind stress simulations. The w field exhibits alternating

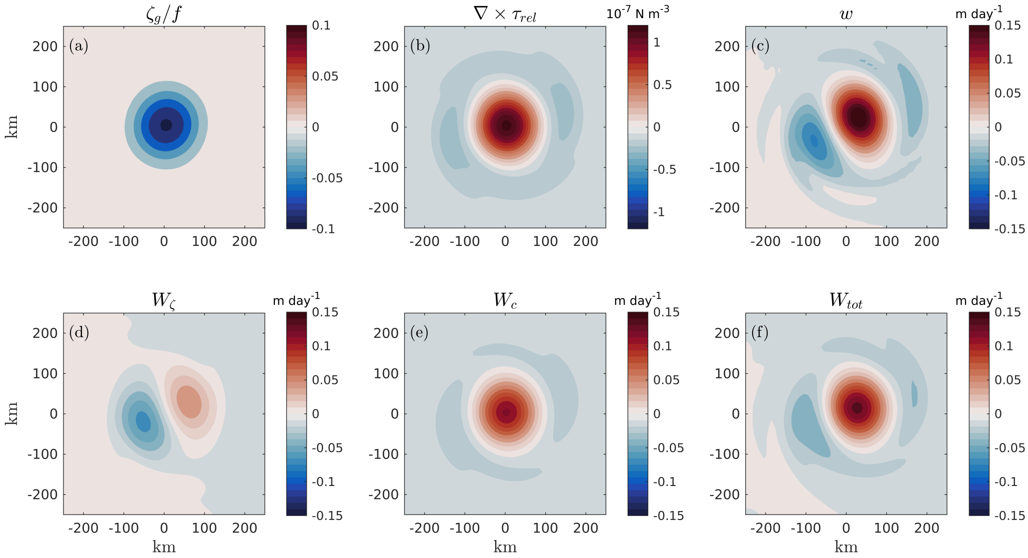

Figure 4.4.2: Horizontal patterns at day 100 in relative wind stress simulation of: a) surface normalised relative vorticity, b) relative wind stress curl, c) model output vertical velocity (in m day^{-1}) at a depth of 5 m, d) non-linear Ekman pumping (in m day^{-1}), e) linear Ekman pumping (in m day^{-1}), and f) total Ekman pumping (in m day^{-1}). Quantities are calculated using MITgcm daily time-mean output.

up/down-welling cells that encircle the eddy centre, which indicate the eddy is not in geostrophic balance (Pilo et al., 2018). The w field is dominated mostly by a four cell pattern, but also exhibits a weaker eight cell pattern towards the periphery. The four cell vertical velocity pattern is similar to the pattern of a linearly unstable vortex with azimuthal wavenumber $l = 2$ seen in Fig. 2 of Dewar et al. (1999), whilst the eight cell pattern may indicate the existence of unstable higher wavenumbers. Nevertheless, the net effect of relative wind stress on values of w still remain. w_{rel} has maximum absolute values up to 0.03 m day^{-1} greater than w_{abs}.

Transects of w show the extension of vertical motions down the water column (Fig. 4.4.3c,d). w_{abs} exhibits a dipole of up/down-welling at the surface, but with depth the modal wave pattern becomes greater than any Ekman pumping effects. Similarly, w_{rel} shows an Ekman pumping pattern at the surface, as seen in Fig. 4.4.2c,f, but again the modal wave pattern quickly exerts its dominance with depth. The overall increase in w is also visible in Fig. 4.4.3e from the surface down to 3000 m. This implies that, although the spatial pattern of w changes with depth, the impact of relative wind stress on vertical velocity remains throughout the water column.

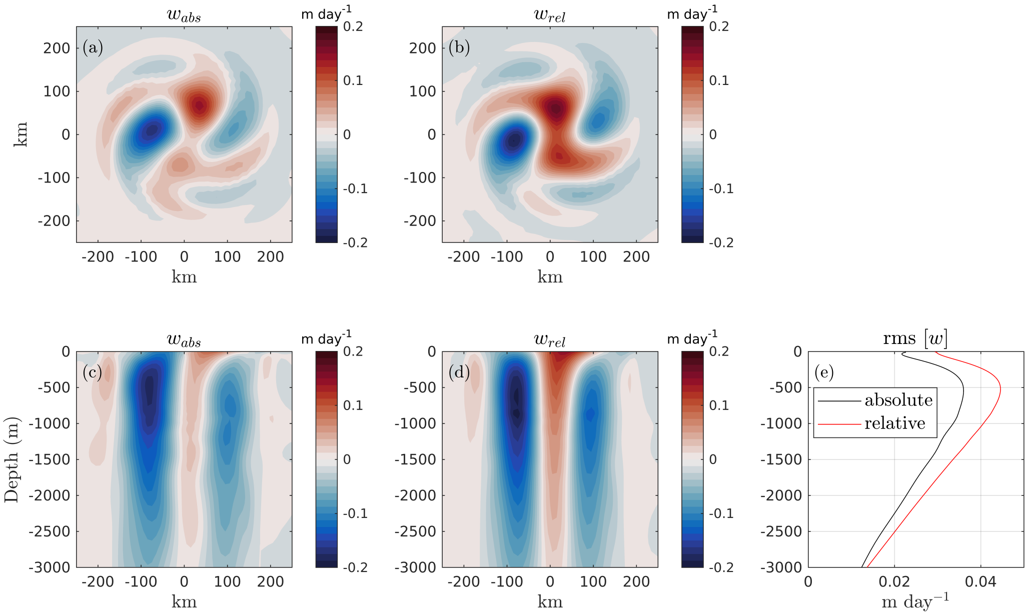

Figure 4.4.3: Model vertical velocity output at day 100 (in m day^{-1}). Horizontal patterns averaged over top 800 m for a) absolute wind stress and b) relative wind stress, and zonal transects through eddy centre for c) absolute wind stress and d) relative wind stress. In e) the root-mean-square of vertical velocity for absolute (black) and relative (red) wind stress simulations. Quantities are calculated using MITgcm daily time-mean output.

4.4.2 Mean eddy energetics

Damping and dissipation

The work done by wind on the eddy's geostrophic surface motion at day 100 is shown in Fig. 4.4.4. Here, the daily model output is used to calculate wind work as a snapshot in time. Dipoles of positive and negative wind work exist in absolute (Fig. 4.4.4a) and relative (Fig. 4.4.4b) wind stress simulations. Maximum values of wind work occur in regions of the eddy that have the strongest surface current, which is at the speed-based radius, $L_s \approx 70$ km. In AW, the amount of negative wind work is negated by positive wind work, since there is no current-wind interaction in $\boldsymbol{\tau}_{abs}$, Eq. (4.2.2). In RW, in absolute terms, there is around 12% more negative than positive wind work due to the current-wind interaction in $\boldsymbol{\tau}_{rel}$, Eq. (4.2.1), seen through the zonal cross section of wind work (Fig. 4.4.4c). The total wind power input by relative wind stress is seen over time in Fig. 4.4.5c, and highlights the amount of power being removed from the anticyclonic eddy.

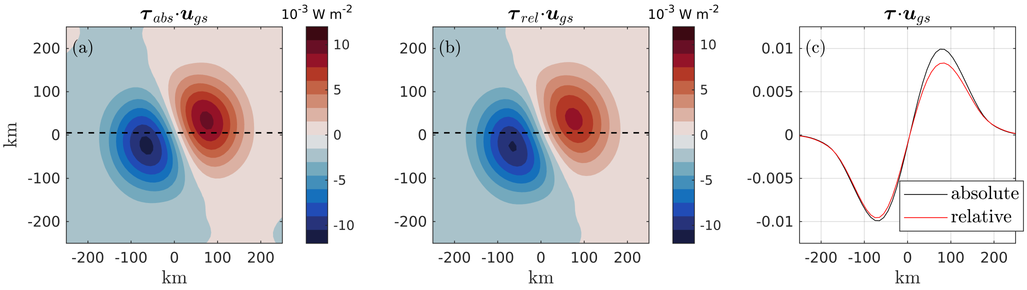

Figure 4.4.4: Horizontal patterns at day 100 of wind work done on the eddy's geostrophic motion (in 10^{-3} W m^{-2}), for a) absolute wind stress and b) relative wind stress simulations. In c) zonal cross sections - dashed lines in (a) and (b) - of wind work in absolute (black line) and relative (red line) wind stress simulations. Quantities are calculated using MITgcm daily time-mean output.

The time evolution of domain integrated mean eddy energetics is shown in Fig. 4.4.5. Total eddy energy ($KE_M + PE_M$) is dominated by PE_M, where KE_M is around an order of magnitude smaller for the first 150 days of the time-series (Fig. 4.4.5a,b). Dissipation of total energy in RW is larger than AW as a result of work done by relative wind stress (Fig. 4.4.4b and 4.4.5c), as shown by the more rapid decrease of $KE_M + PE_M$. The overall damping of total energy likely reflects a release of PE_M, which relative wind stress is the most efficient at fulfilling, achieving an additional 7×10^{14} J of dissipation at day 200. Although the wind power input by relative wind stress is negative (Fig. 4.4.5c) and consistent with the decay of total eddy energy, it does not explain in full how PE_M is reduced.

From Eq. (4.3.9) there are two important terms that govern mean kinetic energy: $C(PE_M, KE_M)$ and P. P_{rel} in this case is negative (Fig. 4.4.5c) and therefore extracts KE_M from the eddy. The exponential growth in magnitude seen in P_{rel} is associated with the exponential growth in KE_M (Fig. 4.4.5b) as P_{rel} depends on the ocean surface current speed. $C(PE_M, KE_M)$ is positive for all time in each simulation (Fig. 4.4.5d) and implies PE_M is converted to KE_M. In RW, $C(PE_M, KE_M)$ is greater for most of time and undergoes an earlier exponential

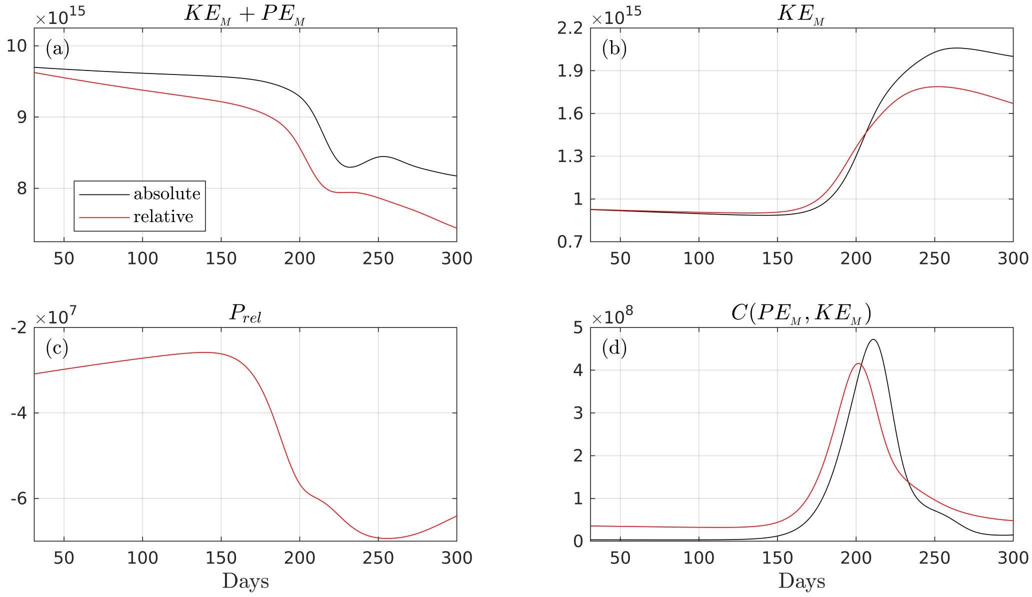

Figure 4.4.5: Time-series from day 31 to 300 comparing absolute (black) and relative (red) wind stress simulations of: a) total mean energy, b) mean kinetic energy, c) relative wind stress damping, and d) conversion of mean potential to mean kinetic energy. Terms in a,b,d) are volume integrals, and c) is a spatial integral. Each day represents a 16-day time-mean. Units of energy in J and damping/conversion in W.

growth and decay. The growth of $C(PE_M, KE_M)$ in-part explains the increased reduction in total energy (Fig. 4.4.5a) since PE_M has to be converted into KE_M before being mechanically dissipated by P_{rel}, or other viscous processes. However, the growth and decay of KE_M in each simulation (Fig. 4.4.5b) appears to be governed by $C(PE_M, KE_M)$, even in RW with P_{rel}. Taking a closer look at values of $C(PE_M, KE_M)$ and P_{rel} in Fig. 4.4.5c,d. At day 31 in the time-series, $C(PE_M, KE_M)$ is $\sim 3.4 \times 10^6$ W in AW and 3.6×10^7 W in RW, whilst P_{rel} in RW is $\sim -3.1 \times 10^7$ W. The additional $C(PE_M, KE_M)$ produced in RW counteracts P_{rel} and increases the KE_M supply by $\sim 1.5\times10^6$ W. By day 100, this KE_M supply has grown to $\sim 2 \times 10^6$ W. This counteracting process by relative wind stress-induced $C(PE_M, KE_M)$ continues until the exponential growth in RW begins to die down.

The effect of relative wind stress on mean kinetic energy and baroclinic conversion is further explored by decomposing their volume contributions into upper and lower layers (Fig. 4.4.6). The upper layer is calculated using all z-levels above and including 800 m, and the lower layer represents that below. As expected, relative wind stress damps upper mean kinetic energy by around 20% from day 31 up until its exponential growth near to day 150 (Fig. 4.4.6a). This damping of surface mean kinetic energy is similar to findings by Seo et al. (2016) and Oerder et al. (2018). It is also clear from this exponential growth in upper layer KE_M why P_{rel} grows (Fig. 4.4.5c). In contrast, lower layer mean kinetic energy has increased by 3% over the same period as a result of relative wind stress (Fig. 4.4.6b). It can be seen that relative wind stress produces more baroclinic conversion in both layers, showing a deep reaching effect from this surface drag (Fig. 4.4.6c,d). In each case, the additional baroclinic conversion is consistent with the larger rms[w] in RW (Fig. 4.4.3e). It therefore appears that additional lower layer baroclinic conversion helps to offset any surface damping.

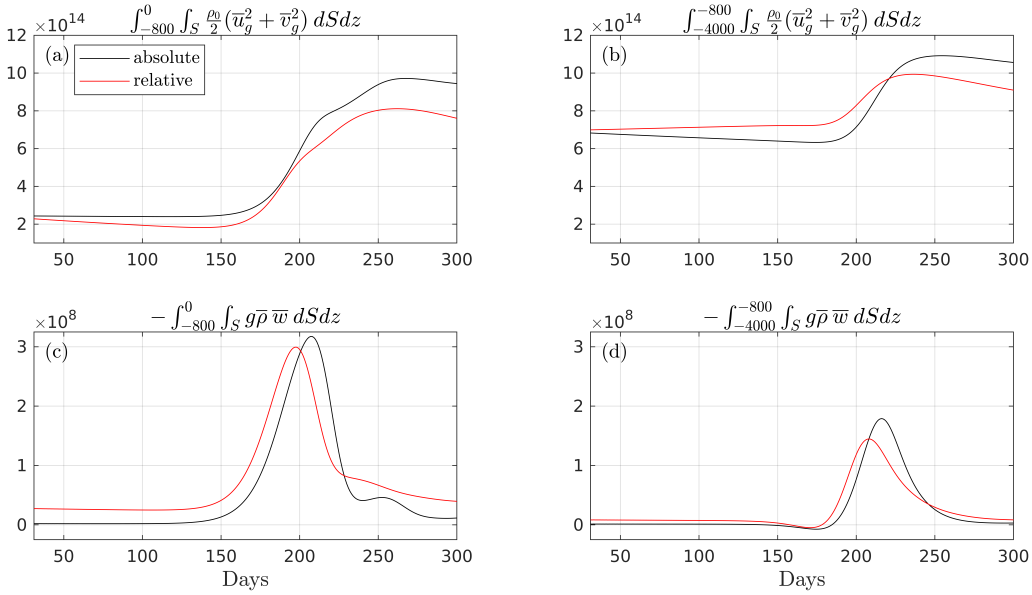

Figure 4.4.6: Time-series from day 31 to 300 comparing absolute (black) and relative (red) wind stress simulations of: a) upper layer mean kinetic energy, b) lower layer mean kinetic energy, c) upper layer conversion of mean potential to mean kinetic energy, and d) lower layer conversion of mean potential to mean kinetic energy. Terms are volume integrated over upper (0 to −800 m) and lower (−800 m to −4000 m) layers. Each day represents a 16-day time-mean. Units of energy in J and conversion in W.

A scaling argument

To provide insight into why additional production of KE_{M} in RW appears to offset wind damping by relative wind stress, we seek a scaling between $C(PE_{M}, KE_{M})$ and P_{rel}. In order to account for deviations in density caused by the eddy, $\overline{\rho}$ needs to be replaced in Eq. (4.3.10). Using von Storch et al. (2012)

$$\int_V \overline{\rho}\,\overline{w}\,dV = \int_V (\overline{\rho} - \rho_{ref})\overline{w}\,dV = \int_V \overline{\rho^*}\,\overline{w}\,dV\ . \tag{4.4.1}$$

This is true because $\int_V \rho_{ref}\overline{w}\,dV = 0$ as the volume integral of $\overline{w}$ will be zero with no-normal flow boundary conditions. Therefore, $\overline{\rho^*}$ replaces $\overline{\rho}$ in Eq. 4.3.10 for this scaling analysis.

Next, additional vertical velocities are generated by relative wind stress-induced Ekman pumping, and it is known that linear Ekman pumping attenuates eddies (Dewar and Flierl, 1987; Gaube et al., 2015). We note that a no-wind experiment (not shown) has similar mean energetics to AW, revealing that W_ζ has little effect on $C(PE_{M}, KE_{M})$. Therefore, W_ζ is neglected from this scaling, and $\overline{w}$ is replaced by W_c in Eq. (4.3.10), thus

$$C(PE_{M}, KE_{M}) = -Hg\overline{\rho^*}\,W_c L_e^2\ , \tag{4.4.2}$$

where L_e is an eddy length scale. To complete this scaling we now need expressions for relative wind stress, wind power input by relative wind stress, and linear Ekman pumping.

Following Duhaut and Straub (2006), we find $\boldsymbol{\tau}_{diff}$ and P_{diff} that equate to relative minus absolute components. In each case, these will provide the contributions that come entirely from eddy-wind interaction. So, P_{diff} is essentially the amount of energy relative wind stress will take out, meaning $P_{diff} \sim P_{rel}$. To find $\boldsymbol{\tau}_{diff}$, it is assumed that only winds aligned with the eddy current contribute to the wind speed magnitude

$$|\boldsymbol{u}_a - \boldsymbol{u}_{gs}| \approx |\boldsymbol{u}_a| - \boldsymbol{u}_{gs} \cdot \boldsymbol{i} \ , \tag{4.4.3}$$

where $\boldsymbol{i}$ is a unit vector that points in the direction of $\boldsymbol{u}_a$. Using this assumption, along with Eqs. (4.2.1) and (4.2.2)

$$\boldsymbol{\tau}_{diff} \equiv \boldsymbol{\tau}_{rel} - \boldsymbol{\tau}_{abs} \approx \rho_a C_d \big[- |\boldsymbol{u}_a| \boldsymbol{u}_{gs} - (\boldsymbol{u}_{gs} \cdot \boldsymbol{i}) \boldsymbol{u}_a \big] \approx -2\rho_a C_d \boldsymbol{u}_a \boldsymbol{u}_{gs} \ , \tag{4.4.4}$$

where quadratic terms have been neglected, and $\boldsymbol{u}_a > 0$. Similarly,

$$P_{diff} \equiv \int_S \boldsymbol{\tau}_{diff} \cdot \boldsymbol{u}_{gs} \, dS \approx -2\rho_a C_d \boldsymbol{u}_a \boldsymbol{u}_{gs}^2 L_e^2 \ . \tag{4.4.5}$$

Now, substituting Eq. (4.4.4) into Eq. (4.3.6) and neglecting the non-linear component W_ζ gives

$$\hat{W}_c = \frac{\nabla \times \boldsymbol{\tau}_{diff}}{\rho_0 (f + \zeta_g)} \approx -\frac{2\rho_a C_d \boldsymbol{u}_a}{\rho_0 f} \zeta_g \ , \tag{4.4.6}$$

where $\hat{W}_c$ neglects the vorticity in the denominator, since $\zeta_g \ll f$. Equation (4.4.6) implies that $\hat{W}_c$ generates upwelling (downwelling) in anticyclonic (cyclonic) regions. Finally, taking Eqs. (4.4.2), (4.4.5) and (4.4.6), and assembling the scaling gives

$$\frac{C(PE_{\scriptscriptstyle M}, KE_{\scriptscriptstyle M})}{P_{rel}} \sim \frac{Hg\overline{\rho^*}\zeta_g}{\rho_0 f \boldsymbol{u}_{gs}^2} \ . \tag{4.4.7}$$

Based on parameters in the anticyclonic eddy, we put $\overline{\rho^*}/\rho_0 \sim 10^{-4}$, $\zeta_g \sim 10^{-6}$ s^{-1}, $\boldsymbol{u}_{gs}^2 \sim 10^{-2}$ m^2 s^{-2}, and values from Table 4.1 into Eq. (4.4.7). These values give a scaling ratio equivalent to 4, showing that additional production of $KE_{\scriptscriptstyle M}$ by W_c offsets damping by relative wind stress. This also supports our numerical findings found earlier in section 4.4.2.

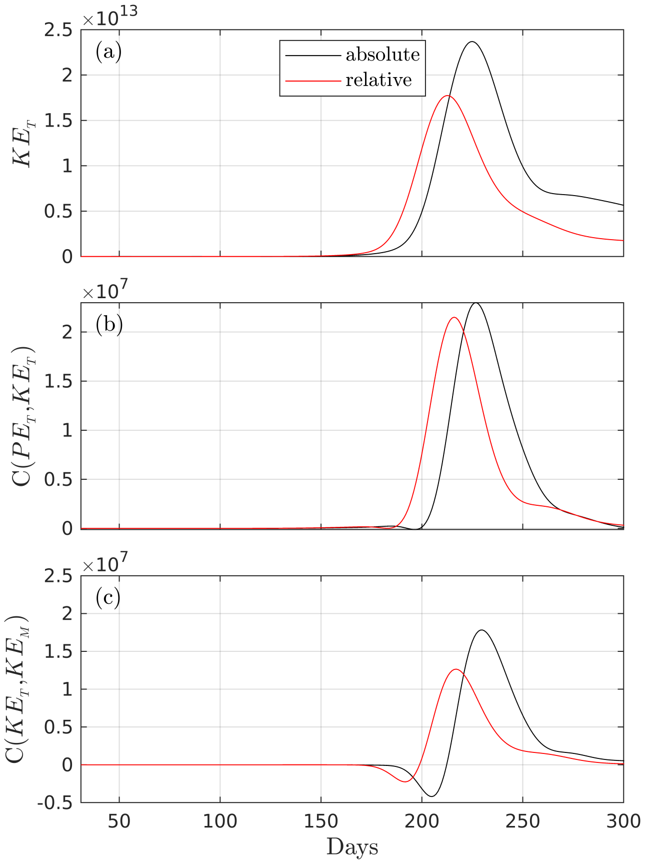

Figure 4.4.7: Time-series from day 31 to day 300 comparing absolute (black) and relative (red) wind stress simulations of: a) turbulent kinetic energy, b) baroclinic pathway, c) barotropic pathway. Terms are volume integrated and each day represents a 16-day time-mean. Units of energy in J and instability pathways in W.

4.4.3 Destabilisation of the eddy

The destabilisation of the eddy is first examined using volume integrated turbulent eddy energetics, shown in Fig. 4.4.7. Initially, little growth is observed in all terms, consistent with the stable time evolution of KE_M and $C(PE_M, KE_M)$ (Fig. 4.4.5b,d). Around day 175, growth in terms begin, indicating the start of eddy instabilities. The dominant instability is baroclinic, with $C(PE_T, KE_T) > 0$ supplying KE_T (Fig. 4.4.7a,b). The barotropic pathway $C(KE_T, KE_M)$ is equivalent in magnitude to the baroclinic one, though fluxes of momentum are predominantly directed upgradient i.e. KE_T is converted to KE_M (Fig. 4.4.7c). The vertical shear component of $C(KE_T, KE_M)$ is negligible. Indeed, Katsman et al. (2003) found the dominant instability to be baroclinic in a counter-rotating eddy regime. It can also be seen that the turbulent peaks all take place shortly after (~ 10 days) the mean energetic peaks (Fig. 4.4.5b,d), indicating that instabilities are prevalent during the eddy's decay stage. A few differences between wind stress simulations exist. The first one is the time of growth, where RW undergoes its amplification ~ 10 days earlier. Secondly, although RW becomes unstable sooner, AW exhibits greater maximum peaks for all quantities, in particular, KE_T is ~ 30% larger than RW. This implies that relative wind stress initiates instabilities sooner but also damps their overall magnitude. Furthermore, growth across all terms comes from the upper 800 m, with turbulent energetic values in the lower layer at least an order of magnitude smaller (not shown). This is consistent with the eddy's primarily surface intensified nature.

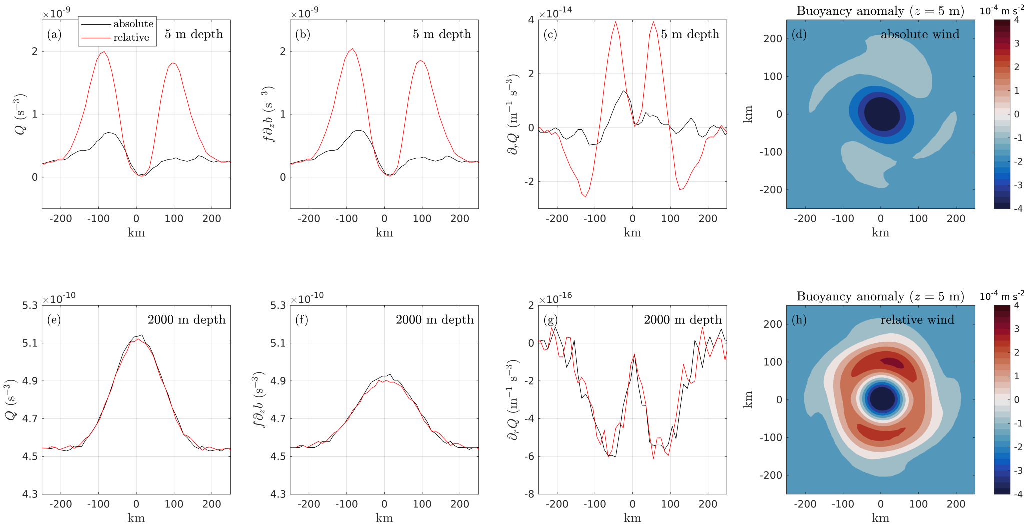

Figure 4.4.8: Meridional cross sections at day 100 at the surface (5 m) and mid-depth (2000 m) of: a,e) potential vorticity (10^{-9} s^{-3}), b,f) potential vorticity contribution by vertical buoyancy gradient (10^{-9} s^{-3}), and c,g) radial potential vorticity gradient (10^{-14} m^{-1} s^{-3}), comparing absolute (black) and relative (red) wind stress simulations. Horizontal plan views of buoyancy anomaly $b(\text{day} = 100) - b(\text{day} = 1)$ (10^{-4} m s^{-2}), at surface (5 m) for d) absolute and h) relative wind stress simulations. Quantities are calculated using MITgcm daily time-mean output.

A reason for this earlier instability onset can be attributed to changes in the eddy's PV gradient between the upper and lower layers, shown in Fig. 4.4.8 for quantities at day 100. It can be seen through cross sections of PV gradients at the eddy surface that values in RW near to a radius of 50 km increase by factors of 4-8 in response to relative wind stress (Fig. 4.4.8c). This increase in PV gradient may be the cause of an earlier onset of baroclinic instability in the eddy (Fig. 4.4.7b). Modifications to the surface PV gradient can be seen by considering the contributions to PV in Eq. (4.3.15). The dominant component of PV is $(f + \zeta_g)\partial_z b$, and we know that $\zeta_g \ll f$. A cross section of $f\partial_z b$ at the surface (Fig. 4.4.8b) is shown to match PV (Fig. 4.4.8a), displaying a similar increase in value in RW. The cross sections at 2000 m depth (Fig. 4.4.8e,f,g) are smaller than the surface quantities and do not vary between wind stress simulations, likely due to $\zeta_g \ll f$ and weak lower layer stratification (see Fig. 4.3.1a). We explain the increase in $f\partial_z b$ through surface buoyancy anomalies at day 100 (Fig. 4.4.8d,h). Through the action of linear Ekman pumping, it can be seen in RW that buoyancy is lost (gained) at the eddy centre (periphery) through upwelling (downwelling). The Ekman pumping process flattens isopycnals, and by doing so converts horizontal density gradients into vertical density gradients, thus increasing $f\partial_z b$ at the surface. This leads to larger PV and PV gradients at the surface in RW, as well as the earlier growth in turbulent energetics (Fig. 4.4.7).

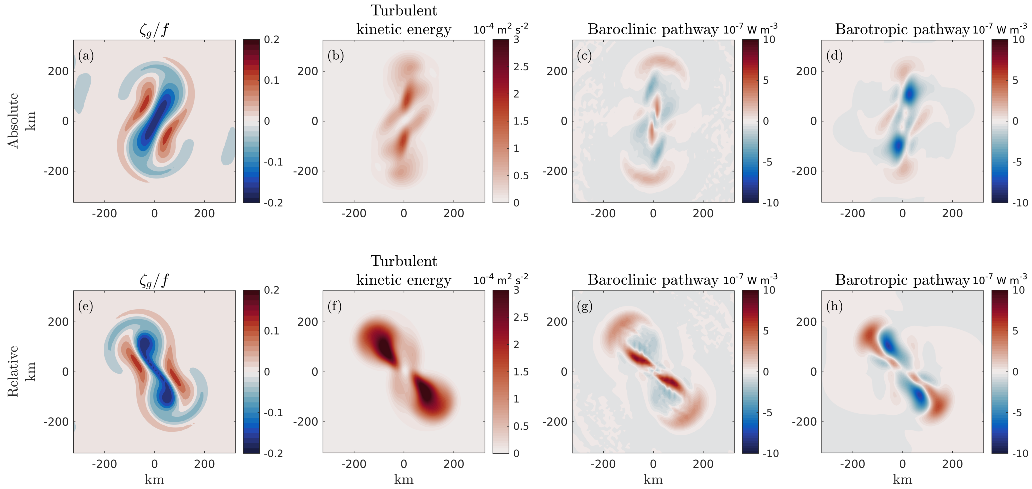

Figure 4.4.9: Horizontal patterns at day 200 of a,e) surface normalised relative vorticity, then profiles averaged over top 800 m of: b,f) $\frac{1}{2}\overline{(u_g'^2 + v_g'^2)}$ (in 10^{-4} m^2 s^{-2}), c,g) $-g\overline{\rho' w'}$ (in 10^{-7} W m^{-3}) and d,h) $\rho_0 \overline{u_g' \boldsymbol{u'}} \cdot \nabla \overline{u}_g + \rho_0 \overline{v_g' \boldsymbol{u'}} \cdot \nabla \overline{v}_g$ (in 10^{-7} W m^{-3}). Top is absolute wind stress and bottom is relative wind stress. Relative vorticity is calculated using MITgcm daily time-mean output, and energetic terms are 16 day time-means taken at day 200.

Horizontal plan views of surface ζ_g/f, and turbulent kinetic energy, baroclinic pathway, and barotropic pathway averaged over the top 800 m at day 200 are presented in Fig. 4.4.9. Again, ζ_g/f uses daily mean model output, and energetic terms use a 16 day time-mean at day 200. The choice of day 200 is used to illustrate the spatial inhomogeneity of these perturbations prior to the eddy's breakup in each wind stress simulation. In AW, ζ_g/f (Fig. 4.4.9a) displays two spiral arms at the north and south side of the eddy, a feature that was first observed and noted in section 4.3.2 through Ekman pumping patterns. There is a clear elliptical tripole vorticity pattern with anticyclonic vorticity at the centre, much different to the circular profile at day 100 (Fig. 4.4.1a). In general, this elliptical pattern is found to be typical of an unstable azimuthal wavenumber $l = 2$ in a baroclinic eddy (Baey and Carton, 2002). Turbulent kinetic energy and positive baroclinic pathway are concentrated at each spiral arm and between patches of opposing ζ_g/f near the eddy centre, highlighting the instability present in the eddy (Fig. 4.4.9b,c). Values in the barotropic pathway are similar to the baroclinic one, but show a tendency for barotropic instability (Fig. 4.4.9d), which is also seen through the volume integrated terms in Fig. 4.4.7c. In RW, each quantity (Fig. 4.4.9e,f,g,h) displays a slow down in azimuthal rotation in response to the damping of upper layer mean kinetic energy (Fig. 4.4.6a). The ζ_g/f profile has become narrower and the stronger north-south anticyclonic regions have initiated their detachment at the origin. Moreover, turbulent kinetic energy and the baroclinic and barotropic pathways are all much stronger than AW, supporting an earlier destabilisation, and ultimate breakup, due to relative wind stress.

4.5 Summary and discussion

Results from this paper highlight the dynamical response of an anticyclonic baroclinic eddy when forced by an absolute or relative wind stress. Rather than examining an eddy through its entire life cycle (i.e. generation to dissipation), a geostrophically balanced eddy was initialised in a mesoscale resolving numerical model to enable the investigation of its spin-down process. The relevant mechanisms involved in the decay of this eddy include its vertical velocity, energetics, and potential vorticity. These processes were examined to help answer the questions posed towards the end of the introduction.

Can relative wind stress lead to a complete eddy spin-down? In this counter-rotating eddy setup, relative wind stress dissipates combined mean potential and mean kinetic energy throughout the simulation, consistent with the notion that relative wind stress is a drag mechanism (Dewar and Flierl, 1987). However, damping of mean kinetic energy by relative wind stress is offset by an additional production of mean kinetic energy via baroclinic conversion. Moreover, examining upper and lower layer mean energetics reveals that relative wind stress damps (energises) upper layer (lower layer) mean kinetic energy. These findings inform us that relative wind stress is more than just a dissipative process, enabling a transfer of mean potential to mean kinetic energy and modulation of the eddy spin-down process.

Can Ekman pumping generate additional baroclinic conversion that offsets relative wind stress damping? The enhanced production of mean kinetic energy by relative wind stress-induced baroclinic conversion is related to the intensified vertical motions. Relative wind stress imposes a curl over the eddy that generates additional vertical velocities throughout the water column via linear Ekman pumping. These additional vertical motions enable an enhanced transfer of mean potential to mean kinetic energy, capable of counteracting relative wind stress damping. This is made clear with the scaling $C(PE_{M}, KE_{M})/P_{rel} > 1$, implying that relative wind stress-induced baroclinic conversion counteracts relative wind stress damping. This shows that Ekman pumping is an important mechanism for kinetic energy supply (Renault et al., 2018), particularly for the deep eddy flow. Studies have shown little difference in large-scale ocean transport or residual meridional overturning circulation between absolute and relative wind stress (Munday and Zhai, 2015; Munday et al., 2021), so it remains unclear what effects an energised deep eddy flow may have. Nevertheless, despite the increase in vertical velocity by relative wind stress, horizontal patterns in each simulation display significant qualitative differences between the surface and at depth. At the surface, Ekman pumping dominates, whilst at depth, alternating patterns of up/down-welling exist.

How might the stability of a baroclinic counter-rotating eddy be affected by relative wind stress? A further key finding of this study reveals that relative wind stress can modify the stability properties of mesoscale eddies. Because opposing potential vorticity gradients in the upper and lower layer stipulate that a counter-rotating eddy will become unstable (Dewar et al., 1999), we demonstrate that an increase in PV gradients at the surface is the reason for an earlier onset of instability and resulting decay seen in the relative wind stress simulation. The mechanism for these enhanced PV gradients is caused by a conversion of horizontal density gradients into vertical gradients via linear Ekman pumping. In-line with findings by Katsman et al. (2003) for counter-rotating eddies, the most unstable perturbation comes in the form of baroclinic instability, which we find to occur on a shorter timescale in the relative wind stress simulation due to larger surface PV gradients.

Overall, these results show clearly the response of an anticyclonic eddy to relative wind stress forcing. However, different model setups and eddies could lead to other outcomes. Sutyrin (2016) found for an anticyclonic eddy that adding a middle layer of uniform potential vorticity reduced the growth of eddy instabilities, hence putting forward a way that eddy lifetime can be prolonged. Arbic and Scott (2008) showed quadratic bottom drag to damp bottom layer kinetic energy, and could therefore play a role in the stabilisation of mesoscale eddies (Dewar et al., 1999). A cyclonic eddy also plays an essential role in the ocean (e.g. Chenillat et al. (2015)), yet one has not been examined here (see chapter 5 for analysis of a cyclonic eddy). We expect an eddy-wind interaction to produce a similar dynamical response in a cyclonic eddy as it does in the anticyclonic eddy. That is, relative wind stress will damp surface mean kinetic energy and also modify surface potential vorticity gradients. It is not clear how relative wind stress would develop any additional responses not seen in the anticyclonic eddy. Yet, an asymmetry in the growth rate of unstable wavenumbers between cyclonic and anticyclonic eddies does exist (Katsman et al., 2003; Mahdinia et al., 2017), and so it could be worth exploring whether relative wind stress impacts this.

In this numerical model setup, horizontal grid spacing of $\Delta x, y = 10$ km is employed, in-part to keep the model computationally inexpensive, but also capable of fully resolving mesoscale processes at the midlatitudes. The literature surrounding submesoscale resolving numerical models [$O(1)$ km] is very much in the limelight at this moment in time (Brannigan et al., 2017; Su et al., 2018; Schubert et al., 2020), and it could be argued a study such as this should be employing as high a resolution as possible. Yet, the lack of any substantial work on idealised mesoscale eddy-wind interaction still persists, and it is therefore critical to understand this because of the ubiquity and importance of mesoscale eddies in the world's ocean. We do, however, acknowledge some possible shortcomings of these results due to this horizontal resolution. It was found in previous work that when horizontal grid spacing is reduced, a marked increase in vertical motions and surface kinetic energy occur (Levy et al., 2001). Because of the horizontal resolution used, the mesoscale eddy studied here could have underrepresented energetics that may have repercussions on lifetime and stability. Yet, coupled with the knowledge of how eddies evolve (e.g. Ikeda (1981); Dewar et al. (1999)), we expect relative wind stress would still generate a similar outcome at a finer resolution e.g. $\Delta x, y = 2$ km.

This study demonstrates a complex interaction between surface winds and a baroclinic anticyclonic eddy in an idealised setting. Much of the individual results over the eddy's lifetime are well understood, and therefore robust. Yet, bringing them together in this study has resulted in a novel finding, whereby relative wind stress, thought to be completely dissipative, in fact may energise the eddy mean flow and reduce eddy stability. Therefore, this advances our understanding of mesoscale air-sea interactions, though future work should focus on added complexity in model design.

4.6 Concluding remarks and aims of next chapter

In this chapter we examined the response of the anticyclonic eddy in detail to ascertain reasons why the prediction method in chapter 3 became invalid after a certain timescale. We showed that the prediction break down was due to the baroclinic eddy containing opposing potential vorticity gradients between the surface and at depth. An earlier break down in the relative wind stress simulation was attributed to enhanced potential vorticity gradients at the surface due to Ekman pumping. We proposed an energy cascade to be the reason for the disparity in KE and SSH decay in chapter 3. We revealed that mean potential energy was converted into mean kinetic energy. This energy conversion was enhanced by relative wind stress through additional vertical motions by wind stress curl induced Ekman pumping (see Table 4.2). The well known relative wind stress damping was counteracted by this energy conversion, resulting in no KE decay, and proposed as the reason for the enhanced decay in RW MIT SSH (see Fig. 3.3.4 in chapter 3). A scaling argument was also presented showing analytically the energy conversion due to wind stress curl induced Ekman pumping can dominate relative wind stress damping. This is a potentially important finding for further development of the prediction method.

The focus of this chapter was on the evolution of a counter-rotating anticyclonic eddy. We suggested in section 4.5 how a cyclonic counter-rotating eddy may differ to the anticyclonic case. We also briefly mentioned in section 4.2 how the growth rate of the most unstable mode in a counter-rotating eddy stabilises

Table 4.2: Eddy energetics at day 31

Term	Absolute	Relative
Baroclinic conversion	3.4×10^6 W	3.6×10^7 W
Wind damping	-	-3.1×10^7 W

when entering a co-rotating regime (Katsman et al., 2003). The next chapter will consider both of these cases, emphasising where their differences lie with the analyses in this chapter.

5

Sensitivity to eddy parameters

This chapter looks at the sensitivity of relative wind stress forcing to two additional eddy setups by modifying some eddy parameters. First, the baroclinic cyclonic eddy outlined in chapter 3 is examined with a focus on the key responses. So far, only baroclinic cyclonic eddy mean energy has been predicted and a brief discussion has been given in chapter 4 and in Wilder et al. (2022) on the likely response to relative wind stress. To this end, mean and turbulent cyclonic eddy energetics are presented, with comparisons made with the anticyclonic case. From these details, inferences on eddy stability will be acquired through timescales in the time-series. Moreover, we will ascertain whether relative wind stress effects are independent of eddy polarity.

Following the cyclonic eddy, we consider how a co-rotating anticyclonic eddy responds to relative wind stress. This is considered because we know mesoscale eddies typically consist of a combination of barotropic and baroclinic vertical modes (Wunsch, 1997). de La Lama et al. (2016) found an alternative vertical structure that reflected sea surface height and may be more appropriate over rough bottom topography where the deep flow is zero. Regions where this might apply could be the Southern Ocean with its intensified surface flow and rough bottom that is the area of leading kinetic energy dissipation in this region (Huang and Xu, 2018). Eddies with surface intensified motion and zero bottom flow are termed co-rotating in the literature, and are found to be much more stable than counter-rotating eddies (Dewar and Killworth, 1995). With this setup, we can further test the sensitivity of relative wind stress damping in relation to it being offset by additional baroclinic conversion. The co-rotating eddy also offers a unique opportunity to establish how an eddy may respond when their stability properties are altered.

5.1 Cyclonic eddy-wind interaction in a counter-rotating regime

We begin with the cyclonic eddy by first looking at mean energetics and the scaling from Wilder et al. (2022), then turbulent energetics, and finally ageostrophic vertical motions.

5.1.1 Results

Mean energetics

The time evolution of total mean energetics is presented in Fig. 5.1.1 for a baroclinic cyclonic eddy (CE). Some of these results were first mentioned in chapter 3, and will be briefly reiterated to present a continuous narrative here. We find that the overall response of the CE is similar to the anticylonic eddy (ACE) described in Wilder et al. (2022) and chapter 4, as shown in Fig. 5.1.1 by comparing the dashed (ACE) and full (CE) lines. Now looking at the cyclonic eddy, over the first 150 days of the time-series, total energy ($KE_M + PE_M$) is found to decay more (Fig. 5.1.1a) in RW as a result of the negative wind power input (Fig. 5.1.1c). Little decay in total energy is observed in AW due to a combination of reduced dissipation and potential energy production by vertical mixing. In fact, CE $KE_M + PE_M$ decays less compared with the ACE for both AW and RW cases, suggesting some production is taking place since both wind power inputs are equivalent. Furthermore, KE_M is found to decay less in RW, because the negative wind power input is offset by

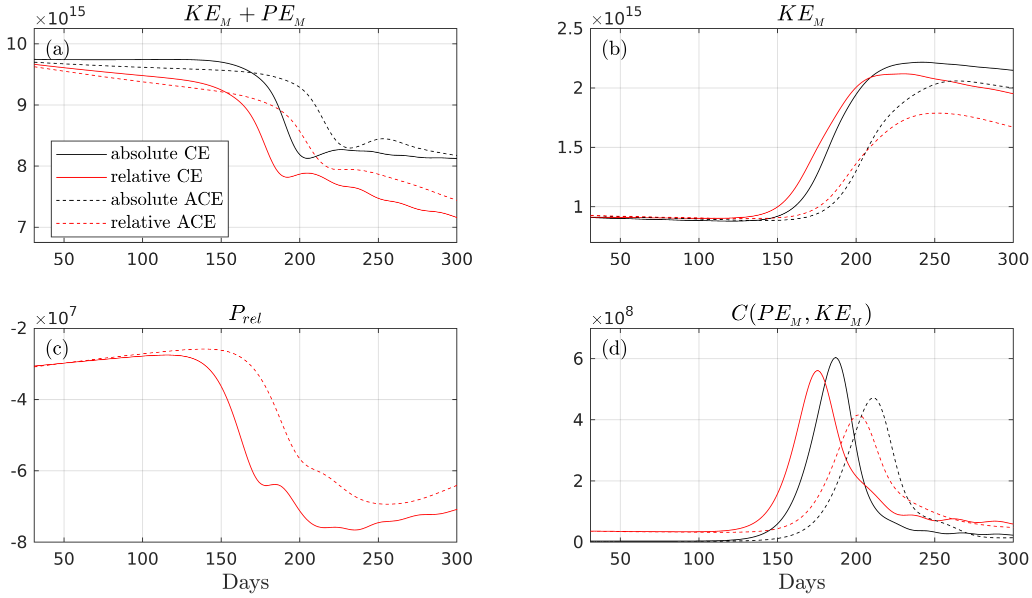

Figure 5.1.1: Time-series from day 31 to 300 comparing absolute (black) and relative (red) wind stress simulations of: a) total mean energy, b) mean kinetic energy, c) relative wind stress damping, and d) conversion of mean potential to mean kinetic energy. Terms in a,b,d) are volume integrals, and c) is a spatial integral. Each day represents a 16-day time-mean. Dashed lines represent the anticyclonic eddy for reference. Units of energy in J and damping/conversion in W.

additional contributions to the term $C(PE_M, KE_M)$ (Fig. 5.1.1d).

Additional baroclinic conversion in the CE is similar to the ACE, which can be understood by considering Wilder et al. (2022). The scaled baroclinic conversion due to linear Ekman pumping is given by

$$C(PE_M, KE_M) = Hg\overline{\rho^*}\left(\frac{2\rho_a C_d \boldsymbol{u}_a}{\rho_0 f}\zeta_g\right)L_e^2\ , \tag{5.1.1}$$

where H is ocean depth, g is gravitational acceleration, $\overline{\rho^*}$ is the density deviation from the reference background state, ρ_a is air density, C_d is a wind stress drag coefficient, $\boldsymbol{u}_a$ is a 10 m surface wind speed, ρ_0 is a reference ocean density, f is the Coriolis parameter, ζ_g is the geostrophic relative vorticity, and L_e is an eddy length scale. If we think of an anticyclonic eddy, $\overline{\rho^*}$ is negative since the isopycnal displacements are depressed from their reference state. Then $C(PE_M, KE_M)$ is positive when ζ_g is also negative. In a cyclonic eddy, the isopycnal displacements are raised above their reference state, and $\overline{\rho^*}$ is positive. Then $C(PE_M, KE_M)$ is positive when ζ_g is also positive. Essentially, the additional positive conversion of mean potential to mean kinetic energy takes place in regions where relative vorticity has the same sign of relative vorticity within the eddy core. This analyses is based on a deduction from Eq. (5.1.1), though it makes physical sense since mean potential energy is released by wind-induced Ekman pumping that acts to flatten eddy isopycnals. This result is also independent of Coriolis parameter since the signs of both ζ_g and f are reversed when entering the Southern Hemisphere i.e. anticyclonic rotation in Northern Hemisphere becomes cyclonic rotation in the Southern Hemisphere.

Moving on from this, the cyclonic eddy undergoes sudden changes in mean energetic values indicating the eddy becoming unstable (Fig. 5.1.1). From day 150, total energy is found to reduce by around 10% over ~ 20 days, with the destabilisation timescale in RW shorter than AW by ~ 10 days. In addition, KE_M grows exponentially for both wind stress formulations and is clearly governed by a strong baroclinic conversion, $C(PE_M, KE_M)$. Like total energy, peaks in KE_M and $C(PE_M, KE_M)$ differ between AW and RW by ~ 10 days, highlighting the earlier trend generated by relative wind stress. Compared with the ACE, a shortened timescale for these sudden changes to take place is observed for all quantities in CE. This suggests an ACE-CE asymmetry exists. Mahdinia et al. (2017) observed this asymmetry in their analysis of eddy modal growth rates, which is consistent with our findings.

Figure 5.1.2 shows volume integrated quantities of upper and lower layer mean kinetic energy and baroclinic conversion for the cyclonic eddy, as well as the anticyclonic eddy for reference. The upper layer takes all z-levels above and including 800 m, and the lower layer is that below. It can be seen that upper layer mean kinetic energy is damped in RW by around 12% from day 31 up to the start of exponential growth at around day 110 (Fig. 5.1.2a). This is less than the amount found in Wilder et al. (2022) for the ACE ($\sim 20\%$), but the reduced damping could be attributed to the shorter timescale, whereby the ACE is damped linearly up to day ~ 150. This surface damping of kinetic energy is consistent with various past studies (Seo et al., 2016; Shan et al., 2020). In lower layer mean kinetic energy, RW displays an increase of around 3% up to day 110, but then the growth slows, possibly due to the sign change in baroclinic conversion (Fig. 5.1.2b,d). The relative wind stress-induced baroclinic conversion in the upper (Fig. 5.1.2c) and lower layers therefore counteracts relative wind stress damping (Fig. 5.1.1c), as reported for the ACE in Wilder et al. (2022).

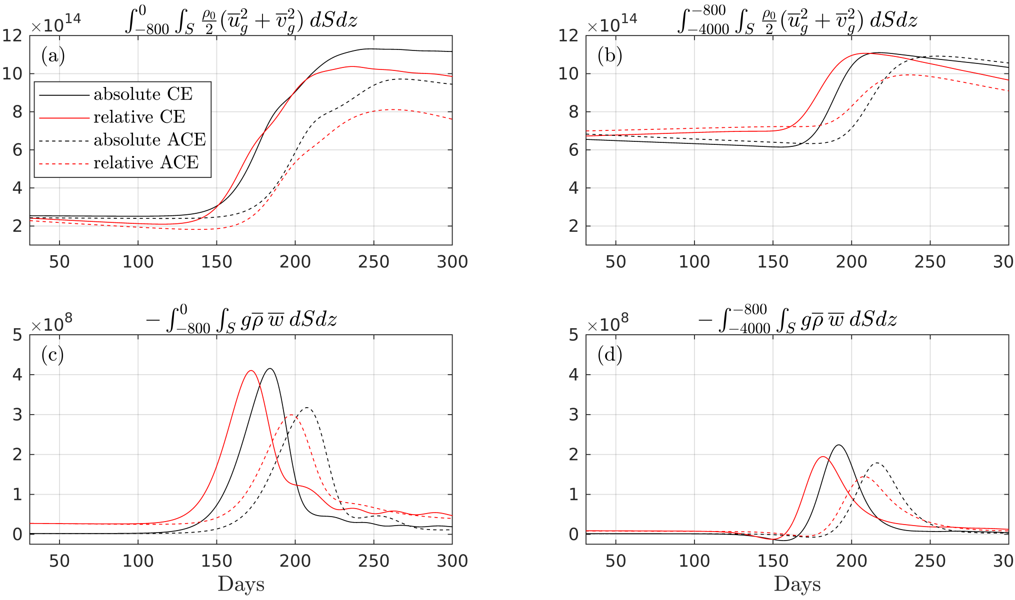

Figure 5.1.2: Time-series from day 31 to 300 comparing absolute (black) and relative (red) wind stress simulations of: a) upper layer mean kinetic energy, b) lower layer mean kinetic energy, c) upper layer conversion of mean potential to mean kinetic energy, and d) lower layer conversion of mean potential to mean kinetic energy. Terms are volume integrated over upper (0 to −800 m) and lower (−800 m to −4000 m) layers. Dashed lines represent the anticyclonic eddy for reference. Each day represents a 16-day time-mean. Units of energy in J and conversion in W.

Turbulent energetics

Instabilities in the eddy are presented through volume integrated turbulent energetics in Fig. 5.1.3. Again, the ACE is included for reference as dashed lines in Fig. 5.1.3a. The difference between the ACE and CE is quite pronounced, whereby quantities in CE undergo rapid changes earlier and are visibly greater, implying the cyclonic eddy is more unstable in nature. Indeed, it was found by Benilov et al. (1998) that anticyclonic eddies display slower growth rates than

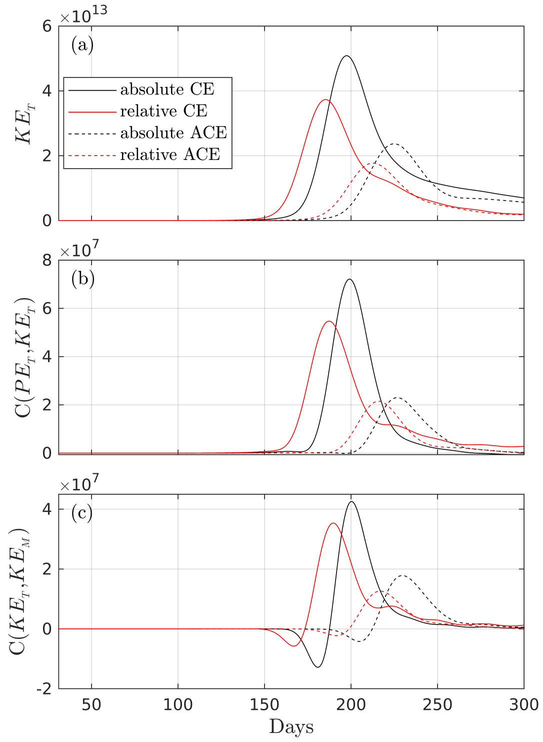

Figure 5.1.3: Time-series from day 31 to day 300 comparing absolute (black) and relative (red) wind stress simulations of: a) turbulent kinetic energy, b) baroclinic pathway, c) barotropic pathway. Dashed lines represent the anticyclonic eddy for reference. Terms are volume integrated and each point represents a 16-day time-mean. Units of energy in J and instability pathways in W.

cyclonic eddies, a possible reason for this disparity in turbulent energetics. Although this additional turbulence may also be due to the reduced surface damping of mean kinetic energy (Fig. 5.1.2a). Now, over the first 150 days, minimal growth is observed across all terms, showing the initial stable nature of the CE. Beyond day 150, a similar response to the ACE then takes place, with exponential like growth in KE_T and $C(PE_T, KE_T)$ (Fig. 5.1.3a,b). This shows the eddy becomes baroclinically unstable over a short period ($\sim$ 30 days). The positive $C(PE_T, KE_T)$ term implies baroclinic instability and governs the growth in KE_T, consistent with the eddy being in a counter-rotating regime (Katsman et al., 2003). Interestingly, relative wind stress invokes a greater damping effect on CE $C(PE_T, KE_T)$. The barotropic pathway is predominantly upgradient (Fig. 5.1.3c), implying that some of the energy supplied to KE_T from $C(PE_T, KE_T)$ goes in to the mean flow through $C(KE_T, KE_M)$.

Horizontal profiles of normalised relative vorticity at the surface, and turbulent energetics averaged over the top 800 m of the eddy are shown in Fig. 5.1.4. In the CE, quantities are plotted at day 175 as they show the eddy entering its breakup stage, and are also approximately at the same stage in growth as the ACE was at day 200. In the absolute wind stress simulation, ζ_g/f displays an elongated tripole of cyclonic vorticity with anticyclonic vorticity at opposing sides and is visibly unstable (Fig. 5.1.4a). Here, the two lobes of turbulent kinetic energy are generated by both baroclinic and barotropic instabilities (Fig. 5.1.4b,c,d). There are also signs of turbulent energy fluxes directing back into the mean flow. In the relative wind stress simulation, again a noticeable change in azimuthal rotation has taken place, likely in response to relative wind stress damping of upper layer mean kinetic energy (Fig. 5.1.2a). Moreover, RW ζ_g/f at the eddy centre is more stretched than AW, showing a more pronounced breakup. Turbulent kinetic energy is much stronger (see Fig. 5.1.3a) and is fuelled by baroclinic and barotropic instability at the eddy centre (Fig. 5.1.4f,g,h). Some of the turbulent kinetic energy supplied by baroclinic instability is converted back to the mean flow through upgradient momentum fluxes. The barotropic pathway is a mixture of up/down-gradient momentum fluxes (Fig. 5.1.4h), meaning this pathway is simultaneously removing and supplying turbulent kinetic energy. However, as a volume integral the barotropic pathway does not make any significant contributions to the overall energy supply at this point in time (Fig. 5.1.3c). The CE is much more unstable compared to the ACE at an earlier time (see Fig. 11 in Wilder et al. (2022)), represented by the $O(10)$ difference in energetic values and the $\sim 50\%$ increase in maximum relative vorticity, in absolute terms.

Ageostrophic vertical motions

It was shown in Wilder et al. (2022) that the anticyclonic eddy exhibited alternating up/down-welling cells in the vertical velocity field w, a characteristic of an unstable azimuthal wavenumber $l = 2$ pattern. Values in the horizontal

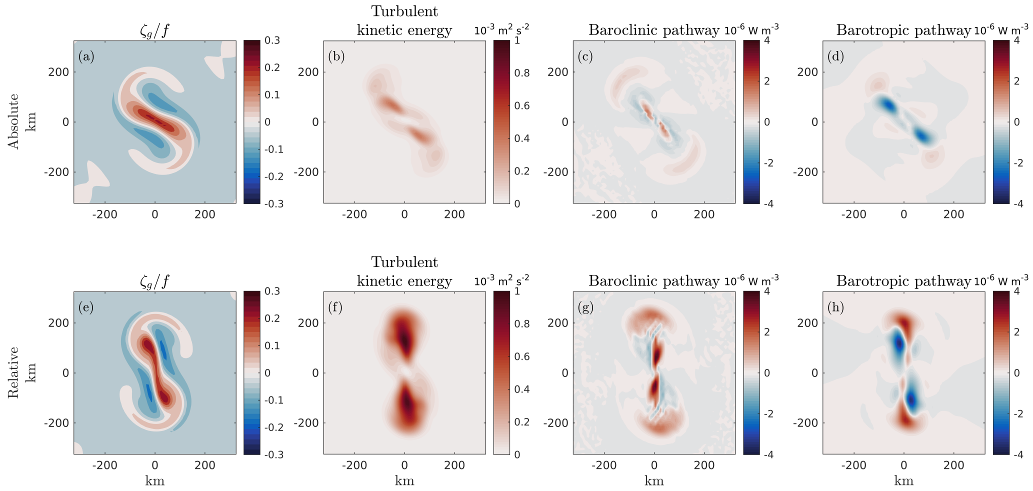

Figure 5.1.4: Horizontal patterns at day 175 of a,e) surface normalised relative vorticity, then profiles averaged over top 800 m of: b,f) $\frac{1}{2}\overline{(u_g'^2 + v_g'^2)}$ (in 10^{-4} m^2 s^{-2}), c,g) $-g\overline{\rho' w'}$ (in 10^{-7} W m^{-3}) and d,h) $\rho_0\overline{u_g'\boldsymbol{u'}}\cdot\nabla\overline{u}_g + \rho_0\overline{v_g'\boldsymbol{u'}}\cdot\nabla\overline{v}_g$ (in 10^{-7} W m^{-3}). Top is absolute wind stress and bottom is relative wind stress. Relative vorticity is calculated using MITgcm daily time-mean output, and energetic terms are 16 day time-means taken at day 175.

plan views of vertically averaged w reached 0.2 m day^{-1}, whilst the rms[w] peak is close to 0.04 m day^{-1}. In each case, relative wind stress introduced additional vertical motions. Figure 5.1.5 shows the same variables at the same time (day 100) for the CE. Again, a clear pattern of alternating up/down-welling cells is evident, but this time reaching much larger values than the ACE of around 0.3 m day^{-1} (Fig. 5.1.5a,b). The greater four cell signal suggests a much stronger and larger growth of azimuthal wavenumber $l = 2$. This increase is clear by looking at the rms[w], where peak values range from 0.07 - 0.09 m day^{-1} (Fig. 5.1.5c).

5.2 Anticyclonic eddy-wind interaction in a co-rotating regime

We now turn our attention to the co-rotating anticyclonic eddy. In the following analysis, the counter-rotating eddy from Wilder et al. (2022) is also presented so that comparisons can be made of each eddy response. We begin with a brief

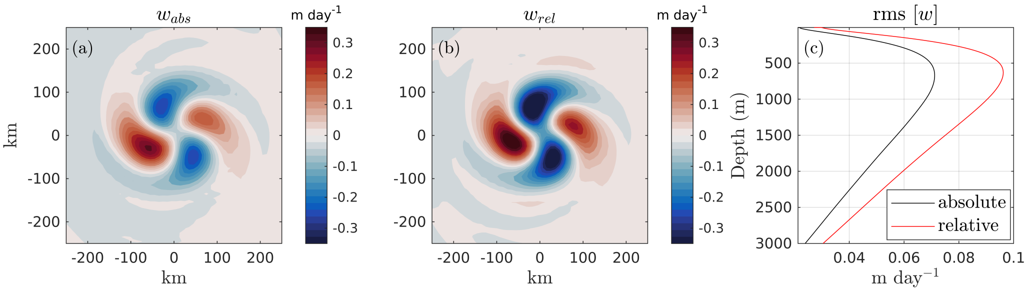

Figure 5.1.5: Model vertical velocity output averaged over top 800 m at day 100 (in m day^{-1}). Horizontal patterns of w in a) absolute wind stress and b) relative wind stress. In c) the root-mean-square of vertical velocity for absolute (black) and relative (red). Quantities are calculated using MITgcm daily time-mean output.

experimental setup that describes the difference in the co-rotating eddy model design. In the results section, we examine the eddy vertical velocity field, mean eddy energetics, revisiting the scaling introduced in Wilder et al. (2022).

5.2.1 Experimental setup

The primary model setup used in chapter 3 and Wilder et al. (2022) is employed here for the co-rotating eddy. To ensure the wind stress effects on the co-rotating eddy are comparable with the counter-rotating eddy, the eddy amplitude is kept the same. This makes the surface geostrophic motions equivalent. Because the co-rotating eddy has a smaller baroclinic component, or larger barotropic component (Katsman et al., 2003), the temperature anomaly with regards to the background temperature is made smaller. This makes ρ^* and subsequently the eddy potential energy smaller. The stratification of the water column is also marginally increased at depth to allow the co-rotating eddy velocities to reach the ocean floor (see Fig. 5.2.1). See Table 5.1 for key eddy parameters.

Table 5.1: Co-rotating eddy parameters

Symbol	Value	Description
A	25 cm	Eddy amplitude
H	4000 m	Ocean depth
f	9.3461×10^{-5} s^{-1}	Coriolis frequency
T'	1.5 °C	Temperature anomaly
γ	0.95	Governs stratification
ρ_0	1026 kg m^{-3}	Reference ocean density

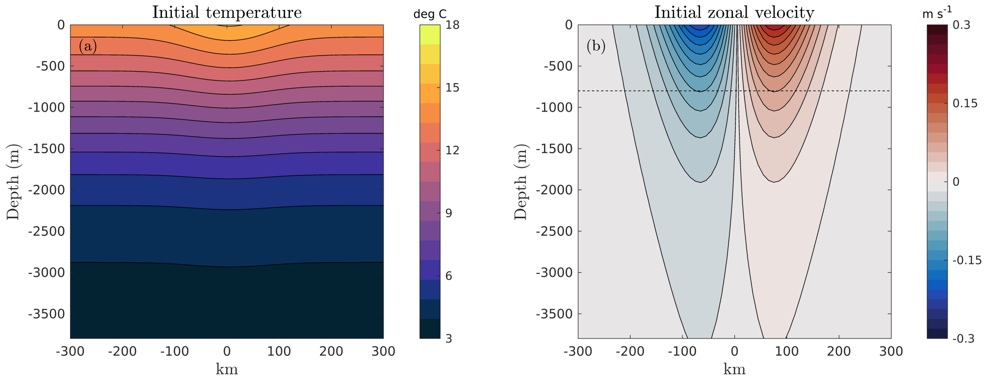

Figure 5.2.1: Meridional transects through the anticyclonic eddy centre of: a) initial temperature (in deg C) and b) zonal velocity (in m s^{-1}). The horizontal dashed line in b) is the depth of the upper layer, $H_1 = 800$ m.

5.2.2 Results

Eddy vertical velocity field

The vertical velocity field is examined in Fig. 5.2.2 for the co-rotating eddy in response to relative wind stress. The counter-rotating eddy from Wilder et al. (2022) is presented alongside for comparative reasons. For the counter-rotating eddy, Wilder et al. showed distinct wave-like patterns occuring in the horizontal profile of $\frac{1}{800}\int_{-800}^{0} w\, dz$ (Fig. 5.2.2a,b). These patterns indicate growth in an unstable azimuthal wavenumber $l = 2$ (Dewar et al., 1999; Pilo et al., 2018), where values in RW are larger due to linear Ekman pumping. A zonal transect through the origin shows the deep reaching nature of w (Fig. 5.2.2e,f), with additional velocities generated by linear Ekman pumping in relative wind stress visible down the water column.

In the co-rotating eddy, clear imprints of wind-induced Ekman pumping can be seen in the horizontal patterns (Fig. 5.2.2c,d). A dipole of up/down-welling is seen in AW and a slightly off-centre upwelling exists in RW, all present in a vertical average over the top 800 m. This shows that wind-induced Ekman pumping pattern extends down the co-rotating eddy water column with each wind stress. These Ekman pumping patterns are also similar to those found at the surface in the counter-rotating eddy in Figs. 3 and 4 in Wilder et al. (2022), implying each wind stress has the same effect regardless of the eddy's vertical structure. Transects of w show a vertical eddy pump that is governed by the surface wind stress (Fig. 5.2.2g,h). The dipoles in AW clearly reach from the surface to around 2500 m, whilst the off-centre upwelling in RW extends all the way to 3000 m. The results of the vertical pump in the co-rotating eddy in response to relative wind stress are consistent with previous studies on Ekman pumping (Dewar and Flierl, 1987; Gaube et al., 2015). Nevertheless, relative wind stress still generates additional vertical velocities, regardless of the eddy vertical structure, and it is this effect we examine next.

Mean energetics

The evolution of time-mean eddy energetics of the co-rotating eddy are now presented alongside the counter-rotating eddy from Wilder et al. (2022) in a time-series of volume integrated quantities shown in Fig. 5.2.3. When directly comparing mean energetics between eddy types, we focus on the time series up to day 150 when the counter-rotating eddy remains stable. Beyond this time frame the comparison is no longer justified. As a general overview, we can observe that $KE_M + PE_M$ and KE_M differ between the eddy types (Fig. 5.2.3a,b). First, $KE_M + PE_M$ is smaller in the co-rotating eddy as a result of the weaker potential energy due to the reduced temperature anomaly. Second,

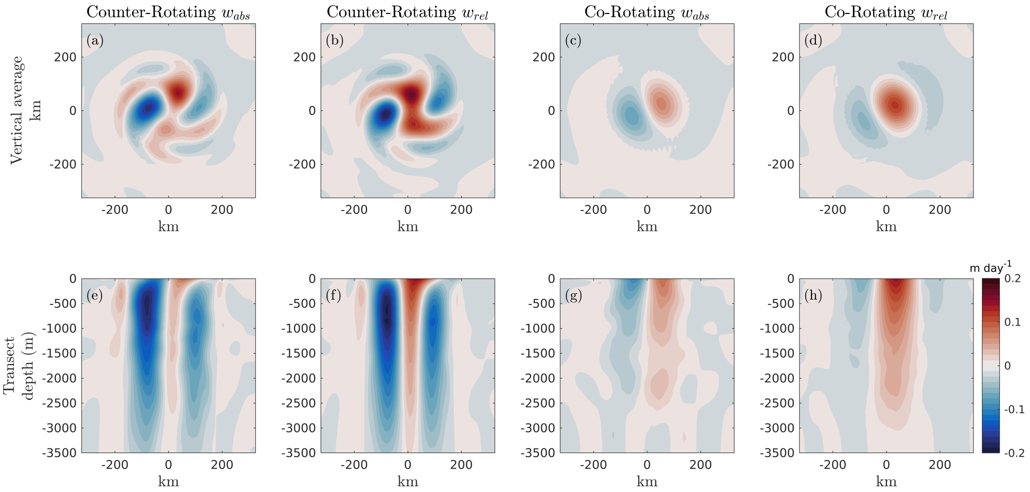
Counter-Rotating w_{abs} Counter-Rotating w_{rel} Co-Rotating w_{abs} Co-Rotating w_{rel}

Figure 5.2.2: Model vertical velocity output at day 100 (in m day^{-1}). Horizontal patterns averaged over top 800 m for a,c) absolute wind stress and b,d) relative wind stress, and zonal transects through eddy centre for e,g) absolute wind stress and f,h) relative wind stress. Counter-rotating in the left four panels, and co-rotating in right four panels. Quantities are calculated using MITgcm daily time-mean output.

differences in co-rotating KE_M are because the deep horizontal velocities are weaker compared with the counter-rotating eddy. Another clear result is no exponential-like growth/changes in the co-rotating eddy energetic terms. This is because a co-rotating anticyclonic eddy is stabilised by the reduced baroclinic component (Dewar et al., 1999).

Now, examining the co-rotating eddy, AW $KE_M + PE_M$ is seen to increase slightly with time, suggesting there is an enhanced supply of energy not seen in the counter-rotating eddy. A reason for this was suggested in chapter 3, section 3.3 to be a result of diffusive processes. In RW, relative wind stress damps $KE_M + PE_M$ (Fig. 5.2.3a). From day 31 to 150, the co-rotating eddy loses 2.5×10^{14} J of total energy, in contrast to the counter-rotating eddy, which loses 4×10^{14} J. What is more, $KE_M + PE_M$ removed by wind damping alone accounts for 2.8×10^{14} J in the counter-rotating and 2.7×10^{14} J in the co-rotating over the same time period (Fig. 5.2.3c). This additional loss of energy in the counter-rotating eddy could be due to its larger total mean kinetic energy (Fig. 5.2.3b), and likely larger viscous dissipation. Nevertheless, relative wind stress damping is equivalent as long as the counter-rotating eddy remains stable, where instability is shown by the increase in P_{rel} that is associated with the increase in KE_M.

The damping of KE_M in the co-rotating eddy by relative wind stress is significant over the course of the simulation, decaying by around $\sim 50\%$ in RW, compared to only $\sim 13\%$ in AW. In contrast with the counter-rotating eddy, which does not exhibit a visible decay in RW KE_M, this suggests that baroclinic conversion is not counteracting relative wind stress damping in the co-rotating eddy. It can also be seen that the baroclinic conversion term $C(PE_M, KE_M)$ is much smaller in the co-rotating eddy, possibly due to the weaker temperature anomaly.

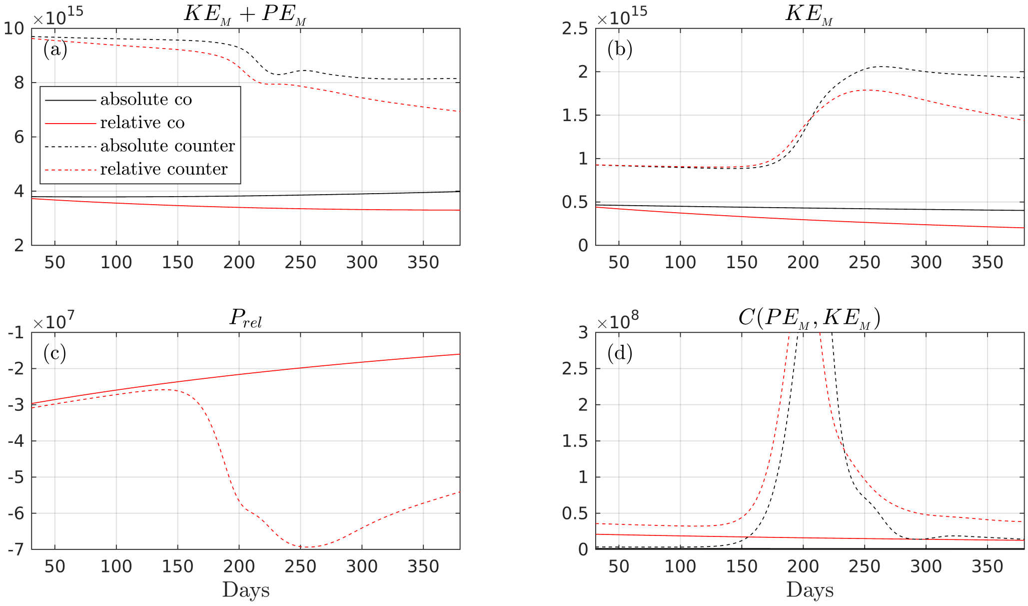

Figure 5.2.3: Time-series from day 31 to 300 comparing absolute (black) and relative (red) wind stress simulations of: a) total mean energy, b) mean kinetic energy, c) relative wind stress damping, and d) conversion of mean potential to mean kinetic energy. Terms in a,b,d) are volume integrals, and c) is a spatial integral. Co-rotating given by full lines, counter-rotating given by dashed lines. Each day represents a 16-day time-mean. Units of energy in J and damping/conversion in W.

To get a better perspective of the co-rotating eddy response to relative wind stress, we decompose volume integrals of mean kinetic energy and the conversion of mean potential to mean kinetic energy into upper and lower layers, shown in Fig. 5.2.4. The upper layer is defined as the volume including and above 800 m, and the lower layer is that below. The first observation is that upper layer kinetic energy is larger in the co-rotating case due to weakened thermal wind shear and more barotropic flow (Fig. 5.2.4a). As we might expect, lower layer kinetic energy is small in the co-rotating eddy, around 16 times that of the counter-rotating eddy (Fig. 5.2.4b). As with volume integrated terms in Fig. 5.2.3, values evolve linearly in the co-rotating eddy, whilst the counter-rotating eddy undergoes instabilities.

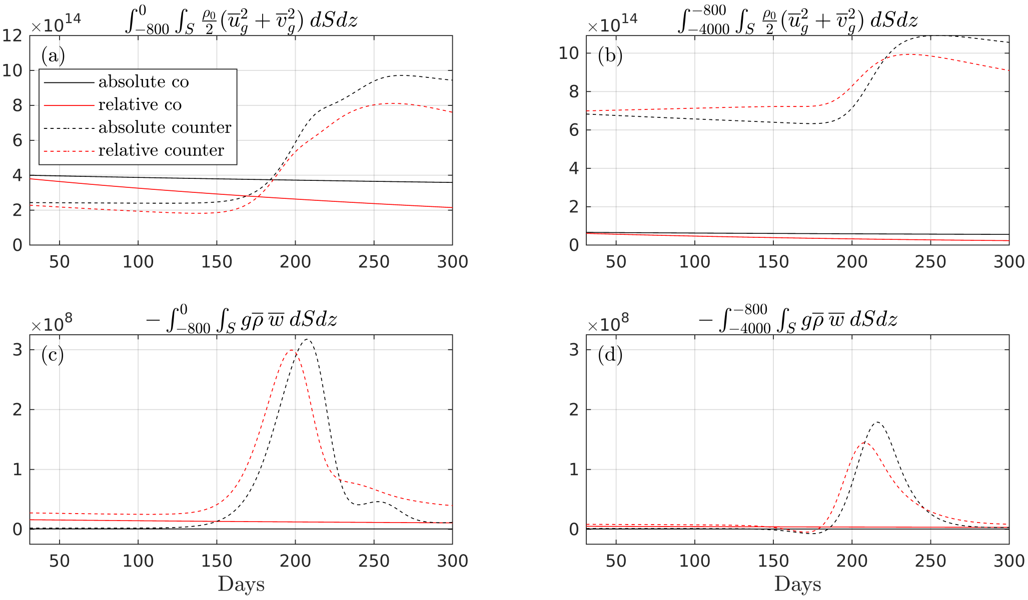

Figure 5.2.4: Time-series from day 31 to 300 comparing absolute (black) and relative (red) wind stress simulations of: a) upper layer mean kinetic energy, b) lower layer mean kinetic energy, c) upper layer conversion of mean potential to mean kinetic energy, and d) lower layer conversion of mean potential to mean kinetic energy. Terms are volume integrated over upper (0 to -800 m) and lower (-800 m to -4000 m) layers. Co-rotating given by full lines, counter-rotating given by dashed lines. Each day represents a 16-day time-mean. Units of energy in J and conversion in W.

We now look at the efficiency of relative wind stress damping on upper layer mean kinetic energy. Over days 31 to 150 of the time-series, RW upper layer kinetic energy is damped more in the co-rotating eddy (Fig. 5.2.4a). Quantifying this damping, we find a reduction of $\sim 4 \times 10^{13}$ J in the counter-rotating eddy and $\sim 1.8 \times 10^{14}$ J in the co-rotating eddy, with respect to values at day 31. Indeed this is the case when both eddy types undergo $\sim 3 \times 10^{14}$ J of dissipation due to relative wind stress (Fig. 5.2.3c), since geostrophic surface velocities are the same between eddy types. This disparity in upper layer kinetic energy damping is a result of upper layer baroclinic conversion (Fig. 5.2.4c), which is lower in the co-rotating case. Over the same time period, additional upper layer baroclinic conversion due to relative wind stress is $\sim 2.8 \times 10^{14}$ J in the counter-rotating eddy and $\sim 1.6 \times 10^{14}$ J in the co-rotating eddy. Because the co-rotating eddy has a reduced temperature anomaly compared to the counter-rotating eddy (see section 5.2.1), there is less mean potential energy for the wind induced Ekman pumping to convert into mean kinetic energy.

The response of the lower layer is also different in the co-rotating eddy. Again, focusing on the time series up to day 150, lower layer mean kinetic energy is damped in the co-rotating case, whilst increases in the counter-rotating case (Fig. 5.2.4b). This difference is attributed to the weakened baroclinic component in the co-rotating eddy (Fig. 5.2.4d), as it is not able to extend all the way down the water column.

Revisiting the scaling

A ratio of $C(PE_{_M}, KE_{_M})_{rel} - C(PE_{_M}, KE_{_M})_{abs}$ to P_{rel} is plotted in Fig. 5.2.5. In the counter-rotating eddy, the ratio sits just above 1 for over half the simulation (prior to eddy breakup), showing relative wind stress damping is counteracted by additional baroclinic conversion, as discussed in Wilder et al. (2022). In the co-rotating eddy, the ratio sits below 1 for all time and tells us that P_{rel} dominates over additional $C(PE_{_M}, KE_{_M})$, explaining why $KE_{_M}$ decreases (Fig. 5.2.3b). This change in ratio between the counter- and co-rotating eddy is because less additional baroclinic conversion is generated by linear Ekman pumping in the co-rotating case. To understand why, recall the scaling of additional $C(PE_{_M}, KE_{_M})$ to P_{rel} from Wilder et al. (2022), given by

$$\frac{\int_V C(PE_{_M}, KE_{_M})\, dV}{P_{rel}} \sim \frac{Hg\overline{\rho^*}\zeta_g}{\rho_0 f \boldsymbol{u}_s^2} \,, \tag{5.2.1}$$

where $\boldsymbol{u}_s$ is the surface ocean current. If we consider the density deviation ρ^* in (6.2.1), then this will vary depending on the amplitude of the eddy temperature anomaly. From the thermal wind balance, the larger the horizontal temperature gradients are, the greater the baroclinic shear will be. For eddies that have the same sea surface height anomaly, a counter-rotating eddy will have a stronger baroclinic component than its co-rotating counterpart, as more baroclinic shear is needed to generate the counter-rotating deep flow. So, in this case ρ^* determines which quantity in (6.2.1) will be dominant. In the counter-rotating eddy, $\rho^* \sim 10^{-1}$, and in the co-rotating eddy, $\rho^* \sim 10^{-2}$. Using typical eddy parameter values $\zeta_g \sim 10^{-6}$ s^{-1}, $\boldsymbol{u}_s^2 \sim 10^{-2}$ m^2 s^{-2} and values in Table 5.1, the ratio is greater than 1 in the counter-rotating regime, and less than 1 in the co-rotating regime, consistent with numerical results in Fig. 5.2.5.

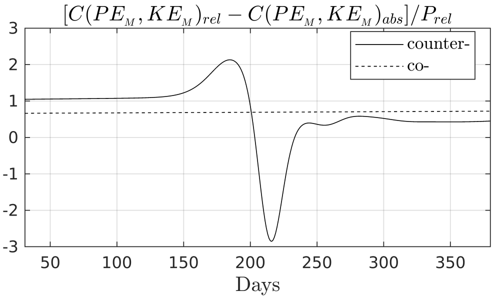

Figure 5.2.5: Time-series from day 31 to 380 comparing the ratio of additional baroclinic conversion by relative wind stress to relative wind stress damping in the counter-rotating (full) and co-rotating (dashed) eddy. Terms are volume integrals. Each day represents a 16-day time-mean.

5.3 Concluding chapter remarks

In this chapter we examined the sensitivity of relative wind stress forcing under modified eddy parameters. In the first section, we tested the response of a cyclonic eddy by choosing oppositely signed sea surface height and temperature anomaly to the anticyclonic eddy. This produced a cyclonic eddy with equivalent geostrophic energy. The response of the cyclonic eddy was found to be broadly similar to the anticyclonic eddy. Total eddy energy is found to decay over the whole simulation due to relative wind stress damping. The reported counteracting of relative wind stress damping by additional baroclinic conversion in Wilder et al. (2022) is observed in the cyclone too for at least the first 150 days. This is explained by the cyclone-anticyclone symmetry, whereby relative wind stress induces equivalent energetic responses in geostrophic eddies. A clear asymmetry in destabilisation timescale does arise though between the anticyclone and cyclone. The shorter timescale for destabilisation in the cyclone results in less damping of upper layer mean kinetic energy whilst the eddy is in a stable state. Eddy instabilities are also generated earlier in the cyclonic eddy, and are also found to be around twice the size of the anticyclone, implying the cyclonic eddy is much more unstable. Ageostrophic vertical motions are also presented to show the extent of the azimuthal wavenumber $l = 2$ pattern. The cyclonic eddy exhibits much greater ageostrophy than the anticyclone, where relative wind stress increases the magnitude of this pattern.

In the second section, the response of a co-rotating anticyclonic eddy was investigated and contrasted with the counter-rotating eddy. For this experiment, we reduced the temperature amplitude and subsequently the baroclinic component of the eddy so it no longer maintained a dominant first baroclinic mode structure. The co-rotating flow was shown to stabilise the eddy considerably (Dewar et al., 1999). The co-rotating vertical velocity field was clearly generated via Ekman pumping at the surface and throughout the water column, indicating a much more stable eddy than the counter-rotating case, which was populated by azimuthal perturbations. The stabilising nature of the co-rotating deep flow is carried through into the energetics. We find that relative wind stress dampens both total energy and mean kinetic energy for all time. In contrast to the counter-rotating case, baroclinic conversion does not completely counteract relative wind stress damping. This is in response to a weakened conversion of mean potential to mean kinetic energy in the co-rotating eddy. The reason for this is described using the scaling derived in Wilder et al. (2022). The scaling is shown to depend on the density deviation ρ^*, which controls the amount of potential energy that can be released by Ekman pumping. This highlights relative wind stress damping efficiency is dependent on the eddy's baroclinic component.

Despite the parameters studied in this chapter, there remain many others that we have not approached. In chapter 2, we were able to conduct numerous simulations based on differing eddy parameters due to the low computational cost of running barotropic eddy simulations. In the case of a continuously stratified baroclinic eddy, the computing costs begin to grow, but in particular the amount of storage space needed for the post-processing of data is much larger than the barotropic case. Therefore, in this chapter we focused only on key aspects we found interesting to explore, such as the cyclonic eddy and the co-rotating anticyclonic eddy.

Nevertheless, it is still important to consider what impact other eddy parameters may pose. For example, eddies with increasing Rossby number ($Ro = U/fL_e$) were shown by Mahdinia et al. (2017) to have larger modal growth rates. Of course, the Rossby number is a function of eddy sea surface height via geostrophic velocity, and therefore by altering the amplitude of the eddy we might expect the timescales for eddy destabilisation to shorten/lengthen. Given the scaling of baroclinic conversion and relative wind stress damping, the counteracting process should still happen, particularly in a first baroclinic mode eddy. The Burger number ($Bu = R_d/L_e$) is the ratio of the first baroclinic Rossby radius of deformation, R_d, to an eddy length scale, and can be considered in terms of eddy stability. Stegner and Dritschel (2000) found eddies with small Bu to be more stable than eddies with large Bu. So, if we were to reduce the length scale of the eddy but maintain the stratification, then Bu increases and the eddy becomes more unstable, and the timescale for eddy destabilisation may shorten. Since neither the scaled baroclinic conversion or relative wind stress damping depend on eddy radius, we have no reason to think modifying this parameter would impact the counteracting damping process.

A Gaussian function is employed for eddy shape because it matches the inner 2/3rds of the average sea surface height distribution (Chelton et al., 2011). Yet it was also shown by Chelton that a quadratic function can capture the mode of sea surface height. We also briefly discussed in the introduction some of the literature that looked at the steepness parameter in terms of eddy stability. This topic offers another subject area worth studying. It could be interesting to quantify whether linear Ekman pumping can still transfer horizontal buoyancy gradients into vertical gradients when the steepness of the eddy profile is altered. In general, how might relative wind stress interact with greater vorticity and momentum gradients, which are strongly related with ageostrophy and tracer fluxes.

In all our experiments we have not considered altering the depth of the ocean or the upper layer depth. The co-rotating eddy considers a horizontal velocity profile that extends through the water column, where its deep flow is zero at the ocean bottom. However, even in this regime the effective thermocline depth was still kept at 800 m. Indeed, reducing the depth of the ocean will take our idealised eddies out of the mid ocean and closer to depths found in the western boundaries and some regions of the Antarctic Circumpolar Current. A reduced ocean depth will also reduce total eddy energy. However, we have seen that relative wind stress generates Ekman pumping down the whole eddy column, beyond the thermocline depth, so it seems unlikely that this wouldn't be the case in a similar setup but with modified layer depths. This ensures that kinetic energy production takes place down the whole water column and is consistent with the depth dependent scaling. Yet, modifying the layer depths also requires changes to the sea surface height and temperature amplitudes to maintain a first baroclinic mode eddy structure. So it seems plausible that this could alter the ratio between kinetic energy production and kinetic energy damping.

In any case, we have demonstrated two interesting parameter studies for relative wind stress damping. We conclude the thesis in the next chapter by offering wider limitations to the work carried out, and suggesting numerous other pathways for this research to continue ahead.

6

Conclusion

6.1 Can the decay of eddy energy be predicted?

The first objective of this thesis was to predict the decay of eddy energy due to relative wind stress damping, detailed in chapters 2 and 3. Obtaining a rate of dissipation for mesoscale eddy energy is vital for eddy parameterisations in global climate models (Mak et al., 2022). We utilised theoretical techniques (Cushman-Roisin and Beckers, 2006) and well known eddy statistics (Chelton et al., 2011) to develop a simple prediction method, which was then compared against an idealised numerical model, MITgcm (Marshall et al., 1997a). The basis of this work draws on fundamental concepts of eddy shape, vertical eddy structures, and eddy-wind interactions. We make use of the fact that eddy kinetic energy is partitioned in either the barotropic or first baroclinic mode, as well as sea surface variability primarily reflecting the movement of the main thermocline, or first baroclinic mode (Wunsch, 1997). Taking account of the ocean surface current in wind stress removes total eddy energy and is considered a significant controlling mechanism on eddy lifetime (Xu et al., 2016).

In chapter 2, a first step towards predicting eddy energy decay is through the derivation of an analytical wind power input. By making assumptions of a Gaussian shaped barotropic eddy in geostrophic balance (Chelton et al., 2011), we arrive at an expression for wind power input that depends on key parameters like eddy amplitude and wind speed, and is given by

$$P_{rel} = -\rho_a \Big(2a_1 + 3a_2 \left| u_a \right| + 4a_3 \left| u_a \right|^2 \Big) \frac{g^2 A^2 \pi}{2f^2} \; .$$

The prediction of eddy energy is then made by varying parameters and comparing the results with idealised simulations in MITgcm. We show that predicted barotropic eddy energy in the midlatitudes is in close agreement with idealised simulations. A barotropic decay timescale is also similar to the one posed by Gaube et al. (2015), who used an Ekman pumping approach. Fitting a gradient wind balance (GWB) to the MITgcm sea surface height field displays a near match with diagnosed MIT total eddy energy, suggesting that a GWB prediction method may have been more appropriate. By varying the Coriolis parameter, eddy amplitude, and radius, we find that for $Ro > 0.1$, predicted eddy energy does not match numerical eddy energy, and therefore the prediction method is not suitable in this parameter range. In addition, increased wind speeds are also shown to damp total eddy energy at a faster rate, consistent with the barotropic decay timescale. The work in chapter 2 therefore verifies the analytical wind power input for use in predicting the damping of total eddy energy.

The variability in sea surface height data reflects the motion of the first baroclinic mode (Wunsch, 1997). In chapter 3, the next logical step attempts to predict the decay of baroclinic eddy energy using a theoretical model with a first baroclinic mode structure. This model displays the features reflective of anticyclonic or cyclonic eddies, such as the depressed or raised main thermocline, respectively. We show that the decay rate of baroclinic total eddy energy in a midlatitude eddy is accurately predicted for $\sim$ 100 days. A derivation of the baroclinic decay timescale hints at an eddy attenuation via the relaxing of the thermocline displacement, consistent with sea surface height and potential energy decay in the prediction and MITgcm. The rate of eddy energy decay is equivalent between the prediction and MITgcm. Beyond $\sim$ 100 days, the prediction method breaks down when the numerical simulation exhibits a sudden reduction in total eddy energy. These changes in the idealised MITgcm runs are hypothesised to be a result of energy conversion and growth of eddy instabilities, both absent from the linearised two-layer model. The sudden reduction in potential energy and increase in kinetic energy suggest a clear correlation between these two phases. At the time stamps of these energetic changes, horizontal plan views of MITgcm kinetic energy display azimuthal wave-like patterns, a clear indication that the eddy is departing from its Gaussian shape.

6.2 How do mesoscale eddies respond to relative wind stress forcing?

The dynamics of idealised mesoscale eddies are well documented (Dewar and Flierl, 1987; Dritschel, 1989; Stegner and Dritschel, 2000; Baey and Carton, 2002; Sutyrin, 2016), yet their energetic and stability response to relative wind stress is unclear. A dedicated idealised eddy-wind study was first carried out in chapter 4 to fill in some of the literature gaps and also establish reasons for the break down in the prediction method seen in chapter 3. We find that relative wind stress damps total eddy energy, consistent with it being a drag on the system (Dewar and Flierl, 1987). In terms of total mean kinetic energy, relative wind stress damping is counteracted by an additional conversion of potential to kinetic energy via wind stress curl induced Ekman pumping. This key result is supported through a scaling of additional baroclinic conversion and relative wind stress damping,

$$\frac{C(PE_{_M}, KE_{_M})}{P_{rel}} \sim \frac{Hg\overline{\rho^*}\zeta_g}{\rho_0 f \boldsymbol{u}_{gs}^2} \,. \tag{6.2.1}$$

At the eddy surface, relative wind stress removes mean kinetic energy, although the conversion term counteracts this surface damping to some degree, an effect seen in Renault et al. (2018) and Shan et al. (2020). The eddy also undergoes an earlier destabilisation due to relative wind stress through Ekman pumping.

Eddy stability is modulated by the transfer of horizontal buoyancy gradients into vertical gradients through this Ekman pumping, enhancing the condition for baroclinic instability in the counter-rotating eddy.

In chapter 5, we began by examining a cyclonic eddy under relative wind stress forcing. Findings are analogous to the anticyclonic eddy in Wilder et al. (2022), showing that relative wind stress induces similar responses in the eddy irrespective of the eddy's polarity. The key difference in the cyclonic eddy is the shorter timescale to destabilisation, a response of the documented anticyclone-cyclone asymmetry (Katsman et al., 2003; Mahdinia et al., 2017). The vertical structure of the anticyclonic eddy was then modified to improve its stability. This was done by reducing the baroclinic component and having complete co-rotation of horizontal eddy velocities. Relative wind stress was found to dampen both mean total and mean kinetic energy. Because of the modified vertical structure, baroclinic conversion was not large enough to counteract relative wind stress damping. This change in eddy response was described through changes to the density deviation, ρ^*, in the scaling term from Wilder et al. (2022).

6.3 What are the implications of these findings?

6.3.1 For eddy energy dissipation parameterisations

Current energy budget-based eddy parameterisations require eddy energy dissipation rates (e.g. (Mak et al., 2018; Jansen et al., 2019)), as well as knowledge of the dynamic response caused by the specific dissipation mechanisms. For example, Jansen et al. (2019) represent the kinetic energy cascade at the subgrid scale by calculating a GM diffusivity based on a predicted kinetic energy. The kinetic energy informed GM coefficient is then used in the calculation of the forward cascade that supplies kinetic energy. Within their kinetic energy budget also resides a dissipation term, which is built using a bottom drag mechanism and biharmonic viscosity. Some immediate implications to this work could come from our analytical wind power input and enhanced energy conversion by relative wind stress. Other energy budget based parameterisations such as GEOMETRIC (Mak et al., 2018) and GM+E (Bachman, 2019) have made significant improvements to ocean energetics in coarse resolution models, though the authors recognise the need to include and implement constrained eddy dissipation rates as a top priority. This thesis certainly provides the groundwork for an eddy dissipation parameterisation due to relative wind stress.

In GEOMETRIC (Mak et al., 2018), the value for the dissipation rate, λ, is arbitrarily chosen, and accounts for all the myriad eddy dissipation mechanisms. The work in chapters 2 and 3 present dissipation timescales due to relative wind stress that could vary quite widely over the ocean. Two forms of λ are therefore based on the barotropic and baroclinic timescales and could be implemented in GEOMETRIC. The barotropic dissipation rate from Eq. (2.1.25) looks like

$$\lambda_{bt} = \frac{\rho_a\Big(2a_1 + 3a_2\left|u_a\right| + 4a_3\left|u_a\right|^2\Big)}{\rho_0 H}\,, \tag{6.3.1}$$

which clearly varies with ocean depth and wind speed. The baroclinic dissipation rate from Eq. (3.1.20) takes the form

$$\lambda_{bc} = \frac{2\rho_a\big(2a_1 + 3a_2\left|u_a\right| + 4a_3\left|u_a\right|^2\big)g^2\mu^2}{\rho_0 R^2 g\prime f^2}\,, \tag{6.3.2}$$

which depends on more parameters due to the stratification of the baroclinic eddy. Based on the past parameters chosen for the eddy timescales in chapters 2 and 3, each dissipation rate - λ_{bt} and λ_{bc} - are of $O(10^{-8})$, which is an order of magnitude smaller than the $O(10^{-7})$ chosen by Mak et al. (2018) for all combined dissipation mechanisms. In Mak et al. (2022), ACC and AMOC volume transport are shown to be sensitive to changes in the eddy energy dissipation rate, λ, even by changes of only $O(10^{-8})$. Therefore, the implications of a modified dissipation rate due to relative wind stress could potentially lead to significant changes in the global ocean circulation.

6.3.2 In general

Beyond the prediction method, one of the most unique findings to come from this thesis is the earlier eddy destabilisation due to relative wind stress, described in Wilder et al. (2022). This earlier destabilisation exhibits up/down-gradient momentum and density fluxes sooner than they would take place in an absolute wind stress case. Relative wind stress also dampens the magnitude of these fluxes, or instabilities in the eddy. Consider a regional ocean model forced by absolute and relative wind stress. Relative wind stress will naturally dampen the eddy field (Seo et al., 2016), which will also dampen turbulent fluxes of momentum and density. Weaker fluxes will also lead to reduced turbulent mixing and dissipation at small scales (McWilliams, 2021). This will also translate towards damping of other tracer fluxes, such as carbon and nutrients, which could impact processes such as eddy ventilation in the Southern Ocean (Dove et al., 2022). At the domain scale, this damping of the eddy tracer fluxes may correspond to weakened sources or sinks of ocean properties. What is not clear is where the shorter destabilisation timescale is relevant to the large-scale, or its importance resides at the localised eddy scale.

6.4 Wider limitations of this work

The overarching goal of this thesis aimed to improve our understanding of mesoscale eddy dissipation due to relative wind stress. This is important because eddy parameterisations like GEOMETRIC (Mak et al., 2017) and other energy based eddy parameterisations (Eden and Greatbatch, 2008; Jansen et al., 2019) depend on an eddy dissipation rate. For all the progress made in this thesis, we nevertheless outline some of the limitations to this work.

Chapter 2 details the derivation of an analytical expression for relative wind stress damping over a circular Gaussian eddy. This equation then enables the damping of total eddy energy to be predicted based on an eddy amplitude found from the total energy of the eddy. The applicability of this wind stress damping term assumes an average eddy profile can be used for mesoscale eddies over the global ocean (Chelton et al., 2011). It has recently been put forward by Chen et al. (2019) that mesoscale eddies are closer to an ellipsoidal shape than circular, and it was even noted by Chelton et al. (2011) that a quadratic function is a better fit for the mode of eddy sea surface height. Employing the barotropic model will also be ill-suited in more realistic regional settings. This is because barotropic energy is poorly captured from sea surface variability (Wunsch, 1997), or has at least been found to make limited contributions to overall kinetic energy (Baker-Yeboah et al., 2009).

At the ocean surface, geostrophic kinetic energy is dominated by the first baroclinic mode, meaning eddy vertical structure can be inferred from sea surface height data (Wunsch, 1997). Chapter 3 utilises a two-layer model that exhibits a singular first baroclinic mode structure, and is therefore an appropriate framework to predict the damping of total eddy energy using the sea surface height. Despite this, it proved difficult to devise a continuously stratified model (MITgcm) that displayed the same energy based on approximate density structure as the two-layer model. The focus was on matching the MITgcm with the two-layer in terms of basic eddy parameters - e.g. layer depths and eddy amplitude - as well as the first baroclinic mode structure. The two-layer model then exhibited kinetic energy levels higher than MITgcm. This poses some issues that need attention. Rather broadly, was the MITgcm setup correct to model a baroclinic eddy? Or could an alternative analytical approach be considered e.g. quasi-geostrophic.

Suppose the two-layer model is the appropriate approach, the next obvious limitations to this method is the break down after ~ 100 days. Investigating the eddy dynamics in Wilder et al. (2022) helped elucidate what the two-layer model lacked. For example, the sudden reduction in potential energy and increase in kinetic energy are indicative of an energy cascade. As mentioned in chapter 3, the two-layer model does not include the transfer of energy between reservoirs and modes. For this reason, this enables relative wind stress to dampen eddy energy efficiently in the two-layer model. Yet we know relative wind stress damping of kinetic energy is offset by an enhanced energy conversion. This suggests that these processes need to be added into this method to enable its wider applicability.

Idealised modelling studies are excellent tools to help diagnose fundamental dynamical responses. Chapter 4 examined in depth the response of a mesoscale eddy to relative wind stress forcing. Whilst this study brought to light some interesting results, there are limits to how far we can interpret the findings. It is now well known that mesoscale eddies can impact their surrounding environment. For example, positive (negative) eddy sea surface temperature anomalies can intensify (weaken) surface winds (Frenger et al., 2013). Therefore, in our numerical model, wind stress should also be a function of sea surface temperature to account for changes in atmospheric stability (Small et al., 2008). If wind speeds change over each eddy, then we might expect the dissipation of eddy energy to be asymmetric between an anticyclone and cyclone. For example, there could be more damping over anticyclones in response to enhanced wind speeds. On the other hand, Byrne et al. (2016) found this thermodynamic feedback was able to inject kinetic energy into mesoscale eddies, depending on the meridional gradient of the wind. In addition, our model also neglects any exchange of heat at the air-sea interface, which could play an important role in the dynamics of the eddy (Molemaker and Dijkstra, 2000). There are clearly further studies to be conducted that should look at building a more realistic eddy model.

Following the wind speed sensitivity experiments of chapter 2, we attempted to carry out similar experiments for the baroclinic eddy in chapter 3. However, problems were encountered and they have not been presented in this thesis. Using the setup for the anticyclonic baroclinic eddy, a wind speed beyond 7 m s^{-1} began to introduce spots of noise in the vertical velocity field. This suggests that the current parameters chosen for viscosity and diffusivity are not adequate for increased wind speed. A way to get around this would be to modify the viscous and diffusive parameters, e.g. by doubling them, which would dampen any high frequency events that could cause the noise. However, this comes with the caveat that these sensitivity experiments would not be comparable with the past experiments. What this demonstrates is a need to plan ahead the numerical setup for the types of sensitivity tests we want to conduct.

6.5 Future research

The research in this thesis provides an overview of mesoscale eddy dissipation by relative wind stress. The primary goal of this thesis was to contribute to the eddy energy budget-based parameterisations by introducing a constrained dissipation rate due to relative wind stress. Indeed, this thesis derives analytical dissipation rates based on simple theory that could be used in eddy energy budget-based parameterisations. An immediate extension would be to develop this further through the implementation and testing of these dissipation rates in global circulation models. This could lead to the improvement of future projections of the global ocean circulation (Mak et al., 2022). Below we outline some additional future work on eddy-wind parameterisations, alongside some interesting additions to the body of literature on eddy dynamics in response to relative wind stress.

In the prediction method, the two-layer model in chapter 3 was perhaps too simple to adequately model a continuously stratified baroclinic eddy. In an ideal world, the two-layer model density need not be modified to match MITgcm potential energy, as they would match straight off. An alternative setup could be arranged where MITgcm employs a cosine function that describes a first baroclinic mode, similar to that used by Dunphy and Lamb (2014). This may improve the alignment of kinetic energy and reduction in potential energy in MITgcm. Moreover, the number of parameters explored in the prediction method are limited, particularly in the baroclinic case (chapter 3). It would be interesting to examine how the current prediction method fairs when the ocean depth and layer depths are altered. Using the current ratio of upper to lower layer depth (0.25) and the same parameters, if we reduced the depth of the ocean, then the prediction method might break down sooner in response to a reduced gap in surface to deep potential vorticity gradients (Dewar et al., 1999). In a similar train of thought, reducing the upper to lower layer depth ratio could lead to an improved prediction method timescale before break down. These are worth exploring in the future.

Following the additional parameter studies, the next work could focus on developing and improving the total eddy energy prediction method. We found the prediction method to break down as a result of an unstable baroclinic eddy in MITgcm. We should then look at including the processes found in MITgcm into the two-layer model. So that the sudden changes in MITgcm quantities can be represented, a growth rate for the azimuthal wavenumber $l = 2$ needs to be incorporated. This could be calculated through our own linear stability analysis, or taken from the current literature (Katsman et al., 2003; Mahdinia et al., 2017). We also need to include the cascade of energy, such as the transfer from first baroclinic to barotropic modes, and the release of potential energy induced by relative wind stress. Implementing these dynamics and testing them is the next step in the development of a subgrid eddy energy parameterisation that takes note of the complex relative wind stress damping mechanism.

Exploring submesoscale resolving simulations of idealised baroclinic eddies is a possible relevant next step from the work in Wilder et al. (2022). There is a growing debate surrounding the importance of submesoscale processes and their feedback onto the large scale (Hewitt et al., 2022). As such it would be appropriate to diagnose whether relative wind stress can impact a submesoscale resolving simulation any differently. We do know that increasing model resolution increases resolved kinetic energy (Kjellsson and Zanna, 2017) and the speed of vertical motions (McWilliams, 2021), so this is expected. A reviewer for Wilder et al. (2022) was also curious to see how a deep overwintered mixed layer would impact a warm core eddy response to relative wind stress. In our setup we did not consider a mixed layer, or at least it was very shallow. We might expect this addition to induce mixed layer instabilities that occur at the submesoscale (Boccaletti et al., 2007; Brannigan et al., 2017), though how relative wind stress damping might effect these mixed layer instabilities is unclear. A study that considers the seasonal cycle of heating and cooling will improve the realism of this current idealised setup.

In the global ocean, mesoscale eddies are rarely isolated, typically propagating over the ocean (Morrow et al., 2004), as well as merging and splitting with other eddies (Schouten et al., 2000). In this study, we focused on isolated eddies as our primary intention set out to constrain an eddy energy dissipation rate due to relative wind stress. To instigate propagating eddies, the domain should be set up on a beta plane. Evolution of eddies on a beta plane has been studied in the past (Dewar et al., 1999), though this setup has not been examined in response to relative wind stress. How does the beta effect impact wind-induced Ekman pumping and its subsequent effect on energy conversion and counteracting of relative wind stress damping? It is known through satellite altimetry that eddies interact with one another (Chelton et al., 2011), which can influence various processes, such as cross gyre transport (Kaneko et al., 2015), eddy lifetime (Zhai et al., 2010; Nan et al., 2011), and biogeochemical processes (Durán-Campos et al., 2019). Therefore, what happens to the above processes when relative wind stress is included? Could we develop an improved eddy energy dissipation parameterisation that takes into account these complex eddy-eddy interactions?

An area that we hoped to explore at some point in this thesis was the effect of surface heat fluxes. Sea surface temperature anomalies have been shown to be important for mesoscale eddy energy (Byrne et al., 2016), particularly through their effect on the marine atmospheric boundary layer and subsequent change in surface wind speeds (Frenger et al., 2013). There are two potential routes for carrying out this modelling work. We could modify code in MITgcm packages to account for the effects that sea surface temperature anomalies have on the 10 m wind speed. Another option would be to make use of the coupled WRF-MITgcm model developed by Scripps (Sun et al., 2019). This is a source for future work.

Deterministic style eddy parameterisations like GM and its variants are developed using physical laws to mimic the effects of mesoscale ocean eddies. Progress has been made using stochastic methods to improve the representation of eddies in climate models (Porta Mana and Zanna, 2014; Resseguier et al., 2020; Zanna and Bolton, 2021). The benefit of stochastic eddy parameterisations enables them to include the randomness associated with eddy-mean flow interactions (Hewitt et al., 2020). In the case of our derived eddy energy dissipation rate, the outcome is fixed based on the chosen inputs e.g. eddy amplitude and eddy length scale. Accounting for the randomness of mesoscale eddy damping by relative wind stress would require the need for a study on the effects of relative wind stress on eddy spectral space. Does relative wind stress only damp the first baroclinic mode, or are there induced non-linear interactions that make the damping effect appear random? Once this is diagnosed, then a stochastic eddy energy damping parameterisation could be developed in a future study.

6.6 Summary of the thesis

This thesis has examined relative wind stress damping through theoretical techniques and idealised modelling studies. The rate of decay by relative wind stress is approximated well by the analytical wind power input for barotropic and baroclinic eddies. The baroclinic prediction method works well over a short timescale until the mesoscale eddy in MITgcm is found to become unstable. The break down in the method has implications for the usability within current energy budget-based eddy parameterisations, and therefore warrants further work to include the additional dynamics. Nevertheless, the foundations for a simple relative wind stress damping parameterisation are proposed. In addition, on closer inspection of the MITgcm baroclinic eddy, relative wind stress modulates the already well known eddy response. Relative wind stress damping of kinetic energy is either counteracted, or slightly offset, by an additional conversion of potential to kinetic energy via Ekman pumping. A novel finding also revealed relative wind stress generated an earlier eddy destabilisation in a first baroclinic mode eddy. It is important that future work attempts to incorporate these responses into a subgrid eddy energy parameterisation. We propose that improvements to the prediction method must be made a priority. We also suggest pursuing the validity of the dissipation timescales for use in the current energy budget-based parameterisations. Additional research should also be carried out in improving the realism of the initial idealised mesoscale eddy experiment, such as through submesoscale resolution and surface heat fluxes.

Glossary

Key symbols

Symbol	Description	Units
KE	Kinetic energy	J
PE	Potential energy	J
E	Total eddy energy	J
KE_{M}	Mean kinetic energy	J
PE_{M}	Mean available potential energy	J
KE_{T}	Turbulent kinetic energy	J
PE_{T}	Turbulent available potential energy	J
$C(X, Y)$	Conversion of X to Y	W
Ro	Rossby number	
P	Wind power input	W
W	Wind work	W m^{-2}
D_{visc}	Viscous dissipation	W
A_4	Viscous diffusive coefficient	m^4 s^{-1}
$\boldsymbol{\tau}$	Wind stress	N m^{-2}
C_d	Drag coefficient	
g	Gravitational constant	m s^{-2}

Key symbols

g'	Reduced gravity	m s^{-2}
f	Coriolis frequency	s^{-1}
$\boldsymbol{u}$	Horizontal velocities	m s^{-1}
$\boldsymbol{u}_a$	Wind velocities in zonal and meridional direction	m s^{-1}
ρ_a	Air density at ocean surface	kg m^{-3}
ρ	Ocean density, where $\cdot_0$ is a reference	kg m^{-3}
b	Buoyancy	m s^{-2}
A	Eddy amplitude	m
R	Eddy e-folding radius	km
L_s	Eddy speed based radius	km
η or η_1	Eddy sea surface height	cm or m
η_2	Thermocline displacement	m
H	Reference ocean depth	m
μ, λ	Proportionality coefficients	
T_{bt}, T_{bc}	Barotropic and baroclinic decay timescales	days
N	Buoyancy frequency	s^{-1}
ζ	Relative vorticity	s^{-1}
W_{tot}	Total Ekman pumping	m day^{-1}
W_c	Wind stress curl induced Ekman pumping	m day^{-1}
W_ζ	Vorticity induced Ekman pumping	m day^{-1}
Q	Potential vorticity	s^{-3}
l	Azimuthal wavenumber	

Key symbols continued

Key abbreviations

Term	Description
$Pred$	Prediction method
MIT	Model output results
ACE	Anticyclonic eddy
CE	Cyclonic eddy
AW	Absolute wind
RW	Relative wind
BT	Barotropic mode
$BC1$	First baroclinic mode
SSH	Sea surface height
MKE	Mean kinetic energy
PV	Potential vorticity

Key abbreviations

Bibliography

Alemany, F., Quintanilla, L., Velez-Belchí, P., García, A., Cortés, D., Rodríguez, J., Fernández de Puelles, M., González-Pola, C., and López-Jurado, J. (2010). Characterization of the spawning habitat of Atlantic bluefin tuna and related species in the Balearic Sea (western Mediterranean). *Progress in Oceanography*, 86(1):21–38.

Arbic, B. K. and Flierl, G. R. (2004). Baroclinically Unstable Geostrophic Turbulence in the Limits of Strong and Weak Bottom Ekman Friction: Application to Midocean Eddies. *Journal of Physical Oceanography*, 34(10):2257 – 2273.

Arbic, B. K. and Scott, R. B. (2008). On Quadratic Bottom Drag, Geostrophic Turbulence, and Oceanic Mesoscale Eddies. *Journal of Physical Oceanography*, 38(1):84–103.

Arostegui, M. C., Gaube, P., Woodworth-Jefcoats, P. A., Kobayashi, D. R., and Braun, C. D. (2022). Anticyclonic eddies aggregate pelagic predators in a subtropical gyre. *Nature*, 609(7927):535–540.

Bachman, S. D. (2019). The GM+E closure: A framework for coupling backscatter with the Gent and McWilliams parameterization. *Ocean Modelling*, 136:85–106.

Baey, J.-M. and Carton, X. (2002). Vortex multipoles in two-layer rotating shallow-water flows. *Journal of Fluid Mechanics*, 460:151–175.

Bailleul, F., Cotté, C., and Guinet, C. (2010). Mesoscale eddies as foraging area of a deep-diving predator, the southern elephant seal. *Marine Ecology Progress Series*, 408:251–264.

Baker-Yeboah, S., Watts, D. R., and Byrne, D. A. (2009). Measurements of Sea Surface Height Variability in the Eastern South Atlantic from Pressure Sensor–Equipped Inverted Echo Sounders: Baroclinic and Barotropic Components. *Journal of Atmospheric and Oceanic Technology*, 26(12):2593–2609.

Barkan, R., Srinivasan, K., Yang, L., McWilliams, J. C., Gula, J., and Vic, C. (2021). Oceanic mesoscale eddy depletion catalyzed by internal waves. *Geosphysical Research Letters.*, 48(18):e2021GL094376.

Barkan, R., Winters, K. B., and McWilliams, J. C. (2017). Stimulated imbalance and the enhancement of eddy kinetic energy dissipation by internal waves. *Journal of Physical Oceanography*, 47(1).

Benilov, E. S., Broutman, D., and Kuznetsova, E. P. (1998). On the stability of large-amplitude vortices in a continuously stratified fluid on the f-plane. *Journal of Fluid Mechanics*, 355(1):139–162.

Boccaletti, G., Ferrari, R., and Fox-Kemper, B. (2007). Mixed Layer Instabilities and Restratification. *Journal of Physical Oceanography*, 37(9):2228 – 2250.

Brannigan, L., Marshall, D. P., Garabato, A. C. N., Nurser, A. J. G., and Kaiser, J. (2017). Submesoscale Instabilities in Mesoscale Eddies. *Journal of Physical Oceanography*, 47(12):3061–3085.

Bühler, O. and McIntyre, M. E. (2005). Wave capture and wave–vortex duality. *Journal of Fluid Mechanics*, 534:67–95.

Byrne, D., Münnich, M., Frenger, I., and Gruber, N. (2016). Mesoscale atmosphere ocean coupling enhances the transfer of wind energy into the ocean. *Nature Communications*, 7(11867).

Carton, X. J., Flierl, G. R., and Polvani, L. M. (1989). The generation of tripoles from unstable axisymmetric isolated vortex structures. *EPL (Europhysics Letters)*, 9:339.

Chaigneau, A., Gizolme, A., and Grados, C. (2008). Mesoscale eddies off Peru in altimeter records: Identification algorithms and eddy spatio-temporal patterns. *Progress Oceanography*, 79(2):106–119.

Charney, J. G. (1971). Geostrophic Turbulence. *Journal of Atmospheric Sciences.*, 28(6):1087 – 1095.

Chelton, D., Schlax, M., and Samelson, R. (2011). Global observations of nonlinear mesoscale eddies. *Progress in Oceanography*, 91:167–216.

Chelton, D. B., Schlax, M. G., Samelson, R. M., and de Szoeke, R. A. (2007). Global observations of large oceanic eddies. *Geosphysical Research Letters.*, 34(15).

Chen, G., Han, G., and Yang, X. (2019). On the intrinsic shape of oceanic eddies derived from satellite altimetry. *Remote Sensing of Environment*, 228:75–89.

Chen, K., Gaube, P., and Pallás-Sanz, E. (2020). On the Vertical Velocity and Nutrient Delivery in Warm Core Rings. *Journal of Physical Oceanography*, 50(6):1557–1582.

Chen, R., Flierl, G. R., and Wunsch, C. (2014). A Description of Local and Nonlocal Eddy-Mean Flow Interaction in a Global Eddy-Permitting State Estimate. *Journal of Physical Oceanography*, 44(9):2336–2352.

Chenillat, F., Franks, P., Rivière, P., Capet, X., and Grima, N. (2015). Plankton dynamics in a cyclonic eddy in the Southern California Current System. *Journal of Geophysical Research: Oceans*, 120:5566–5588.

Clément, L., Frajka-Williams, E., Sheen, K. L., Brearley, J. A., and Garabato, A. C. N. (2016). Generation of Internal Waves by Eddies Impinging on the Western Boundary of the North Atlantic. *Journal of Physical Oceanography*, 46(4):1067–1079.

Cushman-Roisin, B. and Beckers, J.-M. (2006). *Introduction to Geophysical Fluid Dynamics*, volume 101. Academic Press, 2nd edition.

Danabasoglu, G., McWilliams, J., and Gent, P. (1994). The Role of Mesoscale Tracer Transports in the Global Ocean Circulation. *Science (New York, N.Y.)*, 264:1123–6.

Dawe, J. T. and Thompson, L. (2006). Effect of ocean surface currents on wind stress, heat flux, and wind power input to the ocean. *Geophysical Research Letters*, 33(9).

de La Lama, M. S., LaCasce, J. H., and Fuhr, H. K. (2016). The vertical structure of ocean eddies. *Dynamics and Statistics of the Climate System*, 1(1).

Dewar, W. and Flierl, G. (1987). Some Effects of the Wind on Rings. *Journal of Physical Oceanography.*, 17(10):1653–1667.

Dewar, W. K. and Killworth, P. D. (1995). On the Stability of Oceanic Rings. *Journal of Physical Oceanography*, 25(6):1467–1487.

Dewar, W. K., Killworth, P. D., and Blundell, J. R. (1999). Primitive-Equation Instability of Wide Oceanic Rings. Part II: Numerical Studies of Ring Stability. *Journal of Physical Oceanography*, 29(8):1744–1758.

Donohue, K. A., Tracey, K. L., Watts, D. R., Chidichimo, M. P., and Chereskin, T. K. (2016). Mean Antarctic Circumpolar Current transport measured in Drake Passage. *Geophysical Research Letters*, 43(22):11,760–11,767.

Dove, L. A., Balwada, D., Thompson, A. F., and Gray, A. R. (2022). Enhanced ventilation in energetic regions of the Antarctic Circumpolar Current. *Geophysical Research Letters*, 49(13):e2021GL097574.

Dritschel, D. G. (1989). On the stabilization of a two-dimensional vortex strip by adverse shear. *Journal of Fluid Mechanics*, 206:193–221.

Duhaut, T. and Straub, D. (2006). Wind Stress Dependence on Ocean Surface

Velocity: Implications for Mechanical Energy Input to Ocean Circulation. *Journal of Physical Oceanography*, 36(2):202–211.

Dunphy, M. (2009). The Influence of Mesoscale Eddies on the Internal Tide. Master's thesis, University of Waterloo.

Dunphy, M. and Lamb, K. G. (2014). Focusing and vertical mode scattering of the first mode internal tide by mesoscale eddy interaction. *Journal of Geophysical Research: Oceans*, 119(1):523–536.

Durán-Campos, E., Monreal-Gómez, M. A., Salas de León, D. A., and Coria-Monter, E. (2019). Impact of a dipole on the phytoplankton community in a semi-enclosed basin of the southern Gulf of California, Mexico. *Oceanologia*, 61(3):331–340.

Ebuchi, N., Graber, H. C., and Caruso, M. J. (2002). Evaluation of Wind Vectors Observed by QuikSCAT/SeaWinds Using Ocean Buoy Data. *Journal of Atmospheric and Oceanic Technology*, 19(12):2049–2062.

Eden, C. and Greatbatch, R. J. (2008). Towards a mesoscale eddy closure. *Ocean Modelling.*, 20(3):223–239.

Falkowski, P. G., Ziemann, D., Kolber, Z., and Bienfang, P. K. (1991). Role of eddy pumping in enhancing primary production in the ocean. *Nature*, 352(6330):55–58.

Ferrari, R. and Wunsch, C. (2009). Ocean circulation kinetic energy: Reservoirs, sources, and sinks. *Annual Review of Fluid Mechanics*, 41:253–82.

Frenger, I., Gruber, N., Knutti, R., and Münnich, M. (2013). Imprint of Southern Ocean eddies on winds, clouds and rainfall. *Nature Geoscience Letters*, 6:608–612.

Gaube, P., Chelton, D., Samelson, R., Schlax, M., and O'Neill, L. (2015). Satellite observations of mesoscale eddy-induced ekman pumping. *Journal of Physical Oceanography*, 45:104–132.

Gaube, P., Chelton, D. B., Strutton, P. G., and Behrenfeld, M. J. (2013). Satellite observations of chlorophyll, phytoplankton biomass, and Ekman pumping in nonlinear mesoscale eddies. *Journal of Geosphysical Research Oceans*, 118(12):6349–6370.

Gaube, P., McGillicuddy, D., Chelton, D., Behrenfeld, M., and Strutton, P. (2014). Regional variations in the influence of mesoscale eddies on near-surface chlorophyll. *Journal of Geosphysical Research Oceans*, 119:8195–8220.

Gent, P. and McWilliams, J. (1986). The instability of barotropic circular vortices. *Geophysical & Astrophysical Fluid Dynamics*, 35:209–233.

Gent, P. and McWilliams, J. (1990). Isopycnal mixing in Ocean Circulation Models. *Journal of Physical Oceanography*, 20:150–155.

Gent, P. R., Willebrand, J., McDougall, T. J., and McWilliams, J. C. (1995). Parameterizing Eddy-Induced Tracer Transports in Ocean Circulation Models. *Journal of Physical Oceanography*, 25(4):463–474.

Gill, A. (1982). *Atmosphere-Ocean Dynamics*, volume 30. Academic Press.

Gill, A., Green, J., and Simmons, A. (1974). Energy partition in the large-scale ocean circulation and the production of mid-ocean eddies. *Deep-Sea Research*, 21:499–528.

Gordon, C., Cooper, C., Senior, C., Hewitt, H., Gregory, J., Johns, T., Mitchell, J., and Wood, R. (2000). The Simulation of SST, Sea Ice Extents and Ocean Heat Transports in a Version of the Hadley Centre Coupled Model Without Flux Adjustments. *Climate Dynamics*, 16:147–168.

Greatbatch, R. J., Zhai, X., Claus, M., Czeschel, L., and Rath, W. (2010). Transport driven by eddy momentum fluxes in the Gulf Stream Extension region. *Geophysical Research Letters*, 37(24).

Griffies, S. M. and Hallberg, R. W. (2000). Biharmonic Friction with a Smagorinsky-Like Viscosity for Use in Large-Scale Eddy-Permitting Ocean Models. *Monthly Weather Review*, 128(8):2935 – 2946.

Griffies, S. M., Winton, M., Anderson, W. G., Benson, R., Delworth, T. L., Dufour, C. O., Dunne, J. P., Goddard, P., Morrison, A. K., Rosati, A., Wittenberg, A. T., Yin, J., and Zhang, R. (2015). Impacts on Ocean Heat from Transient Mesoscale Eddies in a Hierarchy of Climate Models. *Journal of Climate*, 28(3):952 – 977.

Hallberg, R. and Gnanadesikan, A. (2001). An Exploration of the Role of Transient Eddies in Determining the Transport of a Zonally Reentrant Current. *Journal of Physical Oceanography*, 31(11):3312–3330.

Hallberg, R. and Gnanadesikan, A. (2006). The Role of Eddies in Determining the Structure and Response of the Wind-Driven Southern Hemisphere Overturning: Results from the Modeling Eddies in the Southern Ocean (MESO) Project. *Journal of Physical Oceanography*, 36:2232–2252.

Helfrich, K. R. and Send, U. (1988). Finite-amplitude evolution of two-layer geostrophic vortices. *Journal of Fluid Mechanics*, 197:331–348.

Hewitt, H., Fox-Kemper, B., Pearson, B., Roberts, M., and Klocke, D. (2022). The Small Scales of the Ocean May Hold the Key to Surprises. *Nature Climate Change*, 12(6):496–499.

Hewitt, H., Roberts, M., Hyder, P., Graham, T., Rae, J., Belcher, S. E., Bourdalle-Badie, R., Copsey, D., Coward, A., Guiavarc'h, C., Harris, C., Hill, R., Hirschi, J., Madec, G., Mizielinski, M., Neininger, E., New, A., Rioual, J.-C., Sinha, B., and Wood, R. (2016). The impact of resolving the Rossby radius at mid-latitudes in the ocean: Results from a high-resolution version of the Met Office GC2 coupled model. *Geoscientific Model Development*, 9:3655–3670.

Hewitt, H. T., Roberts, M., Mathiot, P., Biastoch, A., Blockley, E., Chassignet, E. P., Fox-Kemper, B., Hyder, P., Marshall, D. P., Popova, E., Treguier, A.-M., Zanna, L., Yool, A., Yu, Y., Beadling, R., Bell, M., Kuhlbrodt, T., Arsouze, T., Bellucci, A., Castruccio, F., Gan, B., Putrasahan, D., Roberts, C. D., Van Roekel, L., and Zhang, Q. (2020). Resolving and Parameterising the

Ocean Mesoscale in Earth System Models. *Current Climate Change Reports*, 6(4):137–152.

Hill, C., Ferreira, D., Campin, J.-M., Marshall, J., Abernathey, R., and Barrier, N. (2012). Controlling spurious diapycnal mixing in eddy-resolving height-coordinate ocean models – Insights from virtual deliberate tracer release experiments. *Ocean Modelling.*, 45-46:14–26.

Hirst, A. C. and McDougall, T. J. (1996). Deep-Water Properties and Surface Buoyancy Flux as Simulated by a Z-Coordinate Model Including Eddy-Induced Advection. *Journal of Physical Oceanography*, 26(7):1320 – 1343.

Holland, W. (1978). The Role of Mesoscale Eddies in the General Circulation of the Ocean - Numerical Experiments Using a Wind-Driven Quasi-Geostrophic Model. *Journal of Physical Oceanography*, 8:363–392.

Holland, W. and Lin, L. (1975). On the Generation of Mesoscale Eddies and their Contribution to the Oceanic General Circulation. I. A Preliminary Numerical Experiment. *Journal of Physical Oceanography*, 5:642–657.

Hoskins, B. J., McIntyre, M. E., and Robertson, A. W. (1985). On the use and significance of isentropic potential vorticity maps. *Quarterly Journal of the Royal Meteorological Society*, 111(470):877–946.

Huang, C. and Xu, Y. (2018). Update on the global energy dissipation rate of deep-ocean low-frequency flows by bottom boundary layer. *Journal of Physical Oceanography*, 48(6):1243 – 1255.

Hughes, C. and Wilson, C. (2008). Wind work on the geostrophic ocean circulation: An observational study of the effect of small scales in the wind stress. *Journal of Geophysical Research*, 113(C02016).

Ikeda, M. (1981). Instability and Splitting of Mesoscale Rings using a Two-Layer Quasi-Geostrophic Model on an f-Plane. *Journal of Physical Oceanography*, 11(7):987–998.

Ilıcak, M., Adcroft, A. J., Griffies, S. M., and Hallberg, R. W. (2012). Spurious Dianeutral Mixing and the Role of Momentum Closure. *Ocean Modelling*, 45–46:37–58.

Jablonowski, C. and Williamson, D. L. (2011). The Pros and Cons of Diffusion, Filters and Fixers in Atmospheric General Circulation Models. In Lauritzen, P., Jablonowski, C., Taylor, M., and Nair, R., editors, *Numerical Techniques for Global Atmospheric Models*, volume 80 of *Lecture Notes in Computational Science and Engineering*. Springer.

Jansen, M. F., Adcroft, A., Khani, S., and Kong, H. (2019). Toward an Energetically Consistent, Resolution Aware Parameterization of Ocean Mesoscale Eddies. *Journal of Advances in Modeling Earth Systems*, 11(8):2844–2860.

Jullien, S., Masson, S., Oerder, V., Samson, G., Colas, F., and Renault, L. (2020). Impact of ocean-atmosphere current feedback on ocean mesoscale activity: Regional variations and sensitivity to model resolution. *Journal of Climate*, 33(7):2585 – 2602.

Kaneko, H., Itoh, S., Kouketsu, S., Okunishi, T., Hosoda, S., and Suga, T. (2015). Evolution and modulation of a poleward-propagating anticyclonic eddy along the Japan and Kuril-Kamchatka trenches. *Journal of Geophysical Research: Oceans*, 120(6):4418–4440.

Katsman, C., Vaart, P., Dijkstra, H., and Ruijter, W. (2003). Stability of Multilayer Ocean Vortices: A Parameter Study Including Realistic Gulf Stream and Agulhas Rings. *Journal of Physical Oceanography*, 33:1197–1218.

Kjellsson, J. and Zanna, L. (2017). The Impact of Horizontal Resolution on Energy Transfers in Global Ocean Models. *Fluids*, 2(3).

Kloosterziel, R. and Van Heijst, G. (1991). An experimental study of unstable barotropic vortices in a rotating fluid. *Journal of Fluid Mechanics*, 223:1–24.

Large, G. and Yeager, S. (2004). Diurnal to Decadal Global Forcing for Ocean and Sea-Ice Models: The Data Sets and Flux Climatologies. NCAR/TN-460+STR.

Large, W. G., McWilliams, J. C., and Doney, S. C. (1994). Oceanic vertical mixing: A review and a model with a nonlocal boundary layer parameterization. *Reviews of Geophysics*, 32(4):363–403.

Lee, D.-K. and Niiler, P. P. (1998). The inertial chimney: The near-inertial energy drainage from the ocean surface to the deep layer. *Journal of Geophysical Research: Oceans*, 103(C4):7579–7591.

Levy, M., Klein, P., and Treguier, A.-M. (2001). Impact of sub-mesoscale physics on production and subduction of phytoplankton in an oligotrophic regime. *Journal of Marine Research*, 59:535–565.

Lorenz, E. (1955). Available potential energy and the maintenance of the general circulation. *Tellus*, 7:157–167.

Ma, X., Chang, P. Saravanan, R. M. R., Hsieh, J., Wu, D., Lin, X., Wu, L., and Jing, Z. (2015). Distant Influence of Kuroshio Eddies on North Pacific Weather Patterns? *Scientific Reports*, 5(17785).

Ma, X., Jing, Z., Chang, P., Liu, X., Montuoro, R., Small, R., O. Bryan, F., Greatbatch, R., Brandt, P., Wu, D., Lin, X., and Wu, L. (2016). Western boundary currents regulated by interaction between ocean eddies and the atmosphere. *Nature*, 535:533–537.

Mahdinia, M., Hassanzadeh, P., Marcus, P., and Jiang, C.-H. (2017). Stability of three-dimensional gaussian vortices in an unbounded, rotating, vertically stratified, boussinesq flow: Linear analysis. *Journal of Fluid Mechanics*, 824:97–134.

Mak, J., Maddison, J. R., Marshall, D. P., and Munday, D. R. (2018). Implementation of a Geometrically Informed and Energetically Constrained Mesoscale Eddy Parameterization in an Ocean Circulation Model. *Journal of Physical Oceanography*, 48(10):2363 – 2382.

Mak, J., Marshall, D., Maddison, J., and Bachman, S. (2017). Emergent eddy saturation from an energy constrained eddy parameterisation. *Ocean Modelling*, 112:125–138.

Mak, J., Marshall, D. P., Madec, G., and Maddison, J. R. (2022). Acute Sensitivity of Global Ocean Circulation and Heat Content to Eddy Energy Dissipation Timescale. *Geophysical Research Letters*, 49(8):e2021GL097259.

Marshall, D. P., Maddison, J. R., and Berloff, P. S. (2012). A Framework for Parameterizing Eddy Potential Vorticity Fluxes. *Journal of Physical Oceanography*, 42(4):539 – 557.

Marshall, J., Adcroft, A., Hill, C., Perelman, L., and Heisey, C. (1997a). A finite-volume, incompressible Navier Stokes model for studies of the ocean on parallel computers. *Journal of Geophysical Research*, 102(C3):5753–5766.

Marshall, J., Hill, C., Perelman, L., and Adcroft, A. (1997b). Hydrostatic, quasi-hydrostatic, and nonhydrostatic ocean modeling. *Journal of Geophysical Research*, 102(C3):5733–5752.

McClean, J. L., Bader, D. C., Bryan, F. O., Maltrud, M. E., Dennis, J. M., Mirin, A. A., Jones, P. W., Kim, Y. Y., Ivanova, D. P., Vertenstein, M., Boyle, J. S., Jacob, R. L., Norton, N., Craig, A., and Worley, P. H. (2011). A prototype two-decade fully-coupled fine-resolution CCSM simulation. *Ocean Modelling.*, 39(1):10–30.

McGillicuddy, D. (2015). Formation of Intrathermocline Lenses by Eddy-Wind Interaction. *Journal of Physical Oceanography*, 45(C6):606–612.

McGillicuddy, D., Robinson, A., Siegel, D., Jannasch, H., Johnson, R., Dickey, T., McNeil, J. andMichaels, A., and Knap, A. (1998). Influence of mesoscale eddies on new production in the Sargasso Sea. *Nature*, 394:263–266.

McGillicuddy, D. J. (2016). Mechanisms of Physical-Biological-Biogeochemical Interaction at the Oceanic Mesoscale. *Annual Review of Marine Science*, 8(1):125–159.

McGillicuddy, D.J. Anderson, L., Bates, N., Bibby, T., Buesseler, K., Carlson, C., Davis, C., Ewart, C., Falkowski, P., Goldthwait, S., Hansell, D., Jenkins, W., Johnson, R., Kosnyrev, V., Ledwell, J., Li, Q., Siegel, D., and Steinberg, D. (2007). Eddy/Wind Interactions Stimulate Extraordinary Mid-Ocean Plankton Blooms. *Science*, 316(C6):1021–1025.

McWilliams, J. (2021). Oceanic frontogenesis. *Annual Review of Marine Science*, 13(1):227–253.

Mcwilliams, J. C. (2008). The Nature and Consequences of Oceanic Eddies. In *Ocean Modeling in an Eddying Regime*, pages 5–15. American Geophysical Union (AGU).

Meijers, A. J., Bindoff, N. L., and Roberts, J. L. (2007). On the Total, Mean, and Eddy Heat and Freshwater Transports in the Southern Hemisphere of a $\frac{1}{8}^{\circ} \times \frac{1}{8}^{\circ}$ Global Ocean Model. *Journal of Physical Oceanography*, 37(2):277 – 295.

Meredith, M. P., Garabato, A. C. N., Hogg, A. M., and Farneti, R. (2012). Sensitivity of the Overturning Circulation in the Southern Ocean to Decadal Changes in Wind Forcing. *Journal of Climate*, 25(1):99 – 110.

Mkhinini, N., Coimbra, A., Stegner, A., Arsouze, T., Taupier-Letage, I., and Béranger, K. (2014). Long-lived mesoscale eddies in the eastern Mediterranean Sea: Analysis of 20 years of AVISO geostrophic velocities. *Journal of Geophysical Research: Oceans*, 119.

Molemaker, M. and Dijkstra, H. (2000). Stability of a Cold Core Eddy in the Presence of Convection: Hydrostatic versus Nonhydrostatic Modeling. *Journal of Physical Oceanography*, 30(3):475–494.

Moorthi, S. and Suarez, M. J. (1992). Relaxed Arakawa-Schubert. A Parameterization of Moist Convection for General Circulation Models. *Monthly Weather Review*, 120(6):978 – 1002.

Morrow, R., Birol, F., Griffin, D., and Sudre, J. (2004). Divergent pathways of cyclonic and anti-cyclonic ocean eddies. *Geophysical Research Letters*, 31(24).

Munday, D. and Zhai, X. (2015). Sensitivity of Southern Ocean circulation to wind stress changes: Role of relative wind stress. *Ocean Modelling*, 95:15–24.

Munday, D. R., Johnson, H. L., and Marshall, D. P. (2013). Eddy Saturation of Equilibrated Circumpolar Currents. *Journal of Physical Oceanography*, 43(3):507 – 532.

Munday, D. R., Johnson, H. L., and Marshall, D. P. (2014). Impacts and effects of mesoscale ocean eddies on ocean carbon storage and atmospheric pCO2. *Global Biogeochemical Cycles*, 28(8):877–896.

Munday, D. R., Zhai, X., Harle, J., Coward, A. C., and Nurser, A. G. (2021). Relative vs. absolute wind stress in a circumpolar model of the southern ocean. *Ocean Modelling*, 168:101891.

Nan, F., He, Z., Zhou, H., and Wang, D. (2011). Three long-lived anticyclonic eddies in the northern South China Sea. *Journal of Geophysical Research: Oceans*, 116(C5).

Nardelli, B. B. (2013). Vortex waves and vertical motion in a mesoscale cyclonic eddy. *Journal of Geophysical Research: Oceans*, 118(10):5609–5624.

Oerder, V., Colas, F., Masson, S., and Lemarié, F. (2018). Impacts of the Mesoscale Ocean-Atmosphere Coupling on the Peru-Chile Ocean Dynamics: The Current-Induced Wind Stress Modulation. *Journal of Geophysical Research: Oceans*, 123:812–833.

Pacanowski, R. (1987). Effect of Equatorial Currents on Surface Stress. *Journal of Physical Oceanography*, 17(6):833–838.

Pezzi, L. P., de Souza, R. B., Santini, M. F., Miller, A. J., Carvalho, J. T., Parise, C. K., Quadro, M. F., Rosa, E. B., Justino, F., Sutil, U. A., Cabrera, M. J., Babanin, A. V., Voermans, J., Nascimento, E. L., Alves, R. C. M., Munchow,

G. B., and Rubert, J. (2021). Oceanic eddy-induced modifications to air-sea heat and CO_2 fluxes in the Brazil-Malvinas Confluence. *Scientific Reports*, 11(1):10648.

Pierrehumbert, R. T. and Swanson, K. L. (1995). Baroclinic Instability. *Annual Review of Fluid Mechanics.*, 27(1):419–467.

Pilo, G. S., Oke, P. R., Coleman, R., Rykova, T., and Ridgway, K. (2018). Patterns of Vertical Velocity Induced by Eddy Distortion in an Ocean Model. *Journal of Geosphysical Research Oceans*, 123(3):2274–2292.

Polzin, K. L. (2010). Mesoscale eddy–internal wave coupling. part ii: Energetics and results from polymode. *Journal of Physical Oceanography*, 40(4):789 – 801.

Porta Mana, P. and Zanna, L. (2014). Toward a Stochastic Parameterization of Ocean Mesoscale Eddies. *Ocean Modelling*, 79:1–20.

Prather, M. J. (1986). Numerical advection by conservation of second-order moments. *Journal of Geosphysical Research*, 91(D6):6671–6681.

Redi, M. H. (1982). Oceanic Isopycnal Mixing by Coordinate Rotation. *Journal of Physical Oceanography*, 12(10):1154 – 1158.

Renault, L., Jeroen Molemaker, M., Gula, J., Masson, S., and McWilliams, J. (2016a). Control and Stabilization of the Gulf Stream by Oceanic Current Interaction with the Atmosphere. *Journal of Physical Oceanography*, 46(15):3439–3453.

Renault, L., Jeroen Molemaker, M., McWilliams, J., Shchepetkin, A., Lemairé, F., Chelton, D., Illig, S., and Hall, A. (2016b). Modulation of Wind Work by Oceanic Current Interaction with the Atmosphere. *Journal of Physical Oceanography*, 46(15):1686–1704.

Renault, L., Marchesiello, P., Masson, S., and McWilliams, J. C. (2019). Remarkable Control of Western Boundary Currents by Eddy Killing, a Mechanical Air-Sea Coupling Process. *Geosphysical Research Letters.*, 46(5):2743–2751.

Renault, L., McWilliams, J., and Gula, J. (2018). Dampening of Submesoscale Currents by Air-Sea Stress Coupling in the Californian Upwelling System. *Scientific Reports*, 8(13388).

Resseguier, V., Pan, W., and Fox-Kemper, B. (2020). Data-driven versus self-similar parameterizations for stochastic advection by Lie transport and location uncertainty. *Nonlinear Processes in Geophysics*, 27(2):209–234.

Rimac, A., von Storch, J.-S., Eden, C., and Haak, H. (2013). The influence of high-resolution wind stress field on the power input to near-inertial motions in the ocean. *Geophysical Research Letters*, 40(18):4882–4886.

Rintoul, S. (2018). The global influence of localized dynamics in the Southern Ocean. *Nature*, 558.

Schouten, M. W., de Ruijter, W. P. M., van Leeuwen, P. J., and Lutjeharms, J. R. E. (2000). Translation, decay and splitting of Agulhas rings in the southeastern Atlantic Ocean. *Journal of Geophysical Research: Oceans*, 105(C9):21913–21925.

Schubert, R., Gula, J., Greatbatch, R. J., Baschek, B., and Biastoch, A. (2020). The Submesoscale Kinetic Energy Cascade: Mesoscale Absorption of Submesoscale Mixed Layer Eddies and Frontal Downscale Fluxes. *Journal of Physical Oceanography*, 50(9):2573–2589.

Scott, R. B. and Arbic, B. K. (2007). Spectral energy fluxes in geostrophic turbulence: Implications for ocean energetics. *Journal of Physical Oceanography*, 37(3):673 – 688.

Scott, R. B. and Wang, F. (2005). Direct Evidence of an Oceanic Inverse Kinetic Energy Cascade from Satellite Altimetry. *Journal of Physical Oceanography*, 35(9):1650 – 1666.

Sen, A., Scott, R., and Arbic, B. (2008). Global energy dissipation rate of deep-ocean low frequency flows by quadratic bottom boundary layer drag: computations from current-meter data. *Journal of Geophysical Research*, 35.

Seo, H., Miller, A. J., and Norris, J. R. (2016). Eddy–Wind Interaction in the California Current System: Dynamics and Impacts. *Journal of Physical Oceanography*, 46(2):439 – 459.

Shan, X., Jing, Z., Sun, B., and Wu, L. (2020). Impacts of ocean current–atmosphere interactions on mesoscale eddy energetics in the Kuroshio extension region. *Geoscience Letters*, 7(3).

Small, R. J., deSzoeke, S. P., Xie, S. P., O'Neill, L., Seo, H., Song, Q., Cornillon, P., Spall, M., and Minobe, S. (2008). Air–Sea Interaction over Ocean Fronts and Eddies. *Dynamics of Atmospheres and Oceans*, 45(3):274–319.

Smith, K. S. and Vallis, G. K. (2001). The scales and equilibration of midocean eddies: Freely evolving flow. *Journal of Physical Oceanography*, 31(2):554 – 571.

Song, H., Marshall, J., McGillicuddy Jr., D. J., and Seo, H. (2020). Impact of Current-Wind Interaction on Vertical Processes in the Southern Ocean. *Journal of Geosphysical Research Oceans*, 125(4).

Song, H., Marshall, J., Munro, D., Dutkiewicz, S., Sweeney, C., McGillicuddy, D., and Hausmann, U. (2016). Mesoscale modulation of air-sea CO_2 flux in Drake Passage. *Journal of Geosphysical Research Oceans*, 121:6635–6649.

Stammer, D. (1997). Global Characteristics of Ocean Variability Estimated from Regional TOPEX/POSEIDON Altimeter Measurements. *Journal of Physical Oceanography*, 27(8):1743 – 1769.

Stegner, A. and Dritschel, D. (2000). A Numerical Investigation of the Stability of Isolated Shallow Water Vortices. *Journal of Physical Oceanography*, 30:2562–2573.

Stern, M. E. (1965). Interaction of a uniform wind stress with a geostrophic vortex. *Deep-Sea Research*, 12(3):355–367.

Stewart, A. L. and Thompson, A. F. (2015). Eddy-mediated transport of warm Circumpolar Deep Water across the Antarctic Shelf Break. *Geophysical Research Letters*, 42(2):432–440.

Stewart, K., Hogg, A., Griffies, S., Heerdegen, A., Ward, M., Spence, P., and England, M. (2017). Vertical resolution of baroclinic modes in global ocean models. *Ocean Modelling*, 113:50–65.

Straub, D. N. (1993). On the Transport and Angular Momentum Balance of Channel Models of the Antarctic Circumpolar Current. *Journal of Physical Oceanography*, 23(4):776–782.

Su, Z., Wang, J., Klein, P., Thompson, A., and Menemenlis, D. (2018). Ocean submesoscales as a key component of the global heat budget. *Nature Communications*, 9(775).

Sun, R., Subramanian, A. C., Miller, A. J., Mazloff, M. R., Hoteit, I., and Cornuelle, B. D. (2019). SKRIPS v1.0: A Regional Coupled Ocean–Atmosphere Modeling Framework (MITgcm–WRF) Using ESMF/NUOPC, Description and Preliminary Results for the Red Sea. *Geoscientific Model Development*, 12(10):4221–4244.

Sutyrin, G. G. (2016). On sharp vorticity gradients in elongating baroclinic eddies and their stabilization with a solid-body rotation. *Geosphysical Research Letters*, 43(11):5802–5811.

Tedesco, P., Gula, J., Penven, P., and Ménesguen, C. (2022). Mesoscale Eddy Kinetic Energy Budgets and Transfers between Vertical Modes in the Agulhas Current. *Journal of Physical Oceanography*, 52.

Thompson, A., Heywood, K., Schmidtko, S., and Stewart, A. (2014). Eddy transport as a key component of the Antarctic overturning circulation. *Nature Geosciences*, 7:879–884.

Torres, H. S., Klein, P., Wang, J., Wineteer, A., Qiu, B., Thompson, A. F., Renault, L., Rodriguez, E., Menemenlis, D., Molod, A., Hill, C. N., Strobach, E., Zhang, H., Flexas, M., and Perkovic-Martin, D. (2022). Wind work at the air-sea interface: A modeling study in anticipation of future space missions. *Geoscientific Model Development*, 15(21):8041–8058.

Trossman, D. S., Arbic, B. K., Straub, D. N., Richman, J. G., Chassignet, E. P., Wallcraft, A. J., and Xu, X. (2017). The Role of Rough Topography in Mediating Impacts of Bottom Drag in Eddying Ocean Circulation Models. *Journal of Physical Oceanography*, 47(8):1941 – 1959.

Vallis, G. K. (2006). *Atmospheric and Oceanic Fluid Dynamics.* Cambridge University Press, Cambridge, U.K.

Villas-Bôas, A., Sato, O., Chaigneau, A., and Castelão, G. (2015). The signature of mesoscale eddies on the air-sea turbulent heat fluxes in the south atlantic ocean. *Geosphysical Research Letters*, 42:1856–1862.

von Storch, J.-S., Eden, C., Fast, I., Haak, H., Hernandez-Deckers, D., Maier-Reimer, E., Marotzke, J., and Stammer, D. (2012). An estimate of the Lorenz energy cycle for the world ocean based on the 1/10° STORM/NCEP simulation. *Journal of Physical Oceanography*, 42:2185–2205.

Wang, W. and Huang, R. X. (2004). Wind Energy Input to the Ekman Layer. *Journal of Physical Oceanography*, 34(5):1267–1275.

Wilder, T., Zhai, X., Munday, D., and Joshi, M. (2022). The Response of a Baroclinic Anticyclonic Eddy to Relative Wind Stress Forcing. *Journal of Physical Oceanography*, 52(9):2129–2142.

Wu, Y., Zhai, X., and Wang, Z. (2017). Decadal-Mean Impact of Including Ocean Surface Currents in Bulk Formulas on Surface Air–Sea Fluxes and Ocean General Circulation. *Journal of Climate*, 30(23):9511 – 9525.

Wunsch, C. (1997). The vertical partition of oceanic horizontal kinetic energy. *Journal of Physical Oceanography*, 27:1770–1794.

Wunsch, C. (1998). The Work Done by the Wind on the Oceanic General Circulation. *Journal of Physical Oceanography*, 28(11):2332–2340.

Wunsch, C. and Stammer, D. (1998). Satellite Altimetry, the Marine Geoid, and the Oceanic General Circulation. *Annual Review of Earth and Planetary Sciences*, 26(1):219–253.

Xu, C., Zhai, X., and Shang, X.-D. (2016). Work done by atmospheric winds on mesoscale ocean eddies. *Journal of Geosphysical Research Lett*, 43(12):174–180.

Yang, G., Wang, F., Li, Y., and Lin, P. (2013). Mesoscale eddies in the northwestern subtropical pacific ocean: Statistical characteristics and three-dimensional structures. *Journal of Geosphysical Research: Oceans*, 118:1906–1925.

Yang, L., Nikurashin, M., Hogg, A. M., and Sloyan, B. M. (2018). Energy loss from transient eddies due to lee wave generation in the southern ocean. *Journal of Physical Oceanography*, 48(12):2867 – 2885.

Yang, Z., Zhai, X., Marshall, D. P., and Wang, G. (2021). An idealized model study of eddy energetics in the western boundary “graveyard”. *Journal of Physical Oceanography*, 51(4):1265 – 1282.

Youngs, M. K., Thompson, A. F., Lazar, A., and Richards, K. J. (2017). ACC Meanders, Energy Transfer, and Mixed Barotropic-Baroclinic Instability. *Journal of Physical Oceanography*, 47(6):1291–1305.

Zanna, L. and Bolton, T. (2021). Deep Learning of Unresolved Turbulent Ocean Processes in Climate Models. In *Deep Learning for the Earth Sciences*, chapter 20, pages 298–306. John Wiley & Sons, Ltd.

Zhai, X. and Greatbatch, R. (2006). Surface eddy diffusivity for heat in a model of the northwest Atlantic Ocean. *Geosphysical Research Letters*, 33(L24611).

Zhai, X. and Greatbatch, R. (2007). Wind work in a model of the northwest Atlantic Ocean. *Geosphysical Research Letters*, 34(4).

Zhai, X., Greatbatch, R., and Sheng, J. (2004). Diagnosing the role of eddies in driving the circulation of the northwest atlantic ocean. *Geosphysical Research Letters*, 31(L23304).

Zhai, X., Johnson, H., and Marshall, D. (2010). Significant sink of ocean-eddy energy near western boundaries. *Nature Geoscience Letters*, 3:608–612.

Zhai, X., Johnson, H., Marshall, D., and Wunsch, C. (2012). On the Wind Power Input to the Ocean General Circulation. *Journal of Physical Oceanography*, 42:1357–1365.

Zhai, X. and Yang, Z. (2022). Eddy-induced meridional transport variability at ocean western boundary. *Ocean Modelling*, 171:101960.

Zhang, Z., Wang, W., and Qiu, B. (2014). Oceanic mass transport by mesoscale eddies. *Science*, 345(6194):322–324.